



HAL
open science

Solar driven catalytic reduction of CO₂ in water at photovoltaic materials with Co molecular catalysts

Ruwen Wang

► **To cite this version:**

Ruwen Wang. Solar driven catalytic reduction of CO₂ in water at photovoltaic materials with Co molecular catalysts. Catalysis. Université Paris Cité, 2022. English. NNT : 2022UNIP7145 . tel-04307156

HAL Id: tel-04307156

<https://theses.hal.science/tel-04307156>

Submitted on 25 Nov 2023

HAL is a multi-disciplinary open access archive for the deposit and dissemination of scientific research documents, whether they are published or not. The documents may come from teaching and research institutions in France or abroad, or from public or private research centers.

L'archive ouverte pluridisciplinaire **HAL**, est destinée au dépôt et à la diffusion de documents scientifiques de niveau recherche, publiés ou non, émanant des établissements d'enseignement et de recherche français ou étrangers, des laboratoires publics ou privés.

UNIVERSITÉ DE PARIS CITÉ

LABORATOIRE D'ÉLECTROCHIMIE MOLÉCULAIRE

École Doctorale 388

Chimie Physique et de Chimie Analytique de Paris Centre

THÈSE DE DOCTORAT

PRÉSENTÉE PAR **RUWEN WANG**

**Solar driven catalytic reduction of CO₂ in water at
photovoltaic materials with Co molecular catalysts**

Thèse soutenue publiquement le 16 Juin 2022 devant le jury composé de :

Rapporteur : **Dr. Gabriel LOGET, Université de Rennes**

Rapporteuse : **Dr. Marie-Noëlle COLLOMB, Université Grenoble-Alpes**

Examineur : **Dr. Winfried LIEBL, CEA Saclay**

Présidente, Examinatrice : **Dr. Muriel CHAVAROT-KERLIDOU, Université Grenoble-Alpes**

Directeurs de thèse : **Dr. Julien BONIN, Université Paris Cité**

Prof. Marc ROBERT, Université Paris Cité

Résumé en français

Le climat de la Terre a changé au cours de l'histoire. Les preuves scientifiques du réchauffement du système climatique sont sans équivoque. La tendance actuelle au réchauffement de la planète est le résultat de l'activité humaine depuis le milieu du 20^e siècle et se poursuit à un rythme sans précédent. Une étude récente souligne que l'augmentation des niveaux de CO₂ entraînera une hausse de la température globale et aura un impact sévère sur la survie de tous les êtres vivants. Par conséquent, afin d'éviter les pires effets du changement climatique, le monde doit de toute urgence réduire les émissions de CO₂. Cependant, la manière dont cette responsabilité est partagée entre les régions, les pays et les individus a toujours été un point de discorde sans fin dans les discussions internationales. La dépendance excessive à l'égard des combustibles fossiles n'a pas seulement accéléré la surexploitation des ressources naturelles, elle a également interrompu le cycle du carbone. C'est avec reconnaissance que la plupart des pays se sont tournés vers des sources d'énergie à faible teneur en carbone - technologies nucléaires et renouvelables. Les énergies renouvelables et durables joueront un rôle clé dans la décarbonisation de nos systèmes énergétiques au cours des prochaines décennies. Le captage et l'utilisation du CO₂ (CCU) ont suscité beaucoup d'intérêt.

La réduction du CO₂ présente des avantages considérables, mais reste un défi difficile à relever. Des progrès ont été réalisés ces dernières années. Parmi eux, l'utilisation de l'énergie solaire en abondance pour convertir le CO₂ en produits chimiques à plus haute valeur ajoutée grâce à la technologie de la photoélectrocatalyse

a attiré l'attention de nombreux chercheurs en chimie, en matériaux et en sciences environnementales.

L'énergie solaire est la source d'énergie renouvelable et propre la plus abondante. Elle peut être utilisée à grande échelle en convertissant efficacement l'énergie solaire en énergie électrique par la production de paires électron-trou séparées. Cependant, le stockage de l'électricité à grande échelle reste un défi, tandis que son transport est associé à d'importantes pertes. Par le biais de la photosynthèse naturelle, une autre stratégie a vu le jour : la conversion de l'énergie solaire en combustibles chimiques (stockage de l'énergie dans des liaisons chimiques). Cela peut se faire en utilisant l'électricité produite à partir de l'énergie solaire pour mettre en œuvre des réactions électrocatalytiques de manière indirecte ou en générant des produits chimiques par des réactions photoélectrocatalytiques de manière directe.

La réduction photoélectrochimique (PEC) du CO_2 est alimentée par l'électricité et l'irradiation lumineuse. La PEC présente plusieurs avantages, comme la sélectivité contrôlable des produits et l'utilisation écologique de l'énergie solaire renouvelable. Elle peut atteindre une efficacité et une sélectivité élevées grâce à l'intégration et à l'optimisation des avantages de l'électrocatalyse et de la photocatalyse.

L'élément clé du processus de réduction du CO_2 par la CEP est la photoélectrode. Une photoélectrode se compose d'un photoabsorbeur et d'un catalyseur pour réduire le CO_2 . Des canaux efficaces de migration des électrons entre le photoabsorbeur et le catalyseur peuvent améliorer considérablement les activités de réduction du CO_2 . La réduction du CO_2 par la CEP en est encore à ses débuts. Les catalyseurs à base de

métaux nobles, tels que les nanoparticules ou les alliages à base d'Au, restent les cocatalyseurs les plus étudiés en raison de leur activité et de leur sélectivité élevée pour le CO. En outre, les catalyseurs moléculaires à base de Ru et de Re ont également été largement étudiés. Outre les métaux nobles, peu de travaux ont été consacrés aux catalyseurs non nobles. Les matériaux à base de cuivre sont les catalyseurs non nobles les plus développés en raison de leur grande abondance et de leurs caractéristiques uniques pour la production d'hydrocarbures. L'utilisation de matériaux semi-conducteurs comme photoélectrodes combinés à un catalyseur moléculaire à base de métaux non nobles pour obtenir une réduction hautement efficace et sélective du CO₂ dans l'eau reste un défi de taille. Dans mon travail, j'ai voulu contribuer à la conception de systèmes PEC plus efficaces pour la réduction du CO₂ en solution aqueuse avec des photoélectrodes stables et l'utilisation de complexes de métaux non nobles. Les matériaux photovoltaïques (PV) convertissent l'énergie lumineuse en électricité en utilisant des matériaux semi-conducteurs qui présentent un effet photovoltaïque.

Les dispositifs CIGS (cellules polycristallines de chalcopyrite Cu(In,Ga)Se₂) sont considérés comme faisant partie des dispositifs à couches minces les plus prometteurs. Tout d'abord, les dispositifs à couches minces CIGS sont assez efficaces. En outre, le coût des modules CIGS a encore diminué grâce à la réduction des coûts de fabrication et à l'augmentation de la production. Le CIGS est un semi-conducteur multi-éléments qui peut être déposé sur des substrats flexibles en métal ou en polyimide. Il est largement utilisé dans les cellules solaires en raison de sa grande résistance aux rayonnements. La cellule CIGS est généralement constituée d'une couche de CIGS de

type p qui joue le rôle de principal absorbeur de lumière, en contact avec une couche de CdS de type n pour former une jonction p-n. Sur la face avant, une électrode transparente généralement basée sur une bicouche ZnO/ZnO:Al collecte les électrons. Une électrode en molybdène est fabriquée sur la face arrière du CIGS pour collecter les trous. Cette structure n'est pas fixe et pourrait être ajustée pour s'adapter à des problèmes spécifiques ou pour atteindre des rendements élevés.

Dans la première partie de mon travail, nous avons démontré avec succès l'application de la photocathode CIGS pour la réduction catalytique du CO₂ par voie solaire. Pour le couplage avec le CIGS, un catalyseur moléculaire de quaterpyridine de cobalt a été fonctionnalisé avec deux groupes d'acide phosphonique (Co-qPyH). Cela permet l'immobilisation sur les surfaces d'oxyde métallique. Il a été démontré que l'acide phosphonique est l'un des groupes de liaison les plus stables à la surface d'un oxyde métallique. Des couches de TiO₂ mésoporeux ont été déposées sur des substrats en verre conducteur FTO par une méthode de sérigraphie, ce qui est désigné comme m-TiO₂|FTO. Ensuite, le catalyseur Co-qPyH a été immobilisé sur la surface du TiO₂. Des mesures détaillées ont été effectuées pour étudier l'immobilisation du catalyseur. Des spectres d'absorption UV-visible ont été réalisés sur la surface du m-TiO₂|FTO avant et après l'immobilisation du catalyseur sur les couches de TiO₂, ce qui a confirmé que la surface semi-conductrice avait été modifiée. En outre, seule une petite quantité d'absorption a été observée dans la région de la lumière visible, rendant la surface presque transparente à la majorité de la lumière entrante. D'autres analyses par spectroscopie infrarouge à réflectance totale atténuée (ATR-IR) sur la poudre de Co-

qPyH et l'électrode m-TiO₂ chargée de Co-qPyH (CoqPyH|m-TiO₂) indiquent une immobilisation réussie du catalyseur sur la surface du TiO₂. Le résultat de la cartographie EDX révèle une distribution homogène du catalyseur sur la surface de l'électrode. En outre, la cartographie de l'élément Co a indiqué qu'il n'y avait pas d'agrégation du cobalt. Le rapport atomique constant du phosphate et du cobalt est de 2:1, confirmant à la fois la présence du catalyseur et son intégrité après immobilisation. Une électrolyse à long terme a été réalisée à -0,51 V vs. RHE pendant 2 h, ce qui a montré un courant catalytique moyen de 1,2 mA.cm⁻². Les produits ont été étudiés par chromatographie en phase gazeuse (GC), indiquant la production de CO avec une sélectivité de 80% et une efficacité faradique de 63%. Un seul sous-produit, le H₂, a également été détecté. L'intégrité du catalyseur avant et après l'électrolyse (1 h) dans du KHCO₃ 0.1 M saturé de CO₂ (pH 6.8) à -0.56 V vs. RHE a été étudiée par l'analyse ATR-IR de l'électrode, ne montrant presque aucun changement des signaux caractéristiques. Ceci indique une bonne stabilité du catalyseur et une immobilisation efficace. Compte tenu des bonnes performances de l'électrode Co-qPyH|m-TiO₂ dans les conditions de la CE, nous avons alors pensé à combiner ce matériau comme couche supérieure avec le CIGS comme photocathode pour réduire le CO₂ sous irradiation lumineuse. Nous avons proposé une stratégie étape par étape de la configuration PV-EC à la configuration PEC. Nous avons d'abord conçu une stratégie qui consiste à coupler une cellule PV CIGS externe (matériau ZnO:Al|ZnO|CdS| CIGS|Mo) avec l'électrode Co-qPyH|m-TiO₂ ci-dessus. Le couplage d'une cellule PV à un électrolyseur (PV-EC) est une méthode pratique pour utiliser les charges photogénérées dans les

dispositifs de la cellule et activer un substrat en solution. Dans cette configuration, le matériau photoactif n'est pas directement en contact avec la solution d'électrolyte, ce qui résout en partie le problème de la stabilité. Des expériences d'électrolyse ont été réalisées dans du KHCO_3 0,1 M saturé de CO_2 (à pH 6,8) à 0,14 V vs RHE pendant 2 h avec une densité de courant moyenne d'environ $1 \text{ mA}\cdot\text{cm}^{-2}$ (par surface géométrique de TiO_2). Une autre électrolyse a été réalisée à -0.06 V vs. RHE dans les mêmes conditions d'électrolyte. Une densité de courant moyenne de $3,25 \text{ mA}\cdot\text{cm}^{-2}$ (par surface géométrique de TiO_2) a été obtenue. L'analyse par GC indique que le produit principal est le CO avec une sélectivité de 87 % à un potentiel de polarisation de -0,06 vs RHE, correspondant à un potentiel plus négatif que le potentiel thermodynamique (surpotentiel formellement négatif $\eta = -50 \text{ mV}$). Une électrolyse de plus longue durée, 7 h, a ensuite été réalisée dans un électrolyte de KHCO_3 0,5 M avec un flux continu de CO_2 (pH 7,2) à un potentiel de -0,03 V vs RHE correspondant à un surpotentiel formellement négatif ($\eta = -80 \text{ mV}$) pour la réaction CO_2 vers CO. Une densité de courant moyenne de $1,78 \text{ mA}\cdot\text{cm}^{-2}$ a été observée et la sélectivité pour la production de CO a été maintenue entre 82 et 85% au cours de l'expérience. Dans la deuxième approche, nous avons greffé le catalyseur directement sur la photocathode à base de CIGS afin de réduire le CO_2 dans un processus PEC entièrement intégré. Plus précisément, une couche de TiO_2 a été déposée directement sur le dispositif CIGS complet ($\text{ZnO:Al/ZnO/CdS/CIGS/Mo}$), puis greffée avec le catalyseur Co-qPyH. La stabilité de la photoélectrode a été évaluée par une expérience de photoélectrocatalyse à long terme réalisée dans un électrolyte de KHCO_3 0,1 M saturé en CO_2 (pH 6,8) à un

potentiel de polarisation de $-0,06$ V par rapport au RHE. La densité de courant moyenne était de $0,8 \text{ mA.cm}^{-2}$ avec seulement une légère décroissance au cours de 2 h. Les produits ont été analysés par GC, qui montre une sélectivité de 97% pour le CO et 3% pour le seul sous-produit H_2 . Avec cette configuration, il est possible d'obtenir une sélectivité élevée pour la génération de CO pendant plusieurs heures. Le TON pour le CO supérieur à 8000 a été obtenu, correspondant à un TOF de $1,1 \text{ s}^{-1}$. Il convient de mentionner que cette étude a conduit au développement du premier dispositif PEC présentant une activité photoélectrocatalytique élevée en solution aqueuse et une sélectivité élevée pour le CO. Contrairement à d'autres systèmes PEC de réduction du CO_2 précédemment rapportés, y compris ceux utilisant des métaux nobles, notre travail montre une performance pionnière. Dans cette étude, nous présentons le premier rapport sur le semi-conducteur CIGS comme composant de la photocathode avec un catalyseur moléculaire pour la réduction du CO_2 en milieu aqueux. Cela ouvrira la possibilité d'une photocathode plus performante pour la réduction PEC du CO_2 .

Dans la deuxième partie, nous avons montré des résultats prometteurs avec la combinaison d'une cellule PV CIGS avec un catalyseur moléculaire déposé sur une électrode en carbone pour réaliser la réduction solaire assistée du CO_2 en CO et ensuite en méthanol en milieu aqueux. Nous avons étudié le découplage du processus de réduction du CO_2 en méthanol afin de maximiser l'efficacité, en réalisant d'abord la réduction du CO_2 en CO dans des conditions optimisées dans une cellule électrochimique, puis en utilisant le CO comme réactif dans une seconde cellule photoélectrochimique, en solution aqueuse (conditions basiques). Dans un système PV-

EC, nous avons combiné avec succès une électrode en papier carbone chargée d'un catalyseur de phtalocyanine de cobalt et une cellule PV CIGS pour conduire la réduction du CO en méthanol. Dans ce système PV-EC, la partie électrochimique est uniquement basée sur des éléments abondants (carbone, complexe de cobalt) et est opérationnelle à pression et température ambiantes, le catalyseur moléculaire employé appartenant à un composé déjà utilisé industriellement (phtalocyanine de cobalt). La cellule PV CIGS fournit une grande tension photovoltaïque à l'unité EC. Un rendement faradique de 21% pour le méthanol a été obtenu avec un potentiel de polarisation de -0.06 V vs RHE, correspondant à un surpotentiel de 240 mV. Les performances du système dépendent de l'adéquation de la surface entre le CIGS et l'électrode en papier carbone. Une électrolyse de longue durée (7 h) a montré une perte d'activité progressive mais faible au cours du temps, et l'origine du méthanol produit a été confirmée par des expériences de marquage isotopique.

Ce travail ouvre la voie au développement de systèmes plus efficaces pour la réduction PEC du CO₂. En raison de la complexité du système de réduction solaire, les performances sont contrôlées par plusieurs facteurs, notamment l'absorption de la lumière, le transfert de charge, l'activité catalytique et les techniques d'ingénierie. La capacité à concevoir une photoélectrode efficace et stable intégrant des catalyseurs moléculaires, permettant de synchroniser correctement dans le temps et l'espace toutes les étapes du processus, reste cependant un défi.

Mots clefs : Réduction photoélectrochimique du CO₂, catalyseur moléculaire, CIGS, cobalt quaterpyridine, phtalocyanine de cobalt

Abstract

CO₂ reduction is an environmentally friendly and economically meaningful strategy with significant benefits, but it is still a challenge. The use of abundant solar energy to convert CO₂ into value-added chemicals through photo-electrocatalysis technology has attracted widespread attention from researchers in chemistry, materials, and environmental science. Photoelectrochemical (PEC) reduction of CO₂ can integrate and optimize the advantages of both photocatalysis and electrocatalysis for improved conversion efficiency and selectivity. In this doctoral work, I have: (i) combined a p-type Cu(In,Ga)Se₂(CIGS) semiconductor material with cobalt quaterpyridine molecular catalyst. Pure carbon dioxide dissolved in aqueous solution (pH 6.8) is converted to carbon monoxide under visible light illumination with partial current density above 3 mA cm⁻² and 97% selectivity, showing good stability over time. (ii) developed a new system, consisting in a CIGS unit linked to a carbon electrode loaded with cobalt phthalocyanine as molecular catalyst, able to achieve the CO₂ reduction to CO and then to methanol in aqueous media. Under ideal conditions, the CO₂-to-CH₃OH reaction shows a global Faradaic efficiency of 28 % and chemical selectivity of 11.6 %.

Keywords: CO₂ photoelectrochemical reduction, molecular catalyst, CIGS, cobalt quaterpyridine, cobalt phthalocyanine

Résumé

La réduction du CO₂ est une stratégie respectueuse de l'environnement et économiquement pertinente, qui présente des avantages considérables, mais elle reste un défi. L'utilisation de l'abondante énergie solaire pour convertir le CO₂ en produits chimiques à valeur ajoutée grâce à la photoélectrocatalyse, a attiré l'attention des chercheurs en chimie, en matériaux et en sciences environnementales, et de l'environnement. La réduction photoélectrochimique (PEC) du CO₂ peut intégrer et optimiser les avantages de la photocatalyse et de l'électrolyse pour améliorer l'efficacité et la sélectivité de la conversion. Dans ce travail de doctorat, j'ai : (i) combiné une structure de type p-Cu(In,Ga)Se₂(CIGS) de type p avec un catalyseur moléculaire de quaterpyridine de cobalt. Le dioxyde de carbone pur dissous dans une solution aqueuse (pH 6.8) est converti en monoxyde de carbone sous l'éclairage de la lumière visible avec une densité de courant partielle supérieure à 3 mA cm⁻² et une sélectivité de 97%, montrant une bonne stabilité dans le temps. (ii) développé un nouveau système, consistant en une unité CIGS liée à une électrode de carbone chargée de phtalocyanine de cobalt comme catalyseur moléculaire, capable de réaliser la réduction du CO₂ en CO et ensuite en méthanol en milieu aqueux. Dans des conditions idéales, la réaction du CO₂ au CH₃OH présente une efficacité faradique globale de 28 % et une sélectivité chimique de 11,6 %.

Mots clefs : Réduction photoélectrochimique du CO₂, catalyseur moléculaire, CIGS, cobalt quaterpyridine, phtalocyanine de cobalt

Contents

Résumé en français	1
Abstract.....	9
Résumé.....	10
Chapter 1 - Introduction.....	13
1.1 Photoelectrochemical reduction of CO ₂ : towards a sustainable future.....	13
1.1.1 Principles and advantages of Photoelectrochemical reduction of CO ₂ .	14
1.1.2 Semiconductors as photoelectrodes	16
1.1.3 Thermodynamics and chemical pathways of PEC CO ₂ reduction.....	24
1.2 Photoelectrochemical CO ₂ -reduction at semiconductor/ metal-complex systems.....	30
1.2.1 Group IV Materials	30
1.2.2 Group III-V Materials	32
1.2.3 Oxide Semiconductors	33
1.2.4 Chalcogenide Semiconductors.....	36
1.2.5 CO ₂ Reduction on Multi-semiconductor Systems	36
1.4 Motivation and outline of this thesis.....	39
Chapter 2 - Photocathode functionalized with a cobalt-based molecular catalyst for 2-electron CO ₂ reduction in water.....	41
2.1 Structure and properties of Cu(In,Ga)Se ₂ materials	41
2.2.1. Structure of a standard CIGS solar cell.....	44
2.1.2 The Mo/CIGS/CdS/ZnO heterojunction	49
2.2 Quaterpyridine complexes with CO ₂ reduction	50
2.2.1 Quaterpyridine complexes for electrocatalytic reduction of CO ₂	50
2.2.2 Quaterpyridine complexes for photocatalytic reduction of CO ₂	51
2.3 Functionalization of cobalt quaterpyridine	53
2.3.1 Cobalt quaterpyridine synthesis and functionalization	53
2.3.2 Immobilization of modified cobalt quaterpyridine on TiO ₂	54
2.3.3 Electrochemical performance for CO ₂ reduction.....	58
2.4 Photovoltaic-electrochemical performance of CIGS and functionalized TiO ₂	61
2.4.1 Photocathode assembly and characterizations	61
2.4.2 PV-EC system for CO ₂ reduction.....	64
2.5 Photo-electrochemical performance of CIGS with Cobalt Quaterpyridine	66
2.5.1 Photocathode assembly and characterizations	66
2.5.2 Photo-assisted CO ₂ reduction performance	67
2.6 Conclusions and perspectives	69
Chapter 3 - Photo-assisted CO ₂ reduction to methanol on a porous carbon-cobalt molecular catalyst electrode with the assistance of CIGS photovoltaic material	74
3.1 CO ₂ reduction to methanol.....	74
3.2 Cobalt phthalocyanine complexes	76
3.3 Photo-assisted reduction of CO ₂ to methanol	77
3.3.1 CIGS cell characterizations.....	78

3.3.2 Preparation of porous carbon-CoPc electrode	80
3.3.3 Photo-assisted electrolysis cell assembly.....	80
3.4 Photovoltaic-Electrochemical performance for CO ₂ reduction	80
3.4.1 CO ₂ as reactant.....	81
3.4.2 CO as reactant	82
3.4.3 Labeled experiments	84
3.4.4 Effects of area ratio of S _{carbon electrode} and S _{CIGS}	86
3.4.5 Long-term stability investigation.....	87
3.5 Overall efficiency approach	89
3.6 Conclusions and perspectives	90
Chapter 4 - Preliminary investigation of PEC CO ₂ reduction on p-GaP semiconductors associated with molecular catalysts	94
4.1 PEC reduction of CO ₂ on GaP semiconductors	94
4.2 HER performance of p-GaP based photoelectrode	96
4.2.1 Preparation of photoelectrode	96
4.2.2 Hydrogen evolution reaction at bare GaP photoelectrode	96
4.3 Homogeneous PEC reduction of CO ₂ on GaP based photoelectrode with molecular catalyst	98
4.3.1 Preliminary experiments in aqueous solution.....	98
4.3.2 Preliminary experiments in acetonitrile	100
4.4 Perspectives.....	101
Chapter 5 - General conclusions and perspectives	102
5.1 General conclusions	102
5.2 Future perspectives	104
Chapter 6 - Experiments and Methods.....	106
6.1 Chemicals and synthesis	106
6.1.1 Commercial chemicals.....	106
6.1.2 Synthesis and purifications	107
6.2 Characterization Methods	112
6.2.1 Solar simulator	112
6.2.2 UV-visible spectroscopy	112
6.2.3 Attenuated Total Reflection (ATR-IR) spectroscopy	113
6.2.4 Inductively coupled plasma – Optical Emission Spectroscopy (ICP - OES)	113
6.2.5 X-ray photoelectron spectrometer (XPS).....	113
6.2.6 pH measurements.....	113
6.2.7 Nuclear magnetic resonance (NMR) spectroscopy.....	113
6.2.8 Gas chromatography (GC).....	114
6.2.10 <i>J(V)</i> curve measurement.	117
References.....	118

Chapter 1 - Introduction

1.1 Photoelectrochemical reduction of CO₂: towards a sustainable future

Earth's climate has changed throughout history. Scientific evidence for warming of the climate system is unequivocal. This current global warming trend is the result of human activity since the mid-20th century and is proceeding at a rate that is unprecedented [1, 2]. Recent studies from NASA have shown that most of the warming occurred in the past 40 years, and the years 2016 and 2020 have been the warmest years [3]. The average surface temperature of our planet has risen about 2.12 degrees Fahrenheit since the late 19th century, which is mainly driven by increased carbon dioxide emissions into the atmosphere [4]. Recent study points out that anthropogenic CO₂ levels could reach ~590 ppm by the year 2100, which will lead to an increase in the global temperature of 1.9°C and would severely impact the survival of all living beings [5].

Therefore, in order to avoid the worst effects of climate change, the world needs to urgently reduce CO₂ emissions. However, the way this responsibility is shared among regions, countries and individuals has always been an endless point of contention in international discussions. Over-reliance on fossil fuels has not only accelerated the over-exploitation of natural resources, it has also interrupted the carbon cycle [6]. Nature converts carbon dioxide into carbohydrates through photosynthesis to maintain the carbon cycle, but this is greatly affected by deforestation, industrialization and

urbanization. It is grateful that most countries have been shifting towards low-carbon sources of energy – nuclear and renewable technologies [6]. Renewable and sustainable energy will play a key role in the decarbonization of our energy systems in the coming decades. CO₂ capture and utilization (CCU) has attracted plenty of attention. Various research efforts have been made in the past decades. Consequently, the recycling or conversion of CO₂ into fuels and other valuable products is an attractive strategy to help mitigating the global warming and energy crisis.

1.1.1 Principles and advantages of Photoelectrochemical reduction of CO₂

Solar energy is the most abundant renewable and clean energy source. It can be used in a large scale by efficiently converting solar energy into “electronic” energy through producing separated electron-hole pairs. One direct method to achieve this conversion is collecting the photogenerated electrons and holes to produce electricity with photovoltaic cells. However, it is still a challenge to store electricity on a massive scale, while its transport is associated to important losses. Thus, electrical energy is not ideal because of the problems of large-scale use and long-distance transportation. Enlightened by natural photosynthesis, another strategy has emerged: converting solar energy into chemical fuels (storing energy in chemical bonds). This can be achieved by utilizing the electricity produced from solar energy to drive electrocatalytic reactions in an indirect way or generating chemicals through photoelectrocatalytic reactions in a direct way (Figure 1.1).

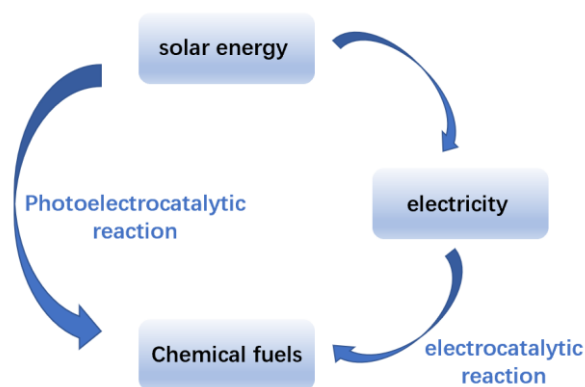


Figure 1.1 Two pathways for the conversion of solar energy-to-chemical fuels.

Photoelectrochemical (PEC) reduction of CO₂ is driven by electricity and light irradiation. This appealing technology mimics Nature’s energy cycle so it is also called artificial photosynthesis. PEC includes several benefits such as controllable selectivity of products and environmentally friendly use of renewable solar energy. It can achieve high efficiency and selectivity due to the integration and optimization of the advantages of both electrocatalysis and photocatalysis. Photocatalytic reduction of CO₂ has received growing attention during the past decades. The design of highly selective and efficient systems for photocatalytic CO₂ reduction still remains a grand challenge. Three main aspects are essential for photocatalytic reduction of CO₂: a. solar-light absorbing and charge generation, b. charge separation and transportation, and c. surface reaction of charge carriers. In these processes, photogenerated electrons and holes would probably be consumed through recombination. Because of efficient light adsorption and charge separation, PEC reduction of CO₂ could lead to improved solar conversion efficiency as compared to particle suspension-based photocatalytic process.[7]

A key element for PEC CO₂ reduction process is the photoelectrode. A

photoelectrode consists in a photo absorber and a catalyst for reducing CO₂. Efficient electron migration channels between photo absorber and catalyst could greatly enhance the activities of CO₂ reduction.

The PEC reduction of CO₂ at a photoelectrode with a co-catalyst (for example a metal complex) needs multiple electron transfers and various products could be generated according to the transfer of electrons and protons and specific reaction route. Carbon monoxide, formic acid, formaldehyde, methanol, and methane have all been detected in some systems even at ambient temperature and pressure [8, 9]. The product yield of PEC reduction of CO₂ is mainly governed by the choice of photoelectrode materials, catalyst and electrolytes. Figure 1.2 illustrates the principle scheme of PEC CO₂ reduction using solar light as the main energy source.

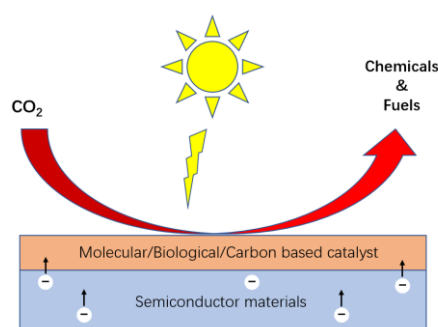


Figure 1.2 Scheme of the PEC CO₂ reduction into chemicals fuels under solar light irradiation.

1.1.2 Semiconductors as photoelectrodes

Semiconductors are crystalline solids with intermediate electrical conductivity between a conductor and an insulator and which are widely used in the manufacture of various kinds of electronic devices. According to theory, the band structure of a solid

material consists of multiple energy bands, similar to the energy levels of electrons in atoms. Electrons occupy lower energy bands first and can occupy higher energy bands upon excitation. The highest filled band, occupied by electrons in the ground state, is called the valence band (VB). The band above the and gap is the conduction band (CB), which is unoccupied at $T = 0$ K. The energy gap between VB and CB is called band gap (the electrons cannot fill it). Figure 1.3 shows the energy bands structure of a typical semiconductor material. The conductivity of such material is determined by the number of electrons contained in the conduction band. When electrons gain energy from the VB and are promoted to the CB, they can freely move through the band to conduct electricity. Generally, metal materials have negligible energy gap between the CB and VB. At room temperature, electrons can easily gain energy and jump to the CB to conduct electricity. Insulating materials have a large energy gap (usually > 9 eV), so it is difficult for electrons to reach the CB. The energy gap of semiconductor materials is typically in the range $1 \sim 4$ eV, leading to an intermediate behavior between conductors and insulators. Therefore, as long as the appropriate conditions of energy excitation are supplied, or the energy gap is decreased, the material can conduct electricity.

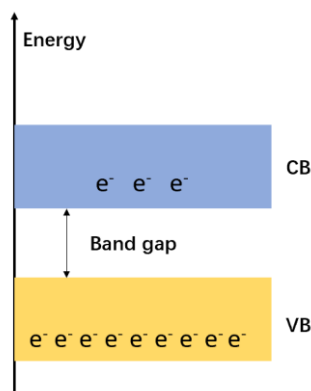


Figure 1.3 Energy bands structure of a semiconductor material.

Therefore, semiconductors are considered as attractive materials for light-absorbing applications. When a photon has an energy higher or equal to the band gap, it could be absorbed. Once absorbed, an electron would be excited from the VB to the CB, thereby leaving behind an empty state that is called a hole. This means that, in a semiconductor, the number of both electrons and holes under light illumination are larger than in the equilibrium state. After the separation, the electrons and holes can recombine or they may transfer to the surface of the semiconductors and eventually migrate to adsorbed molecules, and then initiate the reduction or oxidation reactions (Figure 1.4).

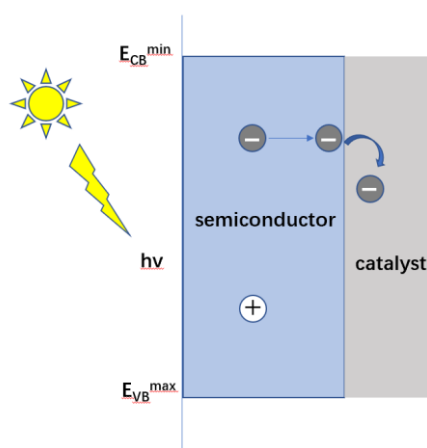


Figure 1.4 Migration of a photoexcited electron from a semiconductor to a catalyst.

The practical reaction sites would be located either on the surface of the semiconductor, or on the surface of other semiconductor materials or co-catalyst such as metal nanoparticles (NPs) or molecular catalyst. Therefore, the most important role of the semiconductor in PEC reduction of CO_2 is to absorb light, generate the electron–hole pairs, and promote their separation and migration. The catalytic aspect of the process is usually an extra function which is mainly performed by a catalytic material.

Recombination of Charge Carriers

After light excitation, the formation of charge carriers, electron and hole pairs, is usually followed by some deactivation routes (Figure 1.5). The effective donation of the electrons or holes to the acceptor molecules at the surface will lead to the desired redox reactions (routes 1 and 2), while these processes compete with several recombination pathways. The carriers can be trapped and consumed by their counterparts with opposite charge on the surface (routes 3), or recombine with other carriers inside the bulk of the material (routes 4) [7]. These recombination reactions reduce the efficiency of the catalytic reaction. Several factors have been showed to affect the recombination rates, e.g. transfer and trapping of charges, defect (doping) density of the crystal [10, 11] as well as possible combination with another material which may play the role of an electron or a hole sink [12].

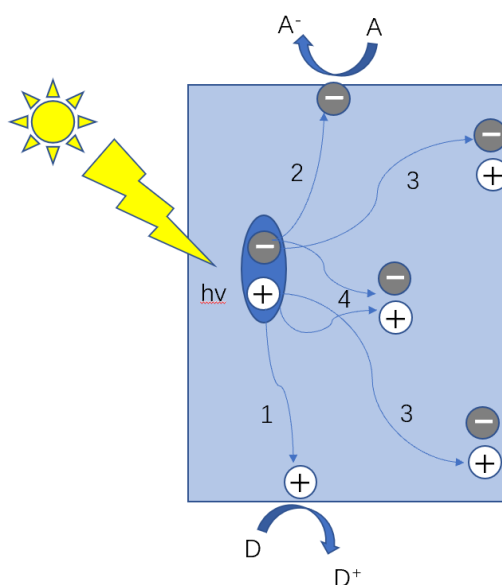


Figure 1.5 Recombination of photoexcited electron-hole pair in a semiconductor material. A = electron acceptor, D = electron donor.

Both recombination processes have negative effects on the efficiency of the

photocatalytic reaction. An example of metal catalyst supported on the semiconductor is described here (as shown in Figure 1.4). In a material, the chemical potential is defined by Fermi level (E_F), which is a thermodynamic quantity and can be used for analysis of electron transfer at material interfaces. In the case in Figure 1.4, the photoexcited electrons are transferred towards the metal because the E_F energy lies below the CB states. This process finally changes the E_F of the composite. Therefore, the electrons can be transported towards the adsorbate more easily compared with semiconductor itself. In another words, the composite is more reductive. This strategy could promote the separation of electron-hole pairs by promoting migration of electrons towards the metal, while the holes are still in the semiconductor. Finally, improved separation of charge carriers would lead to less recombination and an increased efficiency of the reactions. [7]

p-n Junction in semiconductor materials

Introducing p-n junction is an efficient way to improve the separation of charge carriers. n-type semiconductors are semiconductors doped with an electron donor element during preparation. The term n-type refers to the negative charge of the electron. In n-type semiconductors, electrons are the majority carriers and holes are the minority carriers (Figure 1.6 a). On the contrary, p-type semiconductors are doped with an electron acceptor element and the term p-type comes from the positive charge of a hole. In p-type semiconductors, holes are the majority carriers with a larger hole concentration than electron concentration (Figure 1.6 b)[13].

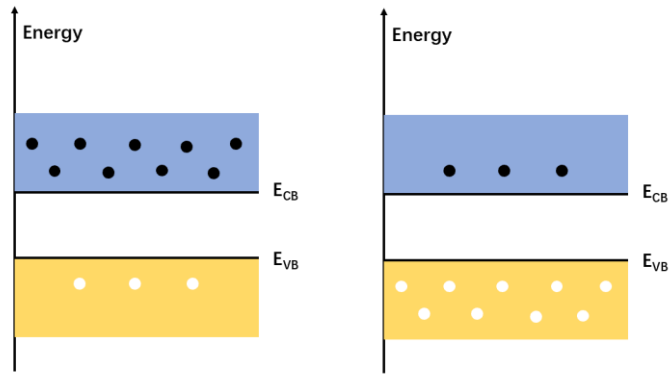


Figure 1.6 Band structure of an (a) n-type semiconductor and an (b) p-type semiconductor. Dark dots in the CB are electrons and light dots in the VB are holes.

A p-n junction is the interface or the boundary between a p-type and a n-type semiconductor. As described above, the p-type side contains an excess of holes, while the n-type side contains an excess of electrons as the main carriers. When illuminated with light, the p-n junction can drive a current which could pass through the junction in one direction only [14]. Specifically, there are two different types of current generated at the p-n junction: the drift current and the diffusion current, which flow in opposite directions. Under “dark” conditions (e.g., without illumination), these currents balance each other and no net current flows. At the microscopic level, the drift current originates from the internal electric field created at the interface of the p-type semiconductor and the n-type semiconductor. The diffusion current originates from the disparate carrier concentrations in the n-type and p-type regions, with electrons tending to diffuse from the higher electron concentration region (n-type semiconductor) towards the lower electron concentration region (p-type semiconductor). Similar action, though in the opposite directions, occurs for the holes. Under illumination, the drift current becomes greater than the diffusion current, thus facilitating the separation of electron-hole pairs.

Improved separation contributes to slower recombination rates and an increased efficiency of the drift current. When a bias potential is applied to the semiconductor with a p-n junction, such as in solar cell, in a band theory model, more carriers would get into the CB and then enter the region where the electric field is located [13, 15].

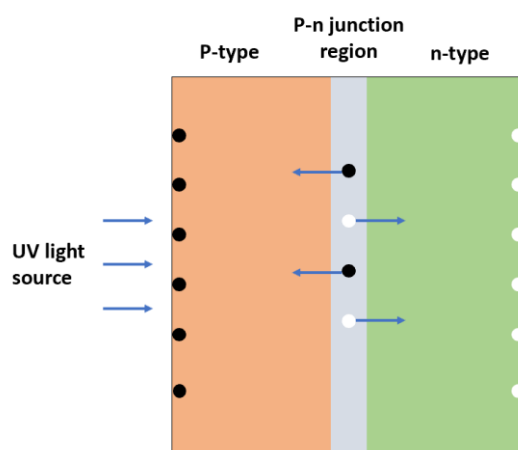


Figure 1.7 Principle of the p-n junction in semiconductors. Dark dots are electrons and light dots are holes.

p-n junction may be created by doping, for example by ion implantation, diffusion of dopants, or by epitaxy (growing a layer of crystal doped with one type of dopant on top of a crystal layer doped with another type of dopant). If two different types of material are used, this would introduce a grain boundary between the semiconductors that would severely inhibit its efficiency by scattering the electrons and holes.

In a photocatalytic system, the semiconductor not only acts as a light absorber but also play a role for photocatalysis as well. From a thermodynamic point of view, the ability to transport photogenerated charge carriers in a semiconductor to the adsorbed catalytic molecular sites is mainly dominated by the alignment of the Fermi levels and the redox potentials of the molecule (Figure 1.8) [16], whereas it is generally believed

that these levels are situated very close to the edges of CB and VB, respectively, especially for n-type semiconductors. The electron transfer reaction is mostly affected by the position of the band edges. It should be noticed that the redox potential goes from positive to negative, while energy goes in the opposite way. Therefore, in reduction processes, the potential level of the CB must be more negative than the reduction potential of the absorbed molecule. Similarly, for oxidation reactions, a photoexcited hole transfer from the semiconductor material to the acceptor molecule equivalent to the migration of an electron through the opposite way. This process needs the potential level of the highest occupied molecular orbital (HOMO) of the absorbed molecule to be more negative than the VB potential of the semiconductor [7].

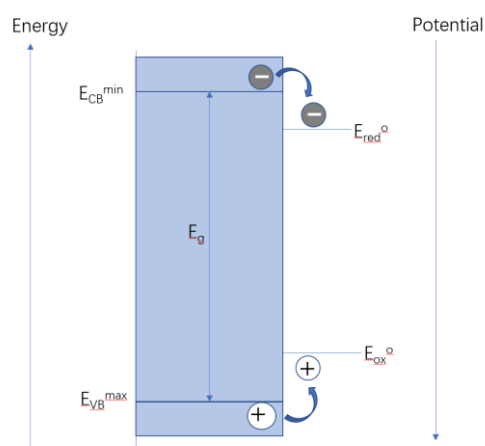


Figure 1.8 Thermodynamic constraints on the migration of electron and hole to the absorbed molecules.

These thermodynamic limitations indicate that the exact energy positions of band edges play a vital role in the application of each semiconductor materials in photocatalytic process. A suitable semiconductor needs to meet two opposite conditions. On one hand, considering a high efficiency, it is beneficial that the semiconductor

material absorbs light in the visible range, so a small band gap is necessary for this condition. On the other hand, the band gap must span the range of the oxidation or reduction potentials corresponding to the catalyst and catalyzed reaction. These requirements regarding the width of the band gap actually limit the application of semiconductor material, while optimization approaches are explored through sensitization or band-gap engineering.

Regarding specifically PEC reduction of CO₂, semiconductors primarily act as the photo absorber and are functionalized with cocatalyst, such as metal nanoparticles or molecular catalyst. An ideal semiconductor photocathode will efficiently harvest solar light and transfer charge carriers to the catalytic sites for efficient reduction reactions. Hence, a semiconductor with relatively small band gap and highly efficient electron-migration channel between photo absorber and catalysts will be beneficial for CO₂ reduction.

1.1.3 Thermodynamics and chemical pathways of PEC CO₂ reduction

The electrochemical standard reduction potentials for C1 products and ethanol are summarized below in Table 1, and are in the same order of magnitude than the proton reduction reaction. Moreover, the potentials are less negative than the CB of various semiconductor materials [18] (as illustrated in Figure 1.9), so these reactions are theoretically feasible. In PEC systems, the energy of photoexcited electrons is normally determined by the conduction band edge (CBE) of the semiconductor photoelectrode. Thermodynamically, CO₂ photoreduction is favorable if the energy of the CBE is more

negative than that of the reduction potential. The single-electron process from CO_2 to its anion radical $\text{CO}_2^{\bullet-}$ has a quite negative reduction potential of -1.9 V vs. standard hydrogen electrode (SHE) at pH 7 (Figure 1.8). This step is highly unfavored, because nearly no semiconductor material could provide sufficient potential to transfer a photogenerated electron to a CO_2 molecule [18]. Utilization of a multiple proton-coupled electron transfer process significantly lowers the potential required for CO_2 reduction, and gives various products that depend on the number of electrons involved.

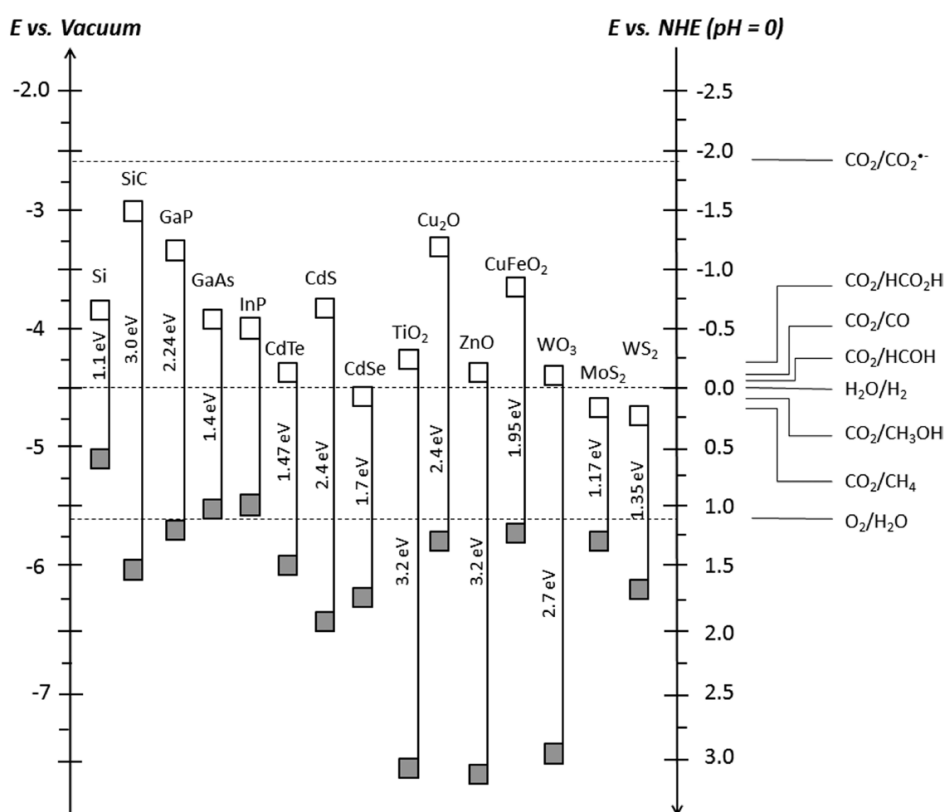


Figure 1.9 CB (white squares) and VB (gray squares) potentials of some commonly used semiconductors, with the potentials of several CO_2 and water redox couples at pH 0, plotted versus vacuum (left) and NHE (right). [17]

The multistep reduction into C1 products involves up to eight electrons and protons (for methane), with the breaking of C–O bonds and the formation of C–H bonds,

and may lead to various products depending on the specific pathway taken. Besides, considering the reduction of CO₂ is generally performed in the presence of water, the competing generation of molecular hydrogen would compete with carbon species for the photoexcited electrons, so it is quite important to suppress this concurrent pathway. Thus, an in-depth understanding of the mechanisms is mandatory to minimize the relevant thermodynamic and kinetic barriers of the intermediate reactions, thereby increasing the overall rate of CO₂ reduction.

Table 1.1 Apparent standard redox potentials ($E^{\circ'}$) relative to the Standard Hydrogen Electrode (SHE) at pH 7

Reaction	$E^{\circ'}$ vs SHE (V)	
$\text{CO}_2 + 2\text{H}^+ + 2\text{e}^- \rightarrow \text{HCOOH}$	-0.61 V	(1)
$\text{CO}_2 + 2\text{H}^+ + 2\text{e}^- \rightarrow \text{CO} + \text{H}_2\text{O}$	-0.53 V	(2)
$\text{CO}_2 + 4\text{H}^+ + 4\text{e}^- \rightarrow \text{HCHO} + \text{H}_2\text{O}$	-0.48 V	(3)
$\text{CO}_2 + 6\text{H}^+ + 6\text{e}^- \rightarrow \text{CH}_3\text{OH} + \text{H}_2\text{O}$	-0.38 V	(4)
$\text{CO}_2 + 8\text{H}^+ + 8\text{e}^- \rightarrow \text{CH}_4 + 2\text{H}_2\text{O}$	-0.24 V	(5)
$2\text{CO}_2 + 12\text{H}^+ + 12\text{e}^- \rightarrow \text{CH}_3\text{CH}_2\text{OH} + 3\text{H}_2\text{O}$	-0.08 V	(6)
$2\text{H}^+ + 2\text{e}^- \rightarrow \text{H}_2$	-0.41 V	(7)

The variation of the band structure at the semiconductor–electrolyte interface is also an important aspect. Specifically, at a semiconductor–electrolyte solution interface, if the Fermi level (E_F) of the semiconductor is not equal to those of the electrolyte, then electrons will be transferred from high E_F to low E_F . As an example, we may take a p-type semiconductor, with E_F lower than that of the electrolyte solution. When the

photocathode is immersed in the electrolyte, electrons will transfer from the electrolyte to the semiconductor. Therefore, an electric field in the semiconductor near the interface is built up, which will cause a band bending of the semiconductor's energy bands structure. As a result, the semiconductor's CB and VB will bend downward, (Figure 1.10). This band bending promote electrons transport to the photocathode-electrolyte interface. Under light irradiation, some electrons in the VB will be excited to the CB, leaving holes in the VB. The semiconductor's CB/VB bending near the interface supplies a force on electron-hole pairs in opposite directions, driving electrons toward the interface and holes away from that. In others words, this bending facilitates electron-hole pairs separation, which is a critical parameter for photoconversion efficiency that hinges on irreversible separation of charge carriers. This p-type photoelectrode will promote reduction reactions. An n-type semiconductor will act as a photoanode, leading a bending in an opposite direction to the energy bands. This band bending promotes hole transport to the photoanode-electrolyte interface, achieving oxidation of electrolyte molecules (e.g. H₂O). As described above, a PEC system could contain both a p-type photocathode and a n-type photoanode as photoelectrodes simultaneously in a tandem way, or one photoelectrode only with a dark counter electrode.

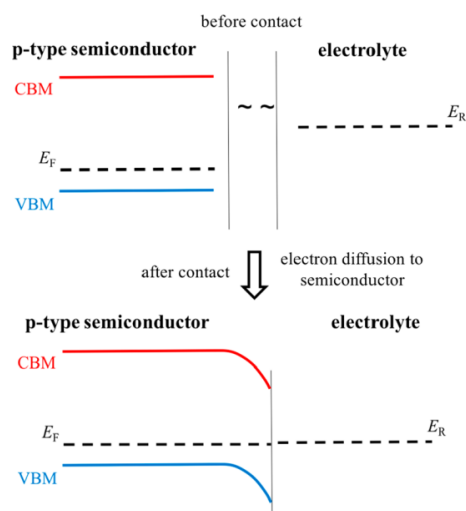


Figure 1.10 Scheme of band bending at the p-type semiconductor/electrolyte interface from ref. [19].

Reactivity at such photocathode-electrolyte interface is hardly controllable, leading to poor selectivity and mediocre stability over time. **In my work, I have mainly focused on the functionalization of semiconductor materials with molecular catalysts for PEC reduction of CO₂ with the objective to associate a stable, efficient photo absorber with an active and selective molecular catalyst.** We also seek to get mechanistic insights from electrochemical studies.

To achieve an efficient photon-induced reduction reaction on a semiconductor photocathode, it is essential to focus on the following aspects:

- 1) Ensure sufficient lifetime of the photoexcited electrons;
- 2) Ensure fast transport of photoexcited electrons and holes in opposite directions, which is essential to photoconversion efficiency;
- 3) Optimize band gap energy: for the photocathode used in the PEC CO₂ reduction, we need to best utilize the solar spectrum and have a sufficiently high CB energy to drive the desired reduction reaction.

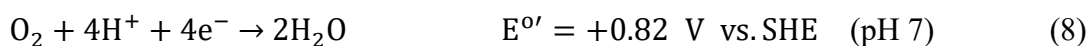
As discussed earlier (Figure 1.3), metal NPs could reduce charge recombination and enhance the separation at the interface of metal–semiconductor. They may also play an important role in catalyzing the subsequent steps and determining the selectivity of the products. [20] Coupling semiconductor with a molecular complex has also been shown to be beneficial for the performance of PEC reduction of CO₂. [19]

The nature of the CO₂ reduction product and selectivity are determined by the chemical composition of the electrocatalyst. The two-electron-reduction product CO is a very important raw material in the chemical industry, especially for the famous Fischer–Tropsch process (synthesis of hydrocarbon fuels). Besides, formic acid (HCOOH) is also a useful compound since it is a hydrogen carrier which got much attention recently. It could be easily decomposed to H₂ and CO₂ in the presence of a suitable catalyst, even under mild conditions [21, 22].

Multi-electron CO₂ reduction is also promising. With a few rare exceptions, molecular catalysts are not yet capable to make such highly reduced products (methanol, CH₄, ethanol, ...). A suitable photoelectrocatalytic CO₂ reduction system should operate in response to visible light and near-infrared light, because these domains account for the majority of the solar spectrum. As in electrocatalytic systems, side reactions should also be suppressed, such as the reduction of protons to H₂ (see Equation 14).

Ideally, water is going to be the electron donor. Since the apparent standard potential associated with the oxidation of water (see Equation 8) is +0.82 V vs. SHE at

pH 7, the minimum photon energy required to cause the photocatalytic reduction of CO₂ on a thermodynamic basis (for the generation of HCOOH, for instance) and to oxidize water is 1.43 eV, which corresponds to a wavelength of approximately 870 nm. Thus, the total range of visible light (400 < λ < 800 nm) can theoretically be used. [23]



Metal complexes associated to semiconductors are promising photocatalysts toward CO₂ reduction to formate, CO, and maybe to various hydrocarbons. In the following sections, some representative examples of photocatalytic CO₂ reduction using metal complexes and semiconductors are introduced.

1.2 Photoelectrochemical CO₂-reduction at semiconductor/metal-complex systems

PEC CO₂ reduction using a p-type semiconductor cathode in the presence of a metal-complex catalyst has been studied since the 1980s, either with a freely diffusing catalyst or upon anchoring the complex to the photoelectrode surface [24-27]. The performance of such semiconductor/metal-complex hybrid systems in aqueous condition could potentially be improved by anchoring water-resistant metal-complex catalysts on the surface of photoelectrode to prevent undesirable aggregation. Obviously, appropriate choice of a semiconductor material is also of great importance.

1.2.1 Group IV Materials

Silicon (Si) has a narrow bandgap of 1.1 eV, allowing the absorption of light to span from the UV region to the near-IR region. Many early studies of PEC reduction of

CO₂ have been performed on Si photoelectrodes also because of its abundance.

Kubiak et al. reported the selective reduction of CO₂ to CO using hydrogen-terminated p-type Si as the photocathode in the presence and homogeneous catalyst Re(bipy-Bu^t)(CO)₃Cl (bipy-Bu^t=4,4'-di-tert-butyl-2,2'-bipyridine) in 0.1 M tetrabutyl ammonium hexafluorophosphate (TBAH) acetonitrile solution (Figure 1.11). [28] The reduction potential required to drive CO₂ to CO conversion on p-Si was found to be 600 mV lower than that for the same reaction on a Pt electrode, with 97 ± 3% Faradaic efficiency at -1.4 V vs. Ag/AgCl. A current density of 31 mA cm⁻² for CO₂ reduction under a monochromatic illumination of 95 mW cm⁻² is noteworthy. Both the H-Si and the rhenium catalyst showed excellent stability, lasting for hours without any sign of degradation.

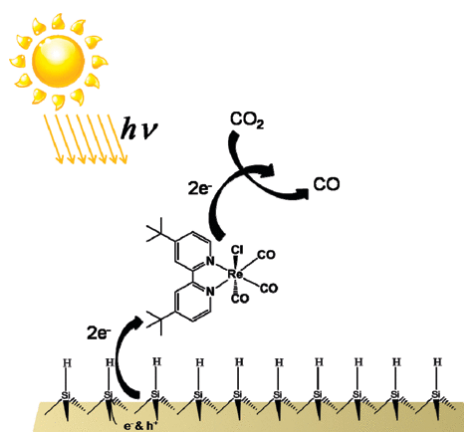


Figure 1.11 Scheme of p-type Si photocathode with Re(bipy-Bu^t)(CO)₃Cl. [28]

In a later study, Torralba-Peñalver et al. reported three Mn-based complexes as homogeneous catalysts for the selective conversion of CO₂ to CO, in combination with a p-type hydrogen-terminated silicon nanowires (SiNWs-H) photocathodes under illumination without losing the intrinsic electrocatalytic activity of the complex.[29] The photocurrent densities measured at -1.0 V vs SCE for [Mn(bpy)

(CO)₃(CH₃CN)](PF₆) at SiNWs-H exceeded 1 mA cm⁻² in CO₂-saturated CH₃CN + 5% v/v H₂O for 3h with a TOF number of 8.

1.2.2 Group III-V Materials

Much efforts have been made in the research of III-V semiconductors used for CO₂ reduction. Among all of the III-V family members, InP, GaP, and GaAs have been the most commonly studied.

Experimental observation of pyridine (Py)-catalyzed CO₂ PEC reduction at p-GaP electrodes was originally reported by Bocarsly and coworkers.[30] They measured almost 96% Faradaic efficiency of CO₂ reduction to methanol at a potential of -0.2 V vs. SCE. It should be noted that it has never been demonstrated that the methanol is issued from CO₂. Moreover, the absence of follow-up studies causes some doubt on the reproducibility of the results.

p-InP is another example of a III-V semiconductor that possesses a bandgap matching the solar spectrum and has thus been studied extensively. A Zn-doped InP (InP-Zn) single crystal modified with a polymerized ruthenium-complex (Figure 1.12) has been reported to serve as a photocathode for the PEC reduction of CO₂, generating formate in aqueous solution under visible-light irradiation.[31] Through the photoelectropolymerization of the mononuclear Ru complex, the Ru complex was immobilized onto the InP-Zn surface. Under visible light irradiation, this Ru-polymer/InP-Zn photocathode could operate in water at a lower potential than that is required in conventional electrocatalysis, with a selectivity for formate of 62.3% at a

bias potential of -0.6 V vs. Ag/AgCl (~0.01 vs. RHE) in water.

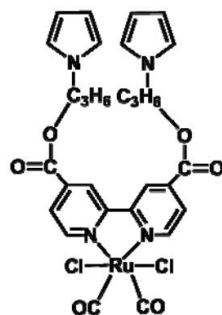


Figure 1.12 The structure of $[\text{Ru}^{\text{II}}(\text{L-L})(\text{CO})_2\text{Cl}_2]$ complex, deposited at a Zn-doped InP upon photo-electropolymerization

It has also been found that other p-type semiconductors, such as $\text{Ta}_2\text{O}_5:\text{N}$, GaP, and $\text{Cu}_2\text{ZnSnS}_4$, can act as competent photocathode for generating formate when paired with a polymerized Ru complex synthesized by chemical polymerization using pyrrole units and FeCl_3 as initiators.[32, 33] Upon polymerization, polypyrrole chains were formed that were stable in electrochemical conditions.[34] Cyclic voltammetry measurements revealed that the E_{red} values of these Ru polymers were almost identical to those of the monomeric analogs.[35] Because of the presence of propyl chains in the Ru polymers, it is believed that this result is caused by negligible electronic interactions between the bpy ligands and the polypyrrole. Therefore, selecting the optimal Ru catalyst is key to maximizing catalytic performance.

1.2.3 Oxide Semiconductors

In general, titanium dioxide (TiO_2) is the most extensively used oxide semiconductors, due to its high photocatalytic stability conditions, low cost, and use in a variety of photocatalytic processes, including water splitting, CO_2 reduction and

degradation of various organic species. Consequently, this material has been widely studied over the past few decades.[18] In PEC CO₂ reduction system, it is commonly combined with other semiconductor materials.

For instance, a Zn and N (Fe₂O₃:Zn,N) co-doped Fe₂O₃ has been reported to be an efficient photocathode device for CO₂ reduction with a p-type Cr₂O₃ underlayer and an n-type TiO₂ used as protecting layer.[35] The combination of Cr₂O₃ and TiO₂ layers dramatically enhanced the cathodic photocurrent in the Fe₂O₃:Zn,N and preventing self-reductive deactivation of the material. By coupling the optimized hybrid photocathode with a SrTiO₃ photoanode, both CO₂ reduction and water oxidation could be achieved without an external electrical bias under light driven (AM1.5G). In this system, for both cathode and anode reactions, nearly 100% overall Faradaic efficiencies could be achieved with formate, CO and H₂ as reduction products and O₂ as the oxidation product. The use of the Ru complex with an electronic network provided by polypyrrole improved the performance and resulted in a stable photocurrent of 150 μAcm^{-2} for 1 h. HCOOH, CO and a small amount of H₂ were generated under 1 sun irradiation with application potential of 0.1 V vs RHE. The selectivity for formate could reach 79% and the solar to chemical energy conversion efficiency was 0.15%, which is close to that obtained with a Ru catalyst/single-crystalline InP:Zn photocathode.

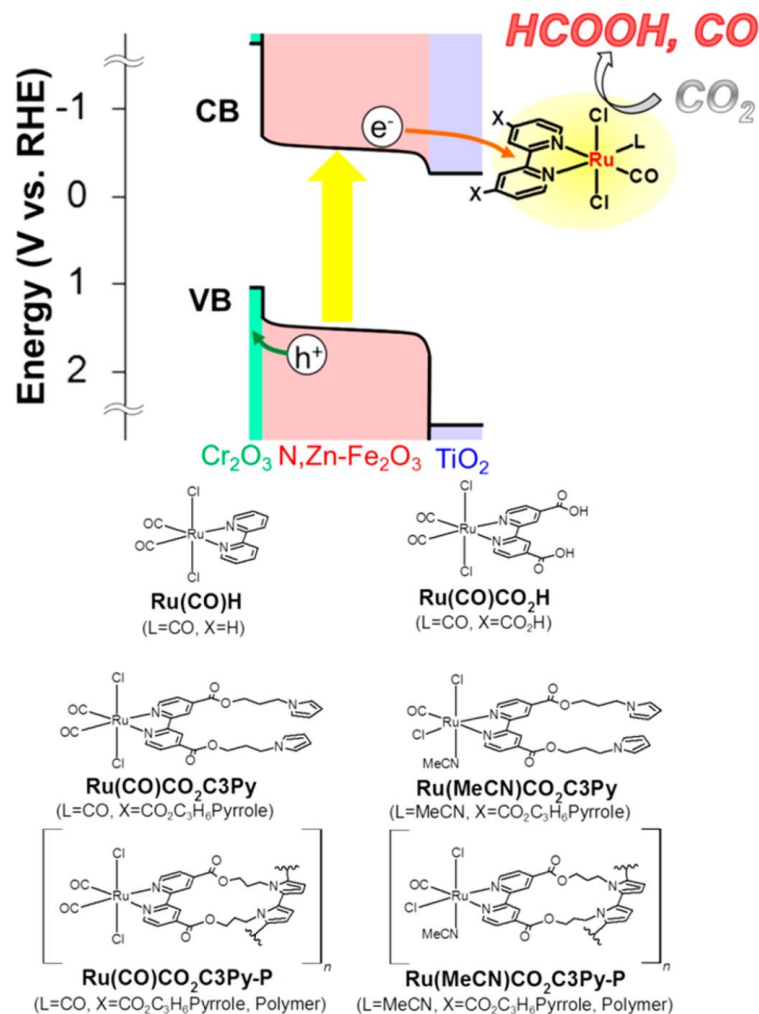


Figure 1.13 Scheme of CO₂ reduction over a Ru Complex/TiO₂/N,Zn-Fe₂O₃/Cr₂O₃

photocatalyst and the structures of the Ru Complexes used.[35]

Armstrong and co-workers developed a carbon monoxide dehydrogenase (CODH) from carboxydotherrmus hydrogenoformans as a biomolecular cocatalyst at a dye-sensitized p-NiO photocathode for PEC reduction of CO₂. This photoelectrode showed a good stability for 12 h under visible-light illumination with a photocurrent of 0.15 μAcm^{-2} , but only a small amount of CO was generated which could not be detected on GC (Figure 1.14).[36]

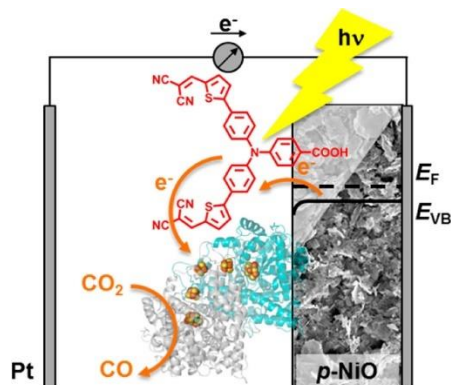


Figure 1.14 Schematic illustration of a dye-sensitized p-NiO photocathode with a CODH cocatalyst for selectively converting CO₂ to CO.[36]

1.2.4 Chalcogenide Semiconductors

Since CdTe has a band gap of 1.5 eV and a p-type form, this II–VI semiconductor has been widely studied for solar-driven CO₂ reduction. The combination of p-type CdTe and a metal phthalocyanine based on a first-row transition metal (V, Mn, Fe, Co, Ni, Cu, and Zn) has shown to be active for PEC CO₂-to-CO reduction in a nonaqueous environment. The best performance was achieved with a cobalt (II) derivative.[27]

Transition metal chalcogenides are also receiving a great deal of attention for PEC application, especially metal sulfides. Cabrera et al. conducted the first study using a chalcogenide. [3] A polycrystalline thin film of p-WSe₂, modified by electropolymerized films of [Re(CO)₃(v-bpy)Cl](v-bpy = 4-vinyl-4'-methyl-2,2'-bipyridine), was used to reduce CO₂ to CO at an onset potential of –0.65 V vs. SSCE in an 0.1 M TBAP/MeCN electrolyte. A turnover number of 450 could be obtained.

1.2.5 CO₂ Reduction on Multi-semiconductor Systems

In the long run, earth-abundant elements-based p-type semiconductors will be

preferable to materials made up of noble metals or high-quality Si. Accordingly, it appears that p-type Cu_2O is an attractive semiconductor with a bandgap of 2 eV and a negative CB edge. However, its inherent instability upon reduction conditions limits the use of Cu_2O for PEC applications. By atomic-layer-deposition (ALD) technique, a heterojunction device made of $\text{TiO}_2/\text{ZnO:Al}/\text{Cu}_2\text{O}$ layers was obtained and showed a good stability in a water-splitting PEC cell.[38] In this photocathode, the p-type Cu_2O layer acts as a light absorber and forms a p-n junction with the n-type ZnO:Al layer, while the top TiO_2 layer serves as a protective layer to keep the Cu_2O from photocorrosion.

This hetero-junctioned $\text{TiO}_2/\text{ZnO:Al}/\text{Cu}_2\text{O}$ device was also reported in reduction of CO_2 to CO under light illumination. In 2015, Grätzel and colleagues applied the $\text{Re}(\text{tBu-bpy})(\text{CO})_3\text{Cl}$ catalyst, introduced by Kubiak et al.,[39] and a TiO_2 -protected Cu_2O photocathode in PEC reduction of CO_2 (Figure 1.15).[40] According to the nature of the p-n junction devices,[41] the electron transfer from photocathode to the acceptor (e.g., a molecular catalyst) is dominated by the energy difference between the CB of TiO_2 and the reduction potential of the acceptor. Through the covalent bond linkages on the surface, the nanostructured photocathode allowed more immobilization of the $\text{Re}(\text{I})$ catalyst, leading to a higher photocurrent and a larger TON value.[42] Eventually, a high photovoltage of 560 mV was achieved, and a photocurrent density of 2.1 mA cm^{-2} for CO evolution was obtained with a FE of nearly 100%. A further observation was made that the transfer of electrons, from the surface of the photocathode to the Re-base molecular catalyst, was greatly limited, so protic electrolyte additives, such as

methanol and n-propanol, are required.

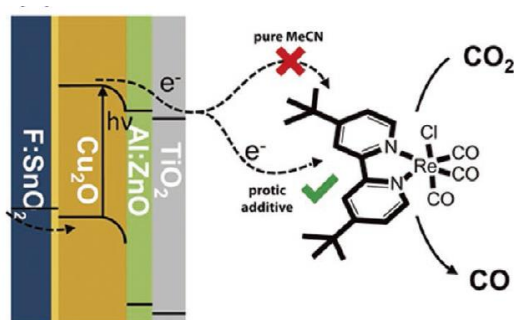


Figure 1.15 Scheme of the PEC CO₂ reduction involving TiO₂-protected Cu₂O photocathode and a Re-based molecular catalyst.[40]

In a subsequent study they immobilized the same Re-containing CO₂-reduction catalyst on the surface of another photocathode showed in Figure 1.16. For the purpose of promoting charge migration from the photocathode to the molecular cocatalyst, a nanostructured TiO₂ layer, which is obtained at low temperature, was deposited on the surface of the Cu₂O based photocathode. Then, the Re-based molecular cocatalyst was directly grafted on the TiO₂ layer through functionalized phosphonate groups. This approach greatly enhanced electrons transfer to the catalyst, leading to a 40-fold increase of the photocurrent compared to conventional planar devices. A large current densitie of 2.5 mA cm⁻² was obtained with high FE between 80% and 95% at 2.20 V vs Fc⁺/Fc in an 0.1 M Bu₄NPF₆/MeCN electrolyte. This improvement can be primarily attributed to the use of the nanostructured TiO₂ layer that is beneficial to transfer of electrons and essential to get large photocurrents.[43]

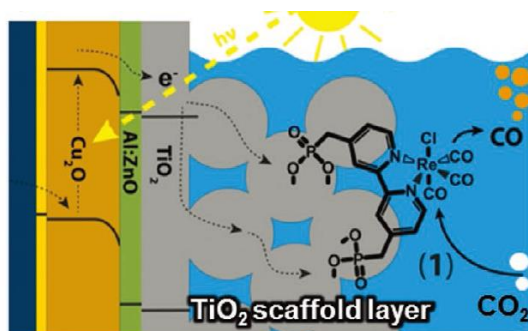


Figure 1.16 Scheme of TiO₂-protected Cu₂O photocathode with covalently bound Re(bpy)(CO)₃ to TiO₂ scaffold layer for CO₂ reduction to CO.[43]

1.4 Motivation and outline of this thesis

Despite the fact that PEC CO₂ reduction is at an early stage, it has the potential to utilize solar energy and convert CO₂ into chemical fuels. As shown in Table 1.2, noble metals catalysts, such as Au-based nanoparticles or alloys, remain the most extensively studied cocatalysts owing to their high activity and selectivity for CO. Besides, Ru and Re based molecular catalysts have also been widely studied. Apart from noble metals, few work has been devoted to non-noble catalyst. Cu-based materials are the most developed non-noble catalysts due to their high abundance and unique characteristics for hydrocarbon production. Using semiconductor materials as photoelectrodes combined with non-noble-metal-based molecular catalyst to achieve highly efficient and selective CO₂ reduction in water remains a high challenge. At part of my work, I intend to contribute to the design of more effective PEC systems for CO₂ reduction in aqueous solution with stable photoelectrodes and the use of non-noble metal complexes.

Table 1.2 Recent advances in semiconductor materials for PEC CO₂ reduction.

Entry	Photocathode	Catalyst	Solvent conditions	Illumination	Irrad. Time (h)	Bias potential (V vs. RHE)	Products	Performance	Ref.
1	p-Si	Nonporous Au film	0.2 M KHCO ₃	1 sun	1	-0.03	CO	FE of 91% for CO	[44]
2	p-Si photocathode	Particulate Ag film	0.5 M KHCO ₃	0.5 sun	1	-0.5	CO	FE > 90% for CO	[45]
3	p-Si nanowire arrays	Sn NPs	0.1 M KHCO ₃	AM 1.5G	3	-0.85	HCOOH	FE of 40% for HCOOH	[46]
4	B-doped p-Si	Fe porphyrin complex	MeCN/5% DMF (v/v)	90 mW cm ⁻² , 650 nm illumination	6	-1.11 V vs. SCE	CO	FE of over 80% for CO	[47]
5	p-GaN	Au NPs	0.05 m K ₂ CO ₃	> 495 nm illumination	50	-1.8	CO	Selectivity of 80% for CO	[48]
6	Zn-doped InP	Ru complex polymer	0.1 M NaHCO ₃ in water	SrTiO ₃ photoanode in AM 1.5G, > 400 nm illumination			HCOOH	Solar-to-chemical efficiency of 0.08% for HCOOH	[49]
7	p-GaP	Pyridine	0.1 M acetate buffer (pH 5.2)	6.5 mW cm ⁻² , 365 nm illumination	6–30	0.35	CH ₃ OH	FE of 96% for CH ₃ OH	[30]
8	TiO ₂ -protected n ⁺ p-Si nanowire	Au ₃ Cu NPs	0.1 M KHCO ₃	20 mW cm ⁻² , 740 nm illumination,	0.5	-0.2	CO	FE of 76.6% for CO	[50]
9	TiO ₂ -protected Cu ₂ O	Re(<i>t</i> Bubpy)(CO) ₃ Cl	7.5 M MeOH in MeCN	AM 1.5G	5	-1.73 V vs Fc ⁺ /Fc	CO	FE of ~100% for CO	[40]
10	TiO ₂ -protected InP nanopillars	Cu NPs	0.5 M KCl	532 nm illumination	12	-0.6 V vs. NHE	CH ₃ OH	FE of 8.7% for CH ₃ OH	[51]
11	ZnO/GaN/n ⁺ p-Si	Cu NPs	0.5 M KHCO ₃	300 W Xe lamp 800 mW cm ⁻²	100 min	-0.33	CO	FE of 20% for CO	[52]
12	Co ₃ O ₄ nanotube arrays	Cu NPs	0.1 M Na ₂ SO ₄	10 mW cm ⁻² , visible light	8	-0.3	HCOOH	6.75 mmol L ⁻¹ cm ⁻² for HCOOH	[53]
13	ZnO@ZnTe@CdTe nanorod	Au NPs	0.5 M KHCO ₃	simulated 1 sun illumination	3	-0.11	CO	FE of 74.86% for CO	[54]

Chapter 2 - Photocathode functionalized with a cobalt-based molecular catalyst for 2-electron CO₂ reduction in water

2.1 Structure and properties of Cu(In,Ga)Se₂ materials

Nowadays, semiconductor industry steps into the solar Photovoltaics (PV) market. PV materials convert light energy into electricity using semiconductor materials which exhibit photovoltaic effect. Since the 1950s, the development of crystalline silicon with p-n junction made much progress in the field of PV, and devices are no more restricted to silicon materials anymore. Various PV materials have come into the market, including organic semiconductors and each of them have advantages and drawbacks.

Solar PV devices are usually named according to the primary light-absorbing material. As shown in figure 2.1, PV devices are typically classified into two categories[55]: wafer-based and thin-film cells. Wafer-based cells are made up of semiconductor wafers and normally covered with glass for protection and mechanical stability, which could be handled with no additional substrate. While thin-film cells are fabricated with semiconductor films deposited onto a substrate such as glass, plastic, or metal. What's more, thin-films devices can further be sub-classified into commercial and emerging thin-film cells.

The commercial availability of PV devices has also made progress. Several of them get much attention: the crystalline or multi-crystalline silicon devices (c-Si) and

the thin-film based devices including the cadmium-telluride (CdTe) cells, amorphous silicon cells (a-Si) and polycrystalline chalcopyrite Cu(In,Ga)Se₂ cells (CIGS).

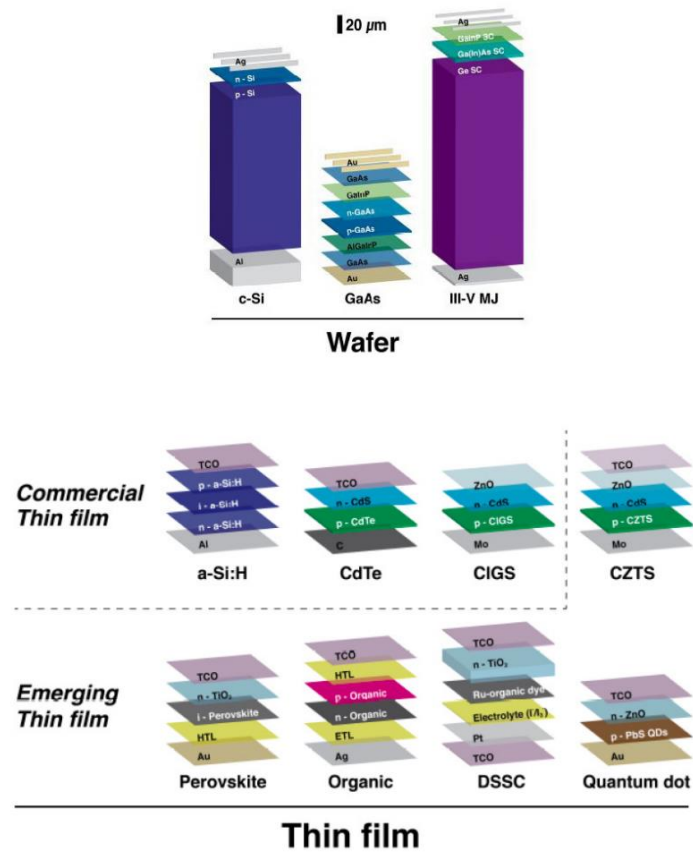


Figure 2.1 Typical solar PV device structures. Primary absorber layers are labeled in white.[55]

Research about photovoltaics has been dominated by crystalline silicon materials for a long time. The current needs for PV is directed towards highly efficient devices that produce solar electricity at a low price. CIGS devices are considered to be among the most promising thin-film devices. Firstly, CIGS thin-film devices are quite efficient.[56] The conversion efficiencies could reach up 22.6% for 0.5 cm² cells.[57] Besides, the cost of CIGS modules, calculated according to the levelized price of electricity, has further decreased due to the reduction of fabrication cost and up-scaling

of the production, making them more competitive. According to a survey from 2016, Solopower, Avancis, Hanergy, Solar Frontier, Stion, Silva Power, and Manz are among the major CIGS manufacturers. [58] In Figure 2.2, the market share of CIGS devices in the PV market is illustrated. In 2015, the thin-film modules represented ca. 7% on the whole production of PV devices and the CIGS production was accounting for nearly half of this percentage. There has been a rapid increase since 2010.

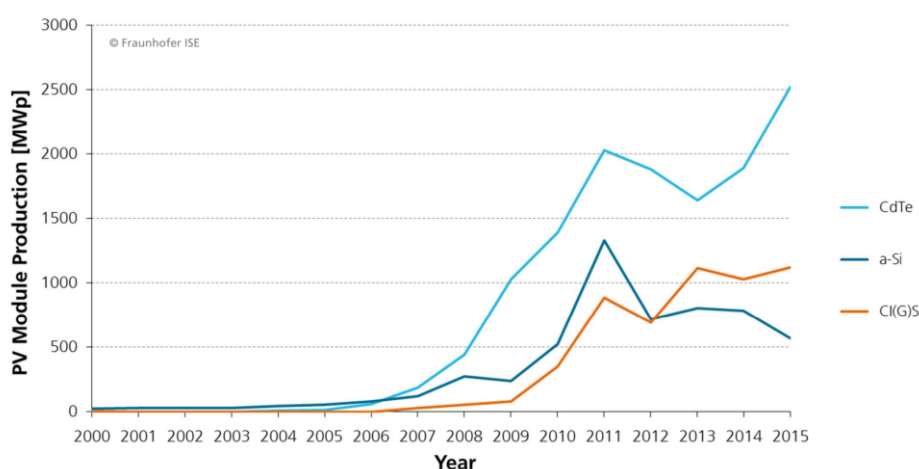


Figure 2.2 Annual Global PV Module Production [58]

CIGS is a multi-element semiconductor which can be deposited on flexible metal or polyimide substrates through various kinds of solution- and vapor-phase techniques [59] with a bandgap of 1.1–1.2 eV. CIGS is well studied for several applications including building-integrated and some other unconventional PV applications. It is widely used in solar cells due to the high radiation resistance. The commercial thin-film PV devices derived from active materials absorb light up to 1000 nm and are more efficient than silicon, enabling a thin film thickness of only a few microns. The use of few quantity of materials is a key advantage of these technologies. Advanced factories

can produce thin-film modules in a highly streamlined and automated fashion. What's more, it is suggested that thin-film technologies produce lower greenhouse gas emissions during production as compared to crystalline silicon (c-Si) PV.[60]

2.2.1. Structure of a standard CIGS solar cell

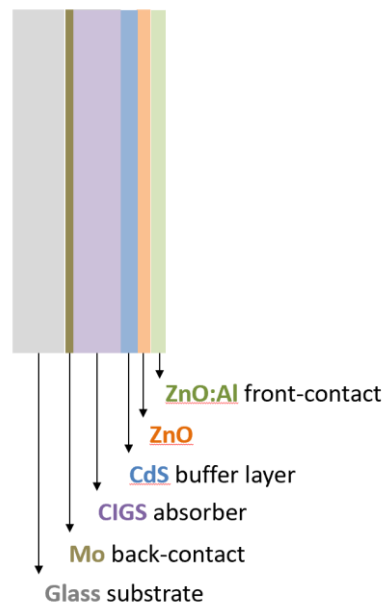


Figure 2.3 Scheme of a standard CIGS cell device

A standard CIGS solar device (as illustrated in Figure 2.3) is usually produced in various laboratories and industries. The cell is typically made up of a p-type CIGS layer acting as the main light absorber, in contact with a n-type CdS layer to form a p-n junction. At the frontside, a transparent electrode generally based on a ZnO/ZnO:Al bilayer collects the electrons. A molybdenum electrode is fabricated on the back side of CIGS to collect the holes. Notably, this structure is not fixed and could be adjusted to adapt specific issues or to reach high efficiencies. This configuration is named substrate configuration: under light irradiation, the light goes inside the cell from the top layer

(ZnO:Al). Each layer is described below, in terms of its role and details:

a. Substrate

The substrate is made of a soda-lime glass, which is used for the deposition of other layers. This substrate is especially well suited because of the following factors:

- its low cost;[61]
 - good stability under high temperature (glass transition temperature: 550-600°C). The fabrication temperature of the CIGS could be higher than 350°C. [62]. Generally, a high deposition temperature will result in a higher conversion efficiency.[62]
 - a thermal expansion of 9-9.5 ppm/K which matches with those of Mo and CIGS layers;
 - Na impurities. Hedström and coworkers have proved that Na can diffuse from the glass to the CIGS layer under a high temperature, which is of benefit to the CIGS [63].
- Additionally, one may note that recent research also found other good candidates, such as polyimide substrate,[59, 64] metallic substrate [65] and ultra-thin glass.[66]

b. Mo back-contact

The back-contact is made from a molybdenum layer because of the following factors:

- its high electron affinity (~4.5 eV). An interfacial thin layer of MoSe₂ will be formed under high temperature [67, 68] providing an ohmic contact with the CIGS;
- permeability and diffusion of Na element from the glass substrate to CIGS through channels among the Mo grains [69]. Na is also good for the deposition of MoSe₂ layer. [70, 71]

Other promising thin metal films to form the back-contact are also investigated, with W and Ta showing an efficiency similar to Mo. [72]

c. CIGS absorber

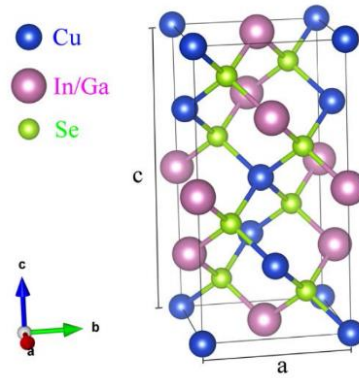


Figure 2.4 Unit cell of chalcopyrite for stoichiometric $\text{Cu}(\text{In,Ga})\text{Se}_2$. a and c are the lattice constants. The figure is reproduced from Ref. [73].

CIGS semiconductor is a solid solution made of the CuInSe_2 and CuGaSe_2 compounds. Cubic sphalerite structure is shown in Figure 2.4. The substitution of In by Ga can result in an expansion of the primitive cell: from CuInSe_2 to CuGaSe_2 , the lattice constants a and c change from 5.780 to 5.607 Å and from 11.604 to 10.983 Å, respectively [74]. The band-gap of CIGS varies with this structure variation, especially with the Ga content. From CuInSe_2 to CuGaSe_2 , the band-gap ranges from about 1.01 eV to 1.63 eV [75, 76]. The energy value of band-gap is given by the following equation:

$$E_g(\text{GGI}) = 1.01 + 0.626 \cdot \text{GGI} - 0.167 \cdot \text{GGI} \cdot (1 - \text{GGI})$$

$$\text{GGI} = [\text{Ga}] / ([\text{Ga}] + [\text{In}])$$

The fraction of Cu in CIGS is usually small ($[\text{Cu}] / ([\text{Ga}] + [\text{In}]) < 1$) [77, 78]. It is reported that the doping level is $5 \cdot 10^{15} - 5 \cdot 10^{16} \text{ cm}^{-3}$. In Cu-poor structures, there are plenty of defects in CIGS, which will enhance the recombination of charge carrier. So that the growth of Cu percentage would decrease the recombination [79].

Moderate Na concentration in the CIGS layer has proved to improve the

performance of the cells [63, 80, 81]. In small concentrations, Cu and In sites could be occupied by Na [82]. The effective hole density would be promoted, and the recombination would be decreased.

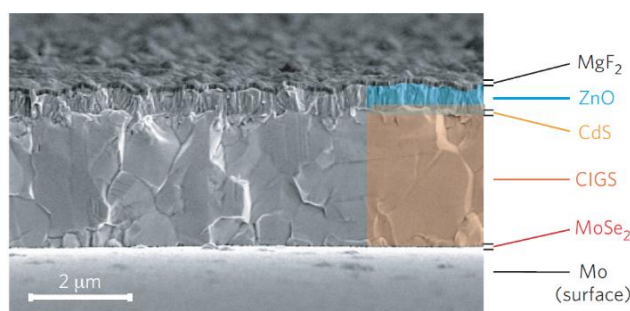


Figure 2.5 Cross sectional SEM image of a complete CIGS device.[83]

CIGS thin films usually have an average thickness of few micrometers with large grains. As shown in Figure 2.5, CIGS layers typically have many grain boundaries across their thickness, which appear to have a mild effect on the performance of the cells. [84] It was observed that the surface recombination velocity was low at the grain boundaries, as determined by electron-beam induced current (EBIC) and various other methods. [85] It has also been demonstrated that some composition variations such as a decreased Se vacancy, the presence of Na or Cu enrichment or oxygen enrichment will lead to a limitation of the recombination at the grain boundaries.[86]

There are several deposition techniques for the materials. The high temperature physical vapor deposition (PVD) of the metallic element is the most important and main deposition technique.[87] Other alternative methods include the sputtering of metallic precursors combined with annealing under the atmosphere of Se or S and high temperature;[88] alternatively, non-vacuum method including electro-deposition of

metallic or oxide precursors [89] has been developed.

d. CdS buffer layer

Chemical bath deposition is usually well adapted for the deposition of a CdS layer on the surface of the CIGS with a controlled composition. This CdS layer is an n-type semiconductor forming an p-n junction with the p-type CIGS layer. Upon the intermixing at the interface, the CdS layer helps passivating the CIGS surface, and protects the absorbing surface during sputtering.[78] For Cu-poor CIGS devices, a thin layer with Cu deficiency is formed at the CIGS/CdS interface, named ordered vacancy compound (OVC).[90] This thin layer could widen the band-gap near the interface. As a result of the valence energy band offset, holes are repelled and recombination at the CIGS/CdS interface is reduced. [78, 79] Likewise, the band-gap (2.4 eV) of the CdS is too low for use at the front-window, which result in optical losses. It should also be noted that CdS is a toxic compound, which may limit further use in devices. Other buffer layers including Zn(O,S) have been also investigated.[77]

e. ZnO/ZnO:Al front layer

Above the CdS layer, a thin layer of ZnO is deposited on the surface. Due to its intrinsic doping, this ZnO layer promotes electron conduction through the CB. [91] Aluminum doped zinc oxide (ZnO:Al) is generally deposited to form the front-contact layer by sputtering. Optimization of the ZnO:Al layer is important to balance its transparency and its conductivity in order to avoid resistive loss. In addition, materials including MgF₂ could be deposited on the top of the ZnO:Al to reduce the light reflection.

Overall, a high cell efficiency may be obtained by optimizing the substrate composition, CIGS deposition techniques and buffer/front-contact materials.

2.1.2 The Mo/CIGS/CdS/ZnO heterojunction

The structure of Mo/CIGS/CdS/ZnO/ZnO:Al heterojunction is a junction combined semiconductors with different band-gaps. Figure 2.6 shows the simulated band-diagram of a CIGS cell on SCAPS (a software invented by Prof. Burgelman et al. version 3.2.01 [92, 93]) according to the materials parameters utilized by Chirilă et al. [83]. As can be seen from his diagram, the VB and CB exhibit discontinuities as a result of variations in band-gap, electron affinities and doping concentration for each layer. At the CIGS/CdS interface, a negative VB offset and a positive CB offset are obtained. Recombination at the interface is thus reduced.

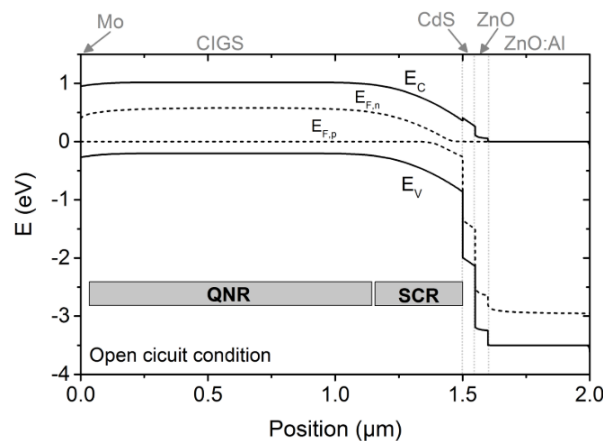


Figure 2.6 Band-diagram for the Mo/Cu(In_{0.7}Ga_{0.3})Se₂/CdS/ZnO/ZnO:Al junction simulated for open circuit condition under light irradiation. Simulation was conducted on SCAPS based on the materials parameters from ref. [41].

The CIGS layers is poorly p-doped ($4 \cdot 10^{15} \text{ cm}^{-3}$), and the CdS layer is highly n-

doped (10^{18} cm^{-3}). Charge diffusion at the CIGS/CdS interface results in positive charges in the n-part and negative charges in the p-part. According to the Poisson equation, an electric field is induced at the CIGS/CdS interface across a distance of ca. 300 nm due to the neutrality condition. This region lacks in free carriers, which is referred to as Space Charge Region (SCR). Free carrier density is close to the net doping density in the region extending from the SCR to the back contact layer, resulting in a neutral condition. This region is called the Quasi-Neutral Region (QNR).

2.2 Quaterpyridine complexes with CO₂ reduction

In the 1930s, Morgan and Burstall firstly isolated the tetradentate 2,2':6',2'':6'',2'''-quaterpyridine (qpy). [94] but the tedious synthetic process and the poor yield have greatly limited its development. However, much improved synthetic methods for qpy came up more recently, boosting the development of metal complexes with this ligand, notably for catalytic water splitting and CO₂ reduction. Due to its strongly chelating and good p-acceptor properties, qpy is expected to stabilize the reduced active species of metal complexes for the reduction of CO₂. Our group and colleagues from City University of Hong Kong also did a series of work on non-noble metal based qpy complex for CO₂ reduction.[95]

2.2.1 Quaterpyridine complexes for electrocatalytic reduction of CO₂

In 2016, our group and colleagues from Hong Kong investigated electrochemical reduction of CO₂ with $[\text{M}(\text{qpy})(\text{H}_2\text{O})_2]^{2+}$ (M = Co, Fe). [96] It was demonstrated that adding a weak Brønsted acid, such as phenol, could greatly enhance the performance

for electrocatalytic CO₂ reduction by [M(qpy)(H₂O)₂]²⁺ (M = Co, Fe), both in terms of efficiency and the overpotential. With the assistance of [Co(qpy)(H₂O)₂]²⁺ and the presence of 1 M phenol, the FE for CO are up to 94% with a selectivity of 99% at a potential of -1.4 V vs. SCE. The selectivity for CO reaches 100% with a smaller Faradaic efficiency of 37% in the case of [Fe(qpy)(H₂O)₂]²⁺. Besides, with a turnover frequency of up to 3.3 x 10⁴ s⁻¹ at a low overpotential of 0.3 V, [Co^{II}(qpy)(H₂O)₂]²⁺ was proved to be one of the most effective molecular catalysts.[97]

In aqueous solutions, qpy complex could also work efficiently. We appended Co(qpy)Cl₂ complexes on the surface of multi-walled carbon nanotubes (MWCNT) to form a heterogeneous catalyst (Co(qpy)Cl₂@MWCNT) for electrochemical reduction of CO₂ with high selectivity, rate and low overpotential. [98] Specifically, a selectivity of 100% for CO and a FE of 100% were obtained at very low catalyst loading (ca. 8.5 nmol cm⁻²) in water (pH = 7.3). The current density reached 0.94 mA cm⁻² with a low overpotential of 240 mV (at -0.35 V vs. RHE). At the overpotential of 340 mV, the current density was up to 9.3 mA cm⁻² with a good catalyst stability of 4.5 h and a TON of 89095. A current density for CO of 19.9 mA cm⁻² was obtained at 425 mV overpotential.

2.2.2 Quaterpyridine complexes for photocatalytic reduction of CO₂

In addition to their performance in electrochemical CO₂ reduction, quaterpyridine complexes have also shown impressive performance for photocatalytic reduction of CO₂. In 2016, our group reported that [M(qpy)(H₂O)₂]²⁺ (M = Co, Fe) complexes are

highly active catalysts for visible light driven photocatalytic reduction of CO₂ to CO. With Ru(bpy)₃²⁺ (bpy = 2,2'-bipyridine) worked as photosensitizer, 1,3-dimethyl-2-phenyl-2,3-dihydro-1H-benzo[d]imidazole (BIH) functioned as sacrificial reductant, and [Co(qpy)(H₂O)₂]²⁺ as catalyst, a TON_{CO} of 2660 as well as 98% selectivity for CO were obtained. Additionally, with [Fe(qpy)(H₂O)₂]²⁺ as catalyst, a TON_{CO} of 4300 and a selectivity of 95% were obtained. [96] Excellent results were also obtained with an organic dye as sensitizer.

In a following work, it was shown that [Fe(qpy)(H₂O)₂]²⁺ also showed good performance in photocatalytic reduction of CO₂ to CO combined with mesoporous graphitic carbon nitride (mpg-C₃N₄) as the photosensitizer with a selectivity of 97% for CO and a TON of 155 under visible light irradiation for 17 hours.[99]

Furthermore, coupling an excellent molecular catalyst with a solid sensitizer may yield a highly selective and very stable photocatalytic CO₂ reduction system. Recently, our group reported a novel molecular-hybrid material, Coqpy@mpg-C₃N₄, which is formed by attaching Coqpy-Ph-COOH to mpg-C₃N₄ through an amide linkage.[100] Under visible light irradiation, CO was generated with a selectivity of 98% and a TON of 128 in a acetonitrile solution, using BIH as sacrificial reductant and phenol as proton donor. This Coqpy@mpg-C₃N₄ material showed impressive stability during 4 days with no degradation.

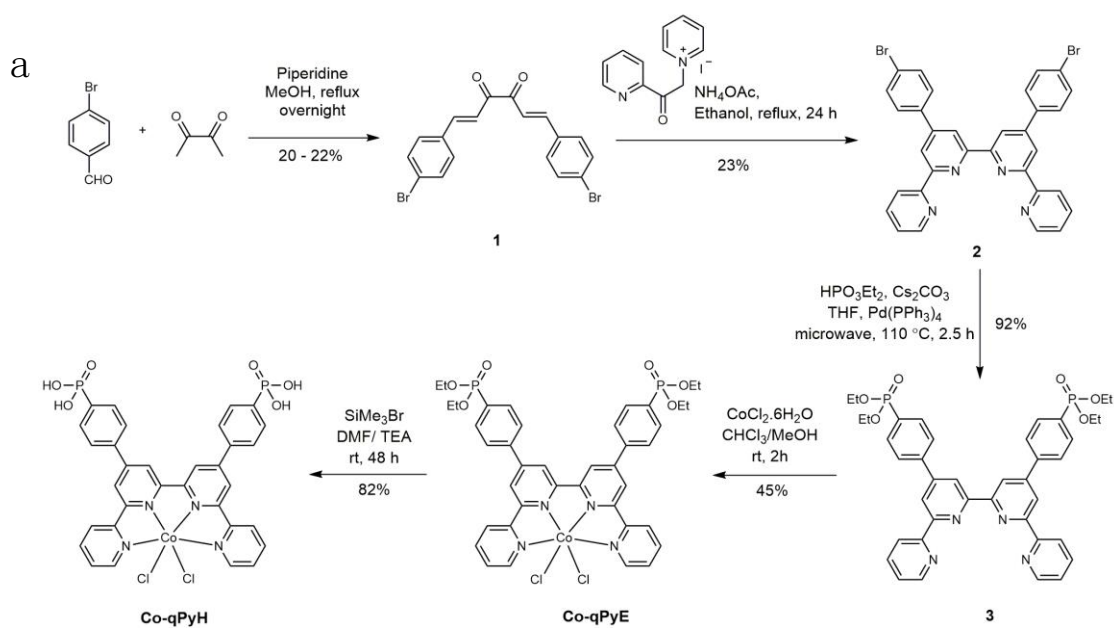
Coupling quaterpyridine complex with PV materials could be a promising way to reduce CO₂ under solar light, especially with a p-n junction material allowing for working near or under thermodynamic potential for CO₂-to-CO conversion, thanks to

the photopotential generated by the semiconductor material.

2.3 Functionalization of cobalt quaterpyridine

2.3.1 Cobalt quaterpyridine synthesis and functionalization

Cobalt quaterpyridine catalyst was modified with two phosphonic acid groups (**Co-qPyH**, Figure 2.7 a). It allows immobilization on metal oxide surfaces. It has been demonstrated that phosphonic acid is one of the most stable binding groups on the surface of metal oxide ($\text{pH} < 7$).^[101, 102] Co-qPyH used in this chapter was synthesized by the route in Figure 2 which is described in detail in Chapter 6 (Experiments and Methods) and was carefully characterized. The synthesis was achieved in Nantes in the group of Dr. Fabrice Odobel. Cyclic voltammetry (CV) of both Coqpy and Co-qPyH were recorded in 0.1 M KHCO_3 (Figure 2.7 b). The redox peaks have shifted to more negative position after modification.



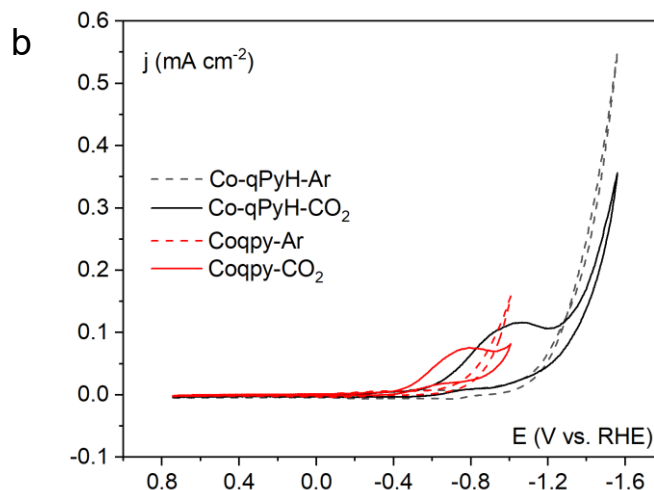


Figure 2.7 a. Synthetic route for Co-qPyH, **b.** CV in 0.1 M KHCO_3 , saturated with argon (dash) or CO_2 (solid). Scan rate was 100 mV s^{-1} .

2.3.2 Immobilization of modified cobalt quaterpyridine on TiO_2

Among all the semiconductors applied in photocatalysis, TiO_2 is the most common one which is widely used for dye bleaching, pollutant degradation and water purification. According to Fujishima, Honda et al., early studies have demonstrated that the catalyst can be used for the photocatalytic water splitting and CO_2 reduction under UV light irradiation. [103] A multitude of studies have been conducted on its crystal lattice, surface, charge transport, and other relevant properties due to its application in photochromic and electrochromic devices. Several factors explain the popularity of TiO_2 as a semiconductor, including its low cost, nontoxic property and abundance of reserves. [104] Corrosion of semiconductors can be induced by irradiation. Nonetheless, TiO_2 is not affected by this process in an aqueous environment because the oxidation of water is thermodynamically more favorable than forming oxygen molecules from oxide anions. As a result of this stability, TiO_2 is widely used in photocatalytic systems

over a wide pH range.[105] A majority of TiO_2 exists as four polymorphs (crystallographic phases): rutile (tetragonal), anatase (tetragonal), brookite (orthorhombic), and TiO_2 (B) (monoclinic). [104] The results of thermodynamic calculations showed that rutile is the most stable polymorph at all temperatures and pressures up to 6 kbar.

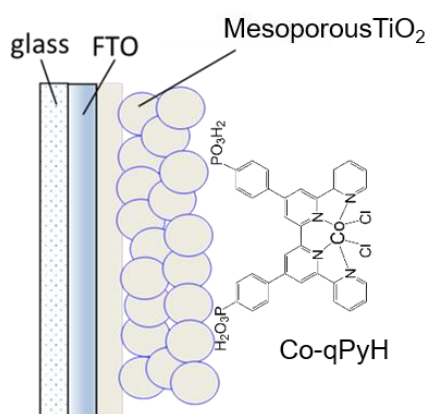


Figure 2.8 Structure of CoqPyH|m- TiO_2 layer at FTO electrode.

In this chapter, mesoporous TiO_2 layers were deposited on FTO-conductive glass substrates by a screen-printing method (described in Chapter 6), which is labeled as m- TiO_2 |FTO. Then Co-qPyH catalyst was immobilized on the surface of TiO_2 as shown in Figure 2.8. Careful detailed measurement was performed to investigate the immobilization of the catalyst. UV-vis absorption spectra were conducted on m- TiO_2 |FTO surface before and after immobilization of catalyst on TiO_2 layers (Figure 2.9), which confirmed that the semiconducting surface had been modified. Besides, only a small amount of absorbance was observed in the visible light region, making the it almost transparent to the majority of incoming light.

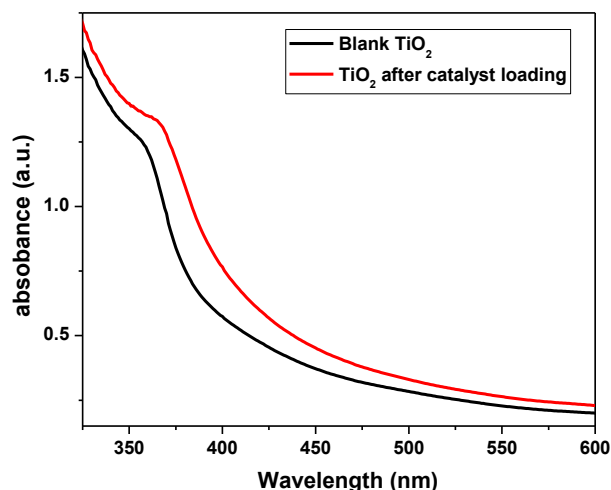


Figure 2.9 UV-Vis absorption spectrum of **Co-qPyH** grafted on **m-TiO₂** film.

Further analysis by attenuated total reflectance—infrared spectroscopy (ATR-IR) on Co-qPyH powder and Co-qPyH-loaded m-TiO₂ electrode (CoqPyH|m-TiO₂) were indicative of a successful immobilization of the catalyst on TiO₂ surface (Figure 2.10). The bands at ~ 1390 , ~ 1490 , ~ 1546 , and ~ 1601 cm^{-1} are attributed to aromatic ring stretching vibrations that indicate structural preservation of the catalyst upon immobilization. Meanwhile, the disappearance of a band near 893 cm^{-1} (P–OH) of Co-qPyH after immobilization along with the presence of the band at 1243 cm^{-1} (P=O stretching) prove typical bidentate binding of phosphonate on TiO₂ surface, with P=O functional group not involved in the linkage [50].

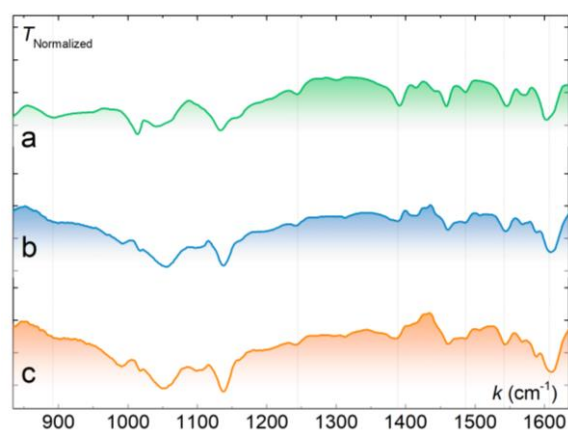


Figure 2.10 ATR-IR spectrum of Co-qPyH complex catalyst. From a powder **(a)**, deposited on **m-TiO₂** before **(b)** and after **(c)** 1h electrolysis performed in 0.1 M KHCO₃ electrolyte saturated with CO₂ (pH 6.8) at -0.56 V vs. RHE.

XPS analyses (Figure 2.11, blue) show a signal for P_{2p} which is typical of phosphate (132.5 eV) [51]. A N_{1s} signal of a pyridinic nitrogen refers to a cobalt atom in a quaterpyridine ligand (399.5 eV) [52]. In the spectrum of Co_{2p}, the main peak is at 780 eV, with a secondary peak at 796 eV, and two shoulders at 785 and 803 eV, respectively, confirming a Co²⁺ oxidation state and the presence of the catalyst as well.

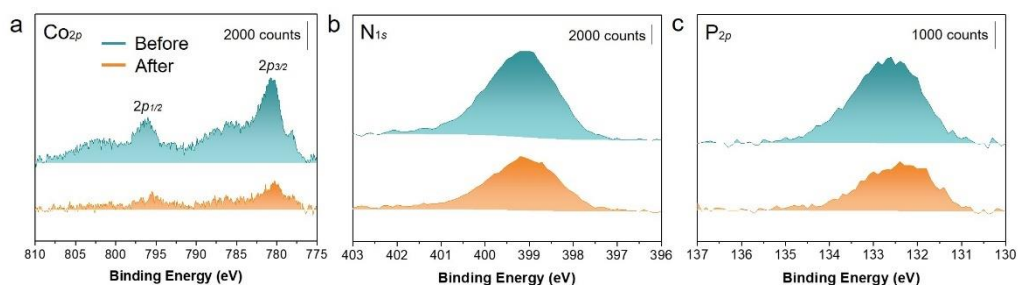


Figure 2.11 XPS analysis of Co-qPyH|m-TiO₂. Before (blue trace) and after (orange trace) 2 h electrolysis at -0.51 V vs. RHE in 0.1 M KHCO₃ electrolyte saturated with CO₂ (pH = 6.8). Data show binding energies for Co_{2p} **(a)**, N_{1s} **(b)** and P_{2p} **(c)**.

The EDX-mapping experiment (Figure 2.12) reveals homogeneous distribution of the catalyst across the surface of the electrode. In addition, mapping of Co element indicated that there was no aggregation of cobalt. The consistent atomic ratio of phosphate and cobalt is 2:1, confirming both the presence of the catalyst as well as its intactness after immobilization.

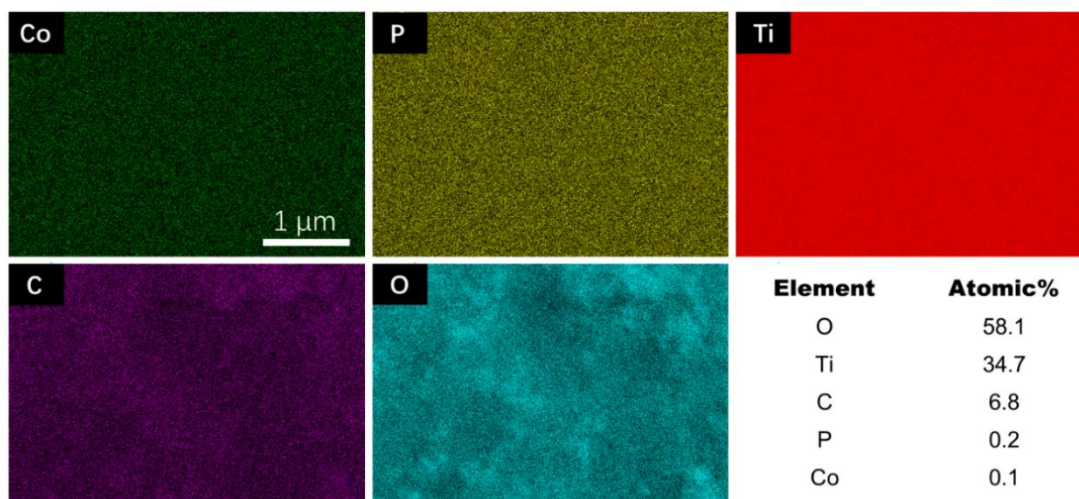


Figure 2.12 EDX-mapping images of a **Co-qPyH|m-TiO₂** electrode.

Additionally, inductively coupled plasma optical emission spectrometry (ICP–OES) measurements were conducted after a dissolution of catalyst in strong acidic (details in Chapter 5) indicating a catalyst loading of $29 \pm 4 \text{ nmol cm}^{-2}$ on m-TiO₂ film. Compared to previously reported data (85 nmol cm^{-2} for a Re complex on mesoporous TiO₂ [53]), this value is approximately one-third lower, suggesting that there is still potential to improve.

2.3.3 Electrochemical performance for CO₂ reduction

In order to test the catalytic performance of Co-qPyH|TiO₂ electrode, CV was first recorded in 0.1 M KHCO₃ water condition saturated with CO₂ (pH = 6.8). Catalytic current was observed as shown in Figure 2.13.

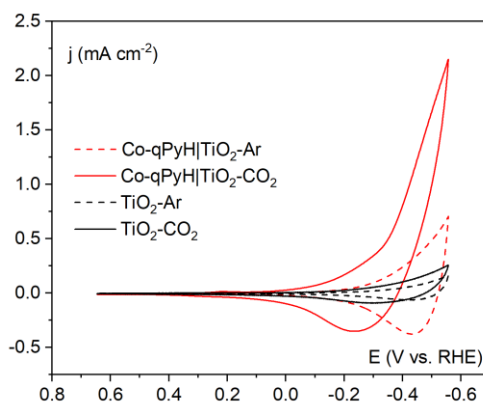


Figure 2.13 CV in EC conditions at a **Co-qPyH|TiO₂** (red) electrode and a bare **TiO₂** (black) electrode in 0.1 M KHCO₃, saturated with argon (dash) or CO₂ (solid). Scan rate was 20 mV s⁻¹.

A long-term electrolysis was performed at -0.51 V vs. RHE for 2 h, which showed an average catalytic current of 1.2 mA cm⁻² (Figure 2.14). The products were investigated through gas chromatography (GC) analysis indicating the production of CO with a selectivity of 80% and FE of 63%. The only by-product H₂ was also detected. Within the first 15 min, the current density had reached a steady-state. Over the next two hours, it remained stable with no significant changes. For comparison, a blank experiment is also performed in water with the same pH condition (0.1 M phosphate buffer) under argon at the same potential and did not yield any CO.

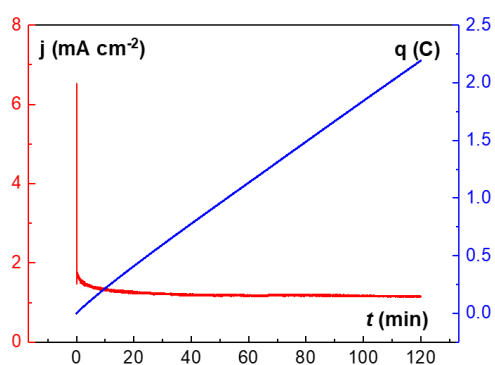


Figure 2.14 Long-term electrolysis in EC conditions at **Co-qPyH|m-TiO₂** electrode

polarized at -0.51 V vs. RHE in 0.1 M KHCO_3 electrolyte saturated with CO_2 (pH = 6.8).

The integrity of the catalyst before and after the electrolysis (1 h) in 0.1 M KHCO_3 saturated with CO_2 (pH 6.8) at -0.56 V vs. RHE was investigated by the ATR-IR analysis of the electrode (Fig. 2.10c), exhibiting nearly no changed characteristic signals. It indicated good stability of the catalyst and efficient immobilization.

XPS measurements of the electrodes were performed before and after a 2 h electrolysis in 0.1 M KHCO_3 saturated with CO_2 (pH 6.8) at -0.51 V vs. RHE (Figure 2.11). There was a slight decrease in signal intensity, which could be attributed to a slight desorption of the catalyst rather than decomposition of the catalyst. This is probably due to the pH value being very close to the upper limit of the stability of the phosphonate group[54].

According to the above results, the cobalt quaterpyridine complex kept its catalytical activity upon immobilization on a quasi-transparent $m\text{-TiO}_2$ electrode after functionalization with phosphonic acid. In our previous work (as introduced in Chapter 2.2.1), the $\text{Co}(\text{qpy})\text{Cl}_2$ catalyst was immobilized on carbon nanotubes in water (pH = 7.3) showing a larger current density up to 19.9 mA cm^{-2} [98]. Although the current density is lower here, but the TiO_2 inorganic layer offers the potential to be used as a support layer on photoelectrode surfaces for solar-driven reduction of CO_2 .

2.4 Photovoltaic-electrochemical performance of CIGS and functionalized TiO₂

CIGS for hydrogen evolution has been reported [56, 57], but they have not yet been used for CO₂ reduction, despite their attractive properties. Considering the good performances of Co-qPyH|m-TiO₂ electrode in EC conditions as described in Chapter 2.3, we then thought about combining this material as a top layer with CIGS as the photocathode to reduce CO₂ under light irradiation.

2.4.1 Photocathode assembly and characterizations

We prepared a CIGS component with a p-n junction made up of a p-type CIGS layer and a n-type CdS layer, and further layers of ZnO and ZnO:Al (AZO) were used to protect the material (see details in Chapter 6). The structure of the CIGS used in this chapter is shown in Figure 2.15 (composition is Cu In_{0.1}Ga_{0.9}Se₂).

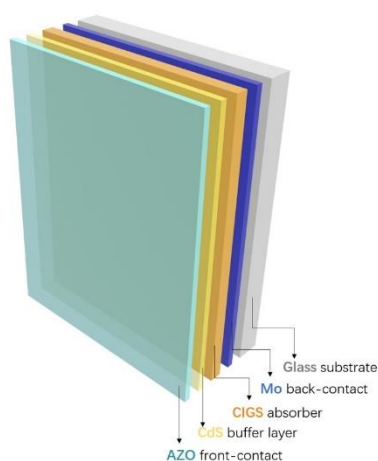


Figure 2.15 Schematic view of the CIGS based layered material used in photoelectrochemical conditions

A scanning electron microscopy image revealed the structure of the different layers of the electrode (Figure 2.16). The thickness of Mo back-contact layer is around 500 nm. The CIGS and CdS layers are around 2 μm and 40 nm, respectively. In addition, the CIGS based solar cell exhibits a short-circuit photocurrent density (J_{sc}) of 18 mA cm^{-2} (calculated from the external quantum efficiency, EQE), and an open circuit voltage (V_{OC}) ranging between 700 and 750 mV from one cell to another. The fill factor (FF) ranges between 60 and 70 % resulting in a power conversion efficiency of about 9 % under AM 1.5 (1000 W/m^2).

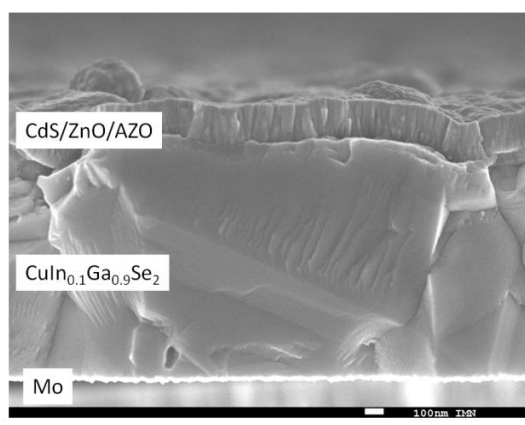


Figure 2.16 Scanning electron microscope (SEM) cross section image of the CIGS layer.

To combine the Co-qPyH catalyst and CIGS devices, we firstly devised a strategy (as illustrated in Figure 2), which coupling an external CIGS PV cell (ZnO:Al|ZnO|CdS|CIGS|Mo material) with the above Co-qPyH|m-TiO₂ electrode (Figure 2.17). The coupling of a PV cell to an electrolyzer (PV-EC) is a practical method of utilizing the photogenerated charges in the cell devices and activating a substrate in solution. The photoactive material in this configuration is not in directly in contact with the electrolyte solution, which partially addresses the stability issue.

2.4.2 PV-EC system for CO₂ reduction

In order to measure the photocurrent, a linear scan voltammetry (LSV) was recorded in 0.1 M KHCO₃ electrolyte saturated with CO₂ (pH 6.8) with the Co-qPyH|m-TiO₂ electrode connected to a CIGS solar cell (ZnO:Al/ZnO/CdS/CIGS/Mo). Photocurrent was observed, up to approximately 2 mAcm⁻².

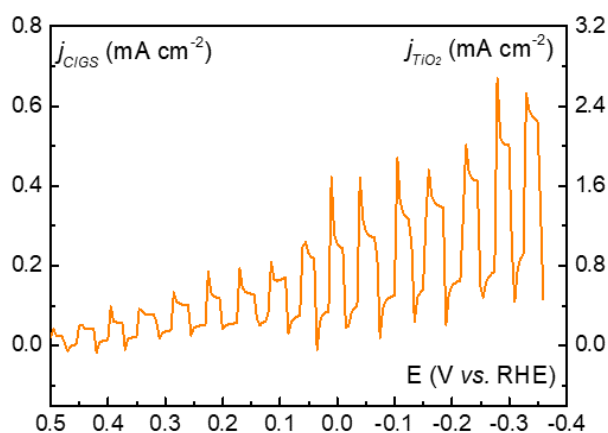


Figure 2.19 LSV in PV-EC conditions at **Co-qPyH|m-TiO₂** electrode in a 0.1 M KHCO₃ electrolyte saturated with CO₂ (pH 6.8) and connected to an external CIGS solar cell under chopped light illumination. Scan rate was 5 mV s⁻¹.

Electrolysis experiments were performed in 0.1 M KHCO₃ saturated with CO₂ (at pH 6.8) at 0.14 V vs. RHE for 2 h with an average current density of ca. 1 mA cm⁻² (per geometric surface of TiO₂). Another electrolysis was conducted at -0.06 V vs. RHE in the same electrolyte conditions. An average current density of 3.25 mA cm⁻² (per geometric surface of TiO₂) was obtained (Figure 2.20). Analysis by GC indicates the main product is CO with a selectivity of 87% at a bias potential of -0.06 vs. RHE, corresponding to a potential more negative than the thermodynamic potential (overpotential formally negative $\eta = -50$ mV).

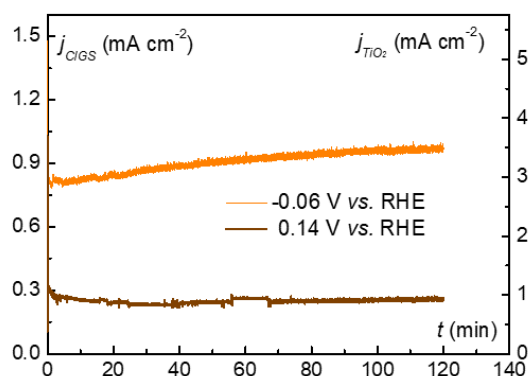


Figure 2.20 Electrolysis in PV-EC conditions on **Co-qPyH|m-TiO₂** electrode in a 0.1 M KHCO₃ electrolyte saturated with CO₂ (pH 6.8), and connected to an external CIGS solar cell under light illumination, polarized at +0.14 (brown) and -0.06 (orange) V vs. RHE.

A longer-term, 7 h electrolysis was then carried out in a 0.5 M KHCO₃ electrolyte with continuous CO₂ flow (pH 7.2) at a potential of -0.03 V vs. RHE corresponding to an overpotential formally negative ($\eta = -80$ mV) for CO₂ to CO reaction (Figure 2.21). An average current density of 1.78 mA cm⁻² was observed and the selectivity for CO production was maintained between 82 and 85% over the course of the experiment.

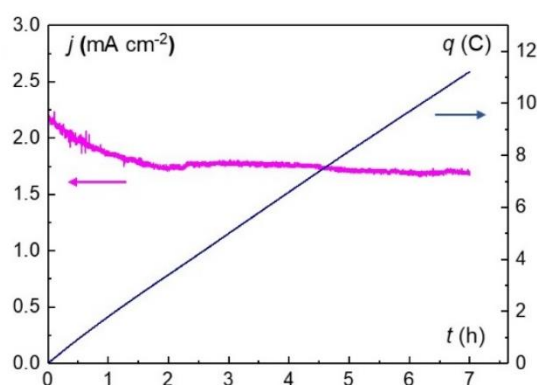


Figure 2.21 Long term electrolysis in PV-EC conditions at a **Co-qPyH|m-TiO₂** electrode in 0.5 M KHCO₃ saturated with CO₂ (pH 7.2), connected to an external irradiated CIGS solar cells polarized at -0.03 V vs. RHE, with continuous flow of CO₂

during electrolysis.

2.5 Photo-electrochemical performance of CIGS with Cobalt Quaterpyridine

2.5.1 Photocathode assembly and characterizations

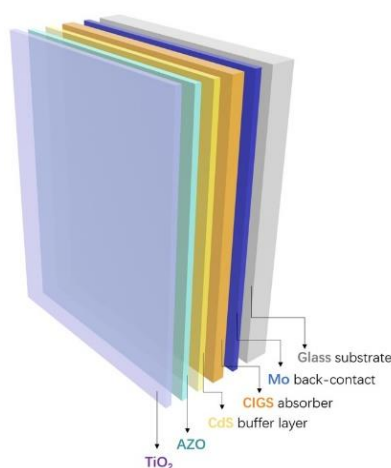


Figure 2.22 Structure of the CIGS based material employed in PEC conditions.

In this second approach, we grafted the catalyst directly on the CIGS-based photocathode so as to reduce CO₂ in a fully integrated PEC process. Specifically, a TiO₂ layer was directly deposited on top of the complete CIGS (ZnO:Al/ZnO/CdS/CIGS/Mo) device and further grafted with Co-qPyH catalyst (Figure 2.22). Notably, the dense layer of TiO₂ (f-TiO₂) deposited by sputtering method (see details in Chapter 5) has a thickness of 5~10 nm, and the catalyst was loaded by chemisorption in the same method as before for m-TiO₂ film (Co-qPyH|f-TiO₂|CIGS) as described in Chapter 2.3. In comparison with m-TiO₂ film, a lower catalyst loading of 3 ± 1 nmol/cm² was measured by ICP-OES, corresponding to a 10-fold decrease.

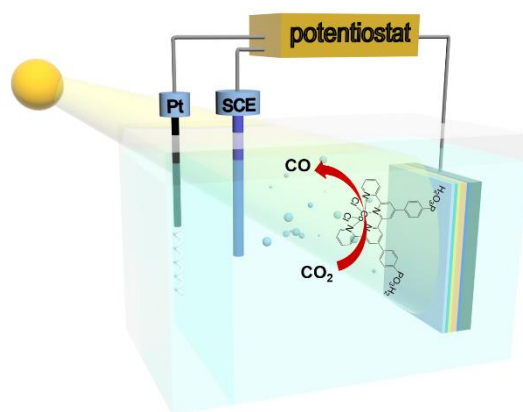


Figure 2.23 Illustrative scheme of the PEC systems investigated in this study.

2.5.2 Photo-assisted CO₂ reduction performance

Linear sweep voltammetry was conducted under chopped illumination in 0.1 M KHCO₃ aqueous solution (Figure 2.24, red), showing a photo response with an onset potential of 0.2 V vs. RHE. Additionally, a blank experiment was also made under Ar and the same pH conditions exhibiting negligible photocurrent modulation (Figure 2.23, black).

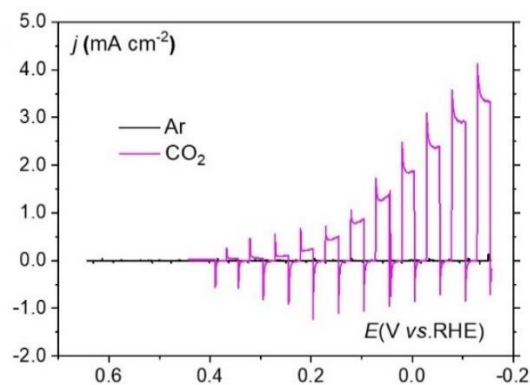


Figure 2.24 LSV in PEC conditions at a **Co-qPyH|f-TiO₂|CIGS** electrode in 0.1 M phosphate buffer saturated with argon (pH 6.8, black) or 0.1 M KHCO₃ electrolyte saturated with CO₂ (pH 6.8, purple) under chopped light. Scan rate was 5 mV s⁻¹.

The stability of the photoelectrode was assessed through a long-term

photoelectrocatalysis experiment performed in a 0.1 M KHCO_3 electrolyte saturated with CO_2 (pH 6.8) at a bias potential of -0.06 V vs. RHE. The average current density was 0.8 mA cm^{-2} with only a slight decay over the course of 2 h (Figure 2.25). The products were analyzed by GC, which shows a selectivity of 97% for CO and 3% for the only by-product H_2 . The slight drop in photocurrent density over the course of the photoelectrolysis is probably due to catalyst leaching from the electrode. Another possible reason might be the instability of the constituent layers, especially when the AZO layer comes into contact with water. However, with this configuration, it is possible to achieve a high selectivity for CO generation for several hours. A turnover number for CO more than 8000 was obtained corresponding to a mean turnover frequency (TOF) of 1.1 s^{-1} . It is worth mentioning that these TON and TOF values are underestimated based on the total surface concentration of the catalyst, rather than its electroactive fraction. Meanwhile, a blank experiment was performed without the catalyst grafted onto TiO_2 leading to a low current density and no CO production upon GC measurement.

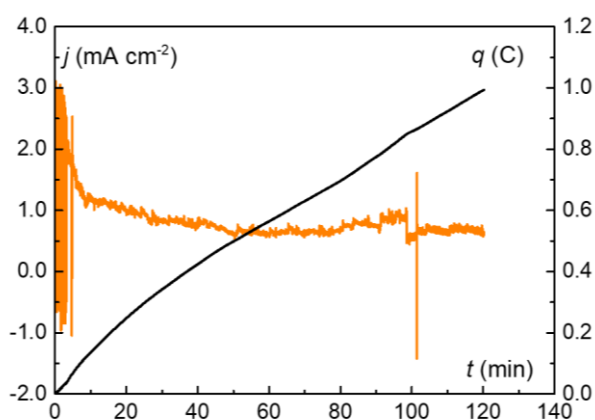


Figure 2.25 Electrolysis in PEC conditions at $\text{Co-qPyHf-TiO}_2/\text{CIGS}$ electrode in a 0.1 M KHCO_3 electrolyte saturated with CO_2 (pH 6.8), under light illumination,

polarized at -0.06 V vs. RHE.

A labeled experiment under $^{13}\text{CO}_2$ atmosphere is compulsory to conclude on the origin of the product of CO. Electrolysis experiment was repeated with $^{13}\text{CO}_2$. The products were analyzed via GC/MS. In the meantime, the result was compared with that under $^{12}\text{CO}_2$ forcefully confirming that CO originated from CO_2 (Figure 2.26).

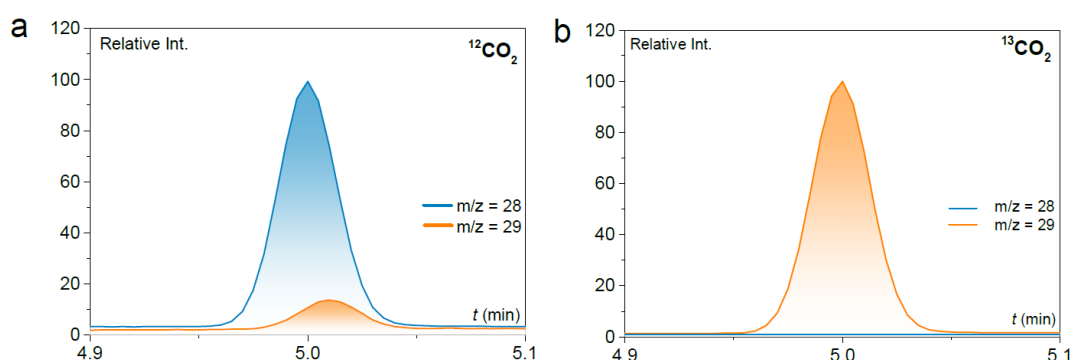


Figure 2.26 GC/MS chromatograms at the retention time of carbon monoxide. Specific traces of $m/z = 28$ value (blue) and $m/z = 29$ value (orange) after 2h electrolysis at illuminated **Co-qPyH|f-TiO₂|CIGS** ($E_{\text{bias}} = -0.06$ V vs. RHE), in 0.1 M KHCO_3 electrolyte saturated with $^{12}\text{CO}_2$ (a) and $^{13}\text{CO}_2$ (b).

2.6 Conclusions and perspectives

In this chapter, we successfully demonstrated the application of CIGS photocathode for solar-driven CO_2 catalytic reduction. For coupling with CIGS, cobalt quaterpyridine molecular catalyst was functionalized and homogeneously immobilized on a TiO_2 upper layer without structural damage and loss of activity confirmed by a series of complementary measurements. Our step-by-step strategy from PV-EC configuration eventually to PEC configuration was proposed to combine CIGS with Co-qPyH, and good activity, selectivity and negative overpotential were obtained under

visible-light irradiation in neutral water condition. It is worth mentioning that this study led to the development of the first PEC device with high photoelectrocatalytic activity in aqueous solution and a 97% of selectivity for CO. In contrast to other previously reported PEC CO₂ reduction systems, including those with noble metals (see entries 1, 5, and 6 in Table 2), our work shows pioneering performance. For instance, with a Ru catalyst grafted onto a hematite photocathode [35], a maximum photocurrent density for CO of 45 $\mu\text{A cm}^{-2}$ was obtained at 110 mV overpotential, which is approximately one order of magnitude less than that of the Co-qPyH|f-TiO₂|CIGS photocathode.

In this study, we present the first report of CIGS semiconductor as a component of photocathode with molecular catalyst for CO₂ reduction in aqueous medium. It will open up the possibility of better-performing photocathode for PEC reduction of CO₂. A higher catalyst loading would further contribute to the enhancement of this system by using a strategy such as nano-structuration of the upper layer. A fully unassisted solar-driven fuel production system could be achieved when coupled with an appropriate photoanodic reaction.

Table 2.1 A summarizing table of all the electrolysis in this chapter:

System	Electrolyte	t (h)	E_{applied} (V vs. RHE)	$j_{\text{total, TiO}_2}$ (mA cm ⁻²)	η_{CO} (mV)	CO		H ₂
						FE [Select.] (%)	T ON ^c	FE [Select.] (%)
EC	0.1 M KHCO ₃ CO ₂ sat. (pH = 6.8)	2	-0.51	1.22	400	63 [80]	10 02	16 [20]
	0.1 M KH ₂ PO ₄ /K ₂ HPO ₄ Ar sat. (pH = 6.8)	2	-0.51	3.00	NA	0 [0]	N A	86 [100]
PV-EC	0.1 M KHCO ₃ CO ₂ sat. (pH = 6.8)	2	0.14	0.90	- 250	80 [80]	94 1	20 [20]
	0.1 M KHCO ₃ CO ₂ sat. (pH = 6.8)	2	-0.06	3.26	-50	96 [87]	40 60	14 [13]
	^a 0.5 M KHCO ₃ CO ₂ sat. (pH = 7.2)	7	-0.03	1.78	-80	NR [82]	N R	NR [18]
PE C	0.1 M KHCO ₃ CO ₂ sat. (pH = 6.8)	2	-0.06	0.81	-50	89 [97]	80 31	3 [3]
	^b 0.1 M KHCO ₃ CO ₂ sat. (pH = 6.8)	2	-0.06	0.05	-50	0 [0]	N A	31 [100]

^a Under continuous gas flow. ^b No catalyst. ^c Lowest estimation (see Methods).
NA: Not applicable. NR: Not reported (experiments under gas flow).

Table 2.2 Summary of the most efficient molecular photocathodes for CO₂ reduction reported in the literature.

Entry	Light absorbing electrode	Catalyst	E _{Applied}	j _{total} (mA cm ⁻²) @ E _{Applied}	j _{CO} (mA cm ⁻²) @ E _{Applied}	FE total (%) @E _{Applied}	FE _{CO} (%)@ E _{Applied}	Selectivity for CO@ E _{Applied}	Electrolyte	Illumination	Ref.
1	Fe ₂ O ₃ co-doped with N and Zn TiO ₂	Ru(MeCN)CO ₂ C 3Py-p	0.1 V vs. RHE	0.15	0.045	100 13h	30 13h	30 13h	0.1 M KHCO ₃ (aq.)	100 mW cm ⁻² , AM1.5G	[35]
2	Cu ₂ O TiO ₂	ReCl(bpy)(CO) ₃	-2.05 V vs. Fc ⁺ /Fc	2.5 * @-2.0 V vs.Fc ⁺ /Fc	≈2~2.4 @-2.0 V vs.Fc ⁺ /Fc	NR	NR	80~95 1.5h	0.1 M TBAPF ₆ , MeCN	100 mW cm ⁻² , AM1.5G	[43]
3	SiNWs-H	MnBr(bpy)(CO) ₃	-1.10 V vs. SCE	≈1.00 * @-1.2 V vs. SCE	≈1.00 @-1.2 V vs. SCE	NR	NR	100 3h	CH ₃ CN + 0.1 M Bu ₄ NClO ₄ under CO ₂ + 5% v/v H ₂ O	Hg-Xe lamp, 525 nm < λ < 655 nm	[29]
4	NiO Zn-porphyrin	ReCl(bpy)(CO) ₃	NR	0.020 (mA)	NR	NR	6.2 115h	NR	0.1 M TBAPF ₆ , DMF	Xe lamp, λ = 430 nm	[106]
5	NiO	Ru(II)-Re(I) dyad	-0.11 V vs. RHE	≈ 0.005	≈0.0045	64% 12h	58	91 12h	0.05 M NaHCO ₃ (aq.)	Xe lamp, λ = 460 nm	[107]
6	CuGaO ₂	Ru(II)-Re(I) dyad	0.29 V vs. RHE	0.011 * 0.0 V vs.RHE	≈0.007 0.0 V vs.RHE	81 15h	49 15h	61 15h	0.05 M NaHCO ₃ (aq.)	Xe lamp, λ = 460 nm	[108]
7	Si TiO ₂	Co(II) bis-terpyridine	0.0 V vs. RHE	0.18	0.029	63 8h	9.5 8h	15 8h	0.1 M KHCO ₃ (aq.)	100 mW cm ⁻² , AM1.5G	[109]
			-1.0 V vs. Fc ⁺ /Fc	0.25	0.13	77 24h	41 24h	53 24h	0.1 M TBABF ₄ , 6:4(v:v) MeCN:H ₂ O		

8	Si n-GaN	Ru/Ct	-0.25 V vs. RHE	≈1.1	≈0.7 (j _{formate})	69 20h	64 for formate 20h	93 for formate 20h	0.05 M NaHCO ₃ (aq.)	100 mW cm ⁻² , AM1.5G	[110]
PV-EC system	CIGS	Co(II) quaterpyridine CoqPyH	-0.06 V vs. RHE	0.9	0.78	110 2h	96 2h	87 2h	0.1 M KHCO ₃ (aq.)	Xe lamp, λ > 435 nm	This work
			-0.033 V vs. RHE	1.78	1.50	NR	NR	82 7h	0.5 M KHCO ₃ (aq.)		
PEC system			-0.06 V vs. RHE	0.81	0.72	92 2h	89 2h	97 2h	0.1 M KHCO ₃ (aq.)		

Chapter 3 - Photo-assisted CO₂ reduction to methanol on a porous carbon-cobalt molecular catalyst electrode with the assistance of CIGS photovoltaic material

3.1 CO₂ reduction to methanol

Electrochemical and photochemical conversion of CO₂ into liquid fuels is one of the most difficult and important chemical challenge. Although CO and formate could be interesting molecules, further reduced products, such as methanol, are particularly appealing. Methanol is an excellent energy carrier because of its high volume-specific energy density and it is an intermediate for many bulk chemicals. From CO₂ to CH₃OH, it is a six-electron six-proton catalytic reduction process. Efforts have been devoted to the investigation of various catalysts such as metal oxides, metal alloys, or chalcogenide-based materials.[111-113] Most of these work either focus on rare metals, or report low selectivity for methanol with the formation of co-generated products including methane or C₂ molecules.[114, 115] In addition, Mul et. coworkers reported that the thermodynamic stability window of metal oxides is limited [116] while reduced metal electrodes lead to a lower activity for CH₃OH generation. Consequently, molecular catalysts could be an interesting alternative to achieve high selectivity thanks to the control of the active site structure, as previously done in our group for the CO₂-to-CO reduction process. [117, 118] There are still few examples of molecular catalyst driving the CO₂ reduction up CH₃OH. Some transition-metal complexes with the help

of heterogeneous co-catalyst showed some methanol evolution. [119-121] Besides, a few papers reported methanol as CO₂ reduction product using molecular catalysts, but the exact source of the alcohol was not identified. [122] As described in Chapter 1.2.2 (Figure 1.11) [31], pyridine complex was used in a PEC CO₂ reduction process and showed trace of methanol. Nevertheless, no evidence proved that the generated methanol was issued from CO₂. In contrast, our previous work reported demonstrated for the first time that cobalt phthalocyanine (CoPc) is able to electroreduce CO₂ into CH₃OH in aqueous media through a CO intermediate. [123] Since the CO₂-to-CO step is very efficient at a neutral pH, a good strategy would be to combine an optimized CO₂-to-CO step in a first electrolyzer with the following step of CO reduction to methanol in a second electrolyze. In basic media (pH 12–13), pure CO was used as a substrate and the Faradaic efficiency (FE) towards methanol generation up to 14.3% was detected. an overall FE from CO₂ to CH₃OH of 19.5% may be achieved.

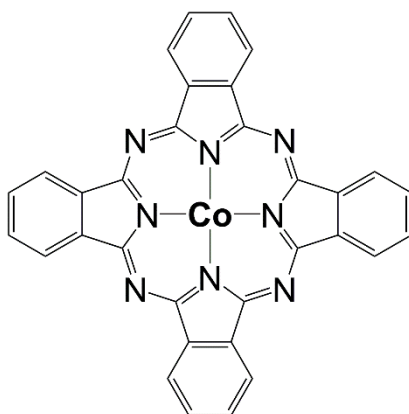


Figure 3.1 Structure of cobalt phthalocyanine (CoPc), a molecular electrocatalyst for CO₂-to-CH₃OH reduction in aqueous solution.

3.2 Cobalt phthalocyanine complexes

Phthalocyanine (Pc) are a well-known family of catalysts which is industrially used as dyes for painting[124] and are thus particularly appealing as easily accessible compounds. Among them, CoPc has been extensively studied in electrochemistry, [17, 18] and used as a dye at a large scale in the painting industry due to its low cost. An early study of Lieber *et al.* demonstrated the reduction of generation of CO₂ to CO on a carbon electrode modified by absorbed CoPc at an applied potential of -1.15 V *vs.* SSCE (silver-silver chloride electrode) in an aqueous solution (pH = 5), with a turnover number (TON) of 3.7×10^5 . [125] The faradaic efficiency (FE) of CO was 55 ~ 60% with H₂, oxalate and formate as by-products. It is notable that this study showed a good stability attributed to immobilized CoPc on the electrode compared with the homogeneous case. Choi *et al.* [126] developed a sterically hindered CoPc that led to electrochemical CO₂-to-CO competition with up to 85% FE in aqueous solution (pH 6.8), at a potential of -0.79 V *vs.* RHE. In this study, CoPc π -stacked onto chemically converted graphene which was deposited on a carbon paper electrode. In a recent study,[127] Reisner *et al.* reported the CO₂-to-CO conversion on a hybrid electrode composed of a CoPc complex bearing four phosphonic acid anchoring groups immobilized on mesoporous TiO₂. Our previous work reported that cobalt phthalocyanine was used as a catalyst for the electrochemical conversion of CO₂ to methanol in aqueous electrolytes at ambient conditions of temperature and pressure. [123] We set a simple procedure for preparing the catalytic electrode, and the low loading amounts of the catalyst (a few nmol cm⁻²) make the process versatile and easy

to implement. It allowed to identify formaldehyde as a key intermediate and pH effect on selectivity. This can help for establishing a sequential process where CO₂ is first converted to CO, which would be further used as a reactant to produce methanol. 14.3% methanol (FE) was generated at -0.64 V vs. RHE in aqueous solution (pH = 13) with pure CO as substrate. This study opens up possibilities for developing earth-abundant metal-based molecular complexes as electrocatalysts for CO₂ reduction to liquid fuel in water.

3.3 Photo-assisted reduction of CO₂ to methanol

Considering the excellent performance of the CIGS-based semiconductors in PEC reduction of CO₂-to-CO (as described in Chapter 2) and the good capacity of CoPc for CO₂ reduction to methanol (as introduced in Chapter 3.1), it would be an interesting strategy to drive CO₂ reduction to methanol under solar light through combining a CIGS-based PV material with CoPc complex as catalyst.

Thus, we decided to combine photovoltaics and electrochemistry in PV-EC configuration. Specifically, we coupled the light conversion and the chemical process by using a CIGS-based PV device generating electrons and an EC cell employing these electrons to carry on the electrochemical reactions. This approach has two advantages. Firstly, both PV and EC parts could benefit from optimization independently concerning their separated requirements. Secondly, the normally encountered photodegradation of PV devices in contact with an electrolyte is bypassed. Therefore, a PV-EC coupling cell (Figure 3.2) is also an interesting approach to utilize solar

generated electrons to sustainably activate and convert CO₂ in aqueous solutions.[128, 129]

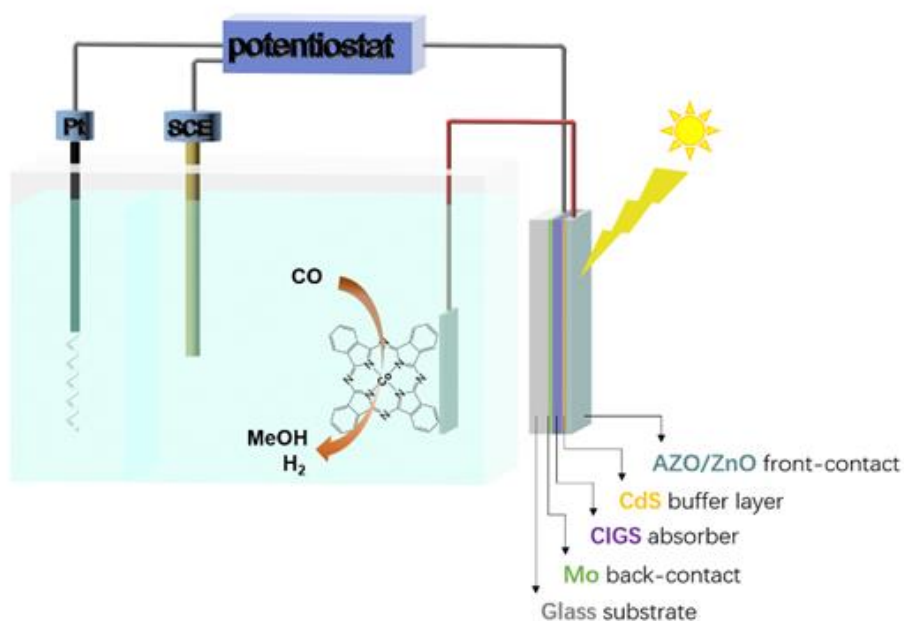


Figure 3.2 Scheme of the PV-EC system combining a CIGS PV cell linked to a CoPc loaded carbon paper used as the working electrode for CO₂ reduction in the EC unit.

3.3.1 CIGS cell characterizations

The structure of the CIGS PV cell used in this work is shown in Figure 3.2. As introduced in Chapter 2, the p-type CIGS thin films were synthesized following a so called CuPRO-process (described in Chapter 4). The ratio of gallium to indium within the films was large enough to yield an absorber band gap of 1.6 eV, measured from absorption threshold of the external quantum efficiency (Figure 3.3).

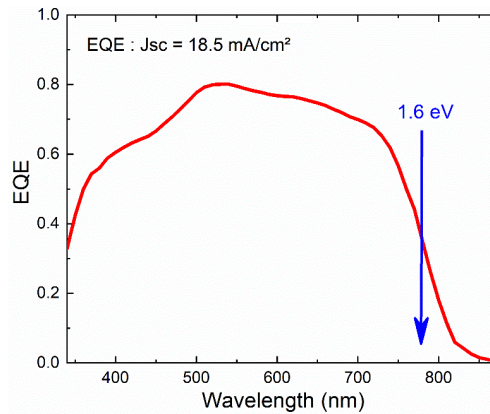


Figure 3.3 External quantum efficiency (EQE) of the CIGS solar cell. The blue arrow indicates the bandgap energy.

The glass/Mo/CIGSe structures were covered with n-type CdS, deposited by chemical bath deposition (CBD), and sputtered ZnO/ZnO:Al bilayer. For the sample operated herein, no electron collection grids were applied to the solar cells, which is at the origin of the limited device fill factor (FF). The typical photovoltaic parameters deduced from current-voltage characteristics (Figure 3.4) are: $V_{oc} = 680\text{-}700$ mV, $J_{sc} = 18.0\text{-}18.5$ mA/cm², $FF = 58\text{-}62$ %, leading to an overall photovoltaic conversion efficiency of ~ 8 %.

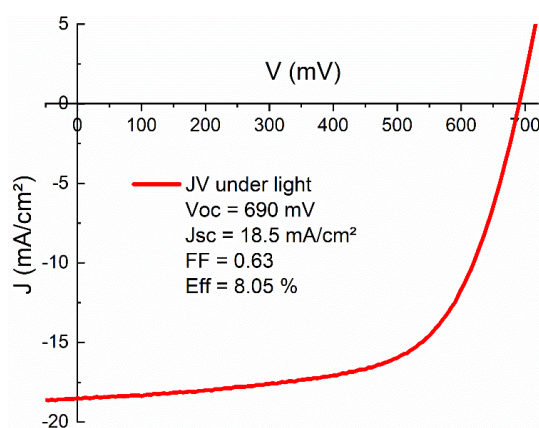


Figure 3.4 Current-voltage (J-V) response of the CIGS solar cell, with corresponding open circuit potential (V_{oc}), short circuit current density (J_{sc}), fill factor (FF) and PV conversion efficiency (Eff).

3.3.2 Preparation of porous carbon-CoPc electrode

To make the catalyst film, a catalytic ink was prepared by mixing CoPc with multi-walled carbon nanotubes (MWCNT) and Nafion resin in a mixture of ethanol and ethylene glycol, to obtain a stable colloidal solution (see Chapter 6 Experimental Section, for details). Ink deposition onto porous carbon paper was made by drop casting, and the operational catalytic film was obtained after drying at 100°C. This preparation is similar to the method used previously in the laboratory.

3.3.3 Photo-assisted electrolysis cell assembly

On the external CIGS PV cell, a front (–) and a back (+) lateral contacts were taken on AZO and Mo layers with copper wire, respectively. The front side (AZO layer) was connected to a carbon paper electrode with copper wire, and the back side was connected to an Autolab potentiostat. Regarding the EC part, a standard three-electrode configuration was employed with a Pt mesh as the counter electrode, which was separated from the working compartment by a glass frit bridge filled with the same electrolyte, and a saturated calomel electrode (SCE) as reference electrode (Ref).

3.4 Photovoltaic-Electrochemical performance for CO₂ reduction

PV-EC experiments were performed with a PGSTAT 302N Autolab potentiostat–galvanostat. Solutions were systematically purged with Ar for 15 min to remove atmospheric O₂, and then saturated with the gas of interest by bubbling more than 20 min before any measurement. Irradiation was performed with a 150 W xenon lamp (see

details in Chapter 6).

3.4.1 CO₂ as reactant

We first explored the ability of the PV-EC assembly to drive the reduction of CO₂. In Figure 3.5, linear sweep voltammetry (LSV) measurements show that no catalytic wave was observed in the absence of illumination, illustrating the need for photons and photovoltage from the CIGS cell to activate the catalyst and to reach the required potential to reduce CO₂. Moreover, Chopped-light experiments clearly showed that a significant 2-3 mA photocurrent (corresponding to 4-6 mA cm⁻² relatively to the carbon electrode surface) can be obtained upon illumination, associated with a typical photovoltage from the CIGS cell of *ca.* 660 mV.

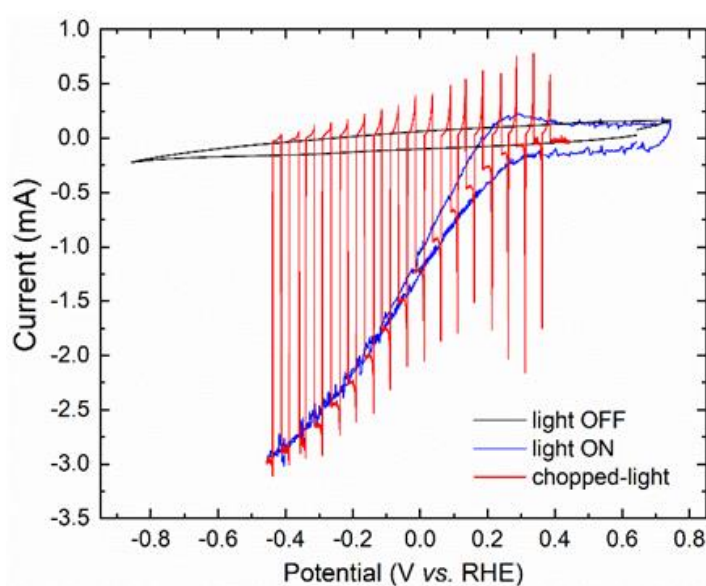


Figure 3.5 Linear sweep voltammetry of the CIGS (PV) coupled to CoPc/carbon paper (EC) modified electrode with light off (black), light on (blue) and chopped-light (red) in 0.1 M KHCO₃ (pH 6.8) electrolyte, under CO₂ atmosphere ($S_{\text{CIGS}} = 0.9 \text{ cm}^2$ and $S_{\text{carbon paper}} = 0.5 \text{ cm}^2$).

Figure 3.6 shows the evolution of the current with time during controlled potential photoelectrolysis under CO₂ atmosphere at pH 6.8 and different applied bias voltage. The electrolysis experiment was conducted at -0.36 V vs. RHE for 1 h with an average current of 2.35 mA. Then, another electrolysis was performed at -0.46 V vs. RHE for 2 h with an average current of 2.83 mA. Under both conditions, the main reduction product was CO with small amounts of H₂ and methanol (Table 3.1 entries 1-2).

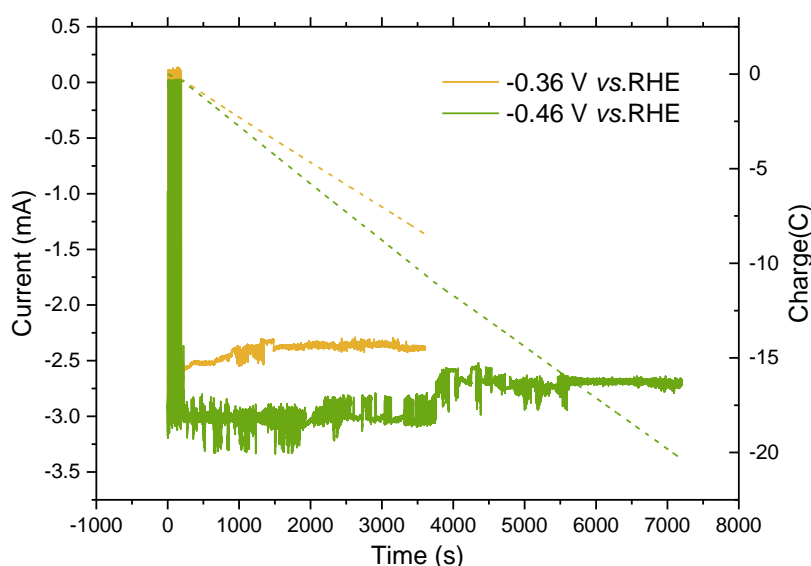


Figure 3.6 Controlled potential photo-electrolysis at -0.36 (orange) and -0.46 (green) V vs. RHE applied bias of the illuminated CIGS (PV) coupled to CoPc/carbon paper (EC) assembly in 0.1 M KHCO₃ (pH 6.8) electrolyte, under CO atmosphere, with $S_{\text{CIGS}} = 0.9 \text{ cm}^2$ and $S_{\text{carbon paper}} = 0.5 \text{ cm}^2$

3.4.2 CO as reactant

Based on our previous studies showing that CO is a key intermediate to further reduced compounds, we then explored the direct use of pure CO as starting reactant in

basic conditions, as described in our initial electrochemical study. [123]

Electrolysis experiments were performed in 0.1 M KOH (pH = 13) and at different applied bias voltage (Figure 3.7). Notably, during the first 200 s, a chopped-light experiment was conducted to check for the photo-response of the system, which explains the shape of the current signal (Figure 3.8). Very interestingly, methanol was produced in significant amount, further illustrating that CO is an intermediary step to further reduction. During 2 h electrolysis, a quite stable current of 1.18, 1.32 and 2.10 mA was observed at bias voltage of -0.09, -0.14 and -0.19 V vs. RHE respectively (Table 3.1, entries 3-5). The more negative the bias voltage the higher the total current, with H₂ as main product and in increasing proportion. A maximum 19% FE for methanol was obtained at -0.14 V vs. RHE (Table 3.1, entry 4), while at a positive bias voltage of +0.01 V vs. RHE, no current was observed (Table 3.1, entry 6), with no CO conversion occurring.

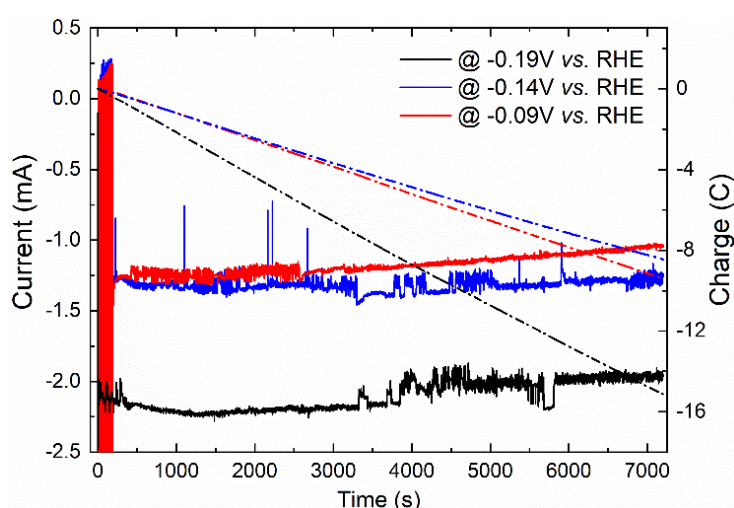


Figure 3.7 Controlled potential photo-electrolysis at -0.09 (red), -0.14 (blue) and -0.19 (black) V vs. RHE applied bias to the illuminated CIGS (PV) coupled to CoPc/carbon

paper (EC) assembly in 0.1 M KOH (pH 13) electrolyte, under CO atmosphere, with $S_{\text{CIGS}} = 0.9 \text{ cm}^2$ and $S_{\text{carbon paper}} = 0.5 \text{ cm}^2$.

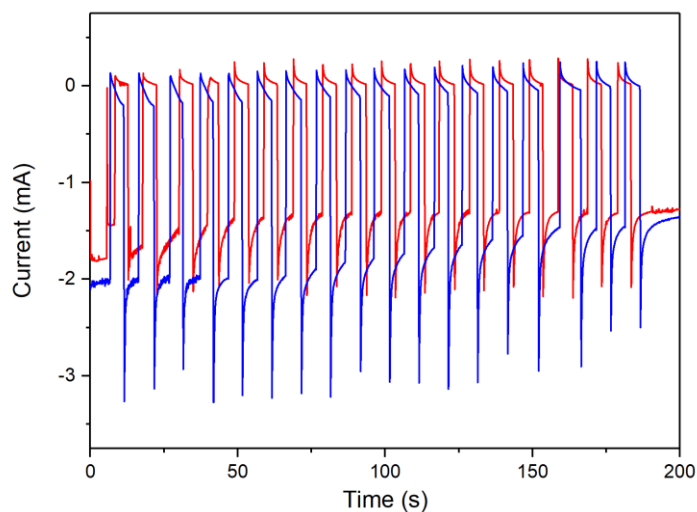


Figure 3.8 Chopped light experiment of the first 200 s of the electrolysis shown in Figure 3.7. The color code is identical to Figure 3.7.

3.4.3 Labeled experiments

After electrolysis under CO atmosphere at -0.14 V vs. RHE , a ^1H NMR spectrum of the electrolyte (see Figure 3.9 Grey) shows a series of peaks at both side of the broad $-\text{OH}$ peak (4.79 ppm). Among them, two could be attributed to CO reduction products: formate (singlet at 8.44 ppm) a commonly reported product, and methanol (singlet at 3.34 ppm). Then isotope labelled experiments under ^{13}CO atmosphere were conducted to confirm that CH_3OH originated from CO.

A labeled experiment under ^{13}CO atmosphere is indeed compulsory to conclude on the nature and the origin of this peaks as shown in Figure 3.9 magenta (see details in Chapter 4). In such conditions, both the 3.34 and 8.44 ppm peaks are splitted with a respective J_{CH} strength characteristic of methanol and formate, definitively proving the

presence and the origin of these products. [130] Note that the small amount of formate may arise from reaction of CO with OH⁻ and from the disproportionation of small amount of formaldehyde form during electrolysis. [123, 131]

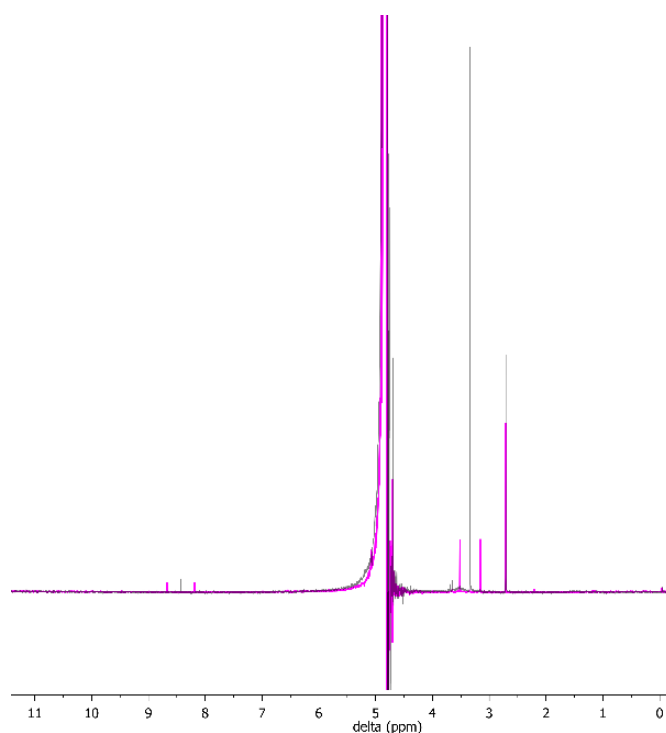


Figure 3.9 ¹H NMR spectrum showing the characteristic doublet signal of methanol (violet, CH₃ protons, $\delta = 3.16$ and 3.52 ppm) due to ¹³C, measured after 1 h CPE at $E_{\text{applied}} = -0.14$ V vs. RHE of the illuminated CIGS (PV) coupled to CoPc/carbon paper (EC) assembly in 0.1 M KOH (pH 13) electrolyte, under ¹³CO atmosphere (with $S_{\text{CIGS}} = 0.3$ cm² and $S_{\text{carbon paper}} = 1$ cm²). A reference spectra obtained upon electrolysis under ¹²CO atmosphere is shown in light grey (the singlet due to CH₃ protons of CH₃OH appears at $\delta = 3.34$ ppm).

3.4.4 Effects of area ratio of $S_{\text{carbon electrode}}$ and S_{CIGS}

To optimize the EC part, we investigated the influence of the surface area of the carbon paper electrode. At a fixed CIGS surface area of 0.9 cm^2 , three carbon paper electrode areas, 0.5 , 1 and 1.5 cm^2 were tested (Figure 3.10). While the current was multiplied by a factor of 2 when going from 0.5 (Table 3.1, entry 4) to 1 cm^2 (entry 7), almost no current increase was noticed with a further increase to 1.5 cm^2 (entry 8). This seems to indicate that an insufficient amount of electrons was provided by the CIGS PV cell to fully feed an electrode of such area. It is worth noting that, when the surface area of carbon paper electrode reached 1 cm^2 , the FE for methanol got to a maximum value of 21 %.

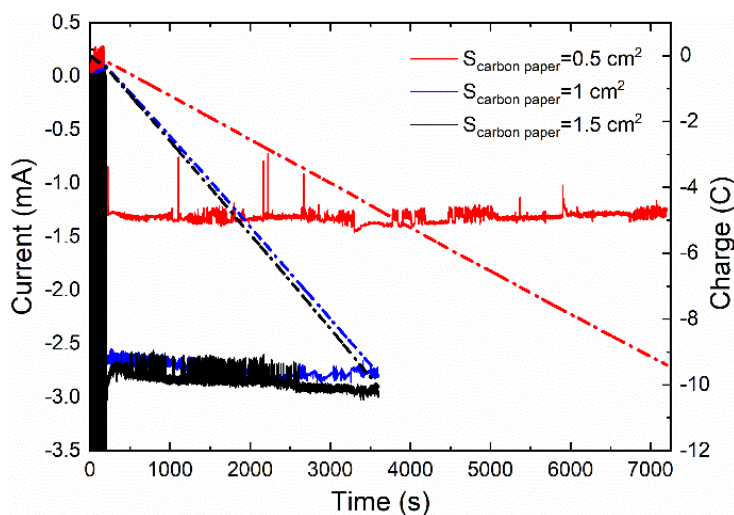


Figure 3.10 Controlled potential photo-electrolysis at $E_{\text{applied}} = -0.14 \text{ V vs. RHE}$ of the illuminated CIGS (PV) coupled to CoPc/carbon paper (EC) assembly in 0.1 M KOH ($\text{pH } 13$) electrolyte, under CO atmosphere, with $S_{\text{CIGS}} = 0.9 \text{ cm}^2$ and $S_{\text{carbon paper}} = 0.5$ (red), 1 (blue) and 1.5 (black) cm^2 .

Blank experiment was conducted under argon atmosphere (Table 3.1, entry 9) with $1 \text{ cm}^2 S_{\text{carbon paper}}$, and we observed no CO or methanol production, only H_2 was detected in a similar amount than under CO atmosphere, suggesting an independent reaction pathway to hydrogen.

3.4.5 Long-term stability investigation

To evaluate the stability of the PV-EC assembly and the evolution of the products generated with time, we conducted an extended electrolysis under CO atmosphere for 7 h at -0.14 V vs. RHE in 0.1 M KOH ($\text{pH} = 13$). Both liquid and gaseous reduction products were analyzed periodically (Table 3.2). As can be seen in Figure 3.11, even if a little bit fluctuating, the current remained quite constant over the electrolysis course, at a average value of -1.75 mA , together with a linear evolution of the charge passed.

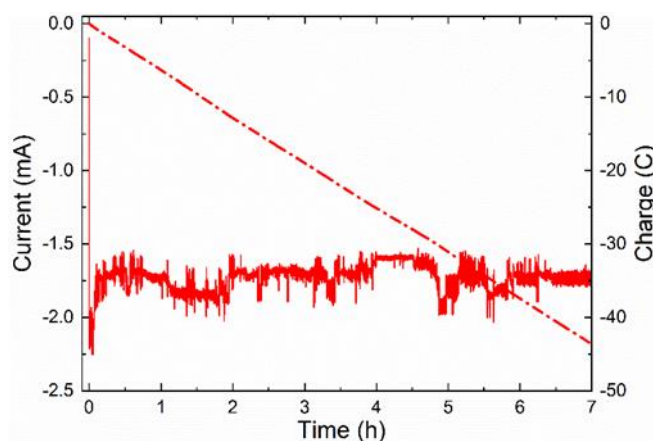


Figure 3.11 Extended controlled potential photo-electrolysis at -0.14 V vs. RHE applied bias of the illuminated CIGS (PV) coupled to CoPc/carbon paper (EC) assembly in 0.1 M KOH ($\text{pH} = 13$) electrolyte, under CO atmosphere, with $S_{\text{CIGS}} = 0.3 \text{ cm}^2$ and

$S_{\text{Carbon paper}} = 1 \text{ cm}^2$ (full red line: current; dotted line: charge).

Gas chromatography and ^1H NMR analysis of the products revealed that, first, FE for methanol was progressively lowered from 16% after the first electrolysis hour to 10% after 7 h (Table 3.2). Hydrogen FE was concomitantly increased from 65 to 70% FE. However, cumulated molar concentration of methanol in the reaction mixture evolved linearly over the whole process up to a total amount of 2.4 mM. Additionally, methanol production occurs at a very low overpotential. The reasons for progressive decrease of methanol production (catalyst leaching from the electrode, catalyst degradation in the film) remain unclear and are currently investigated in our laboratory.

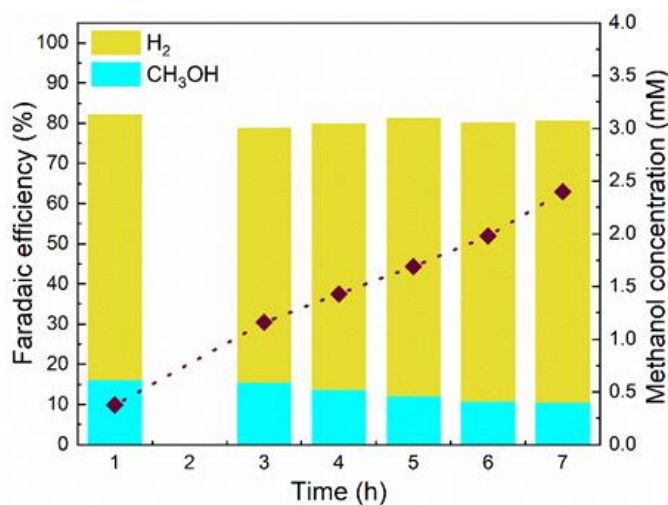


Figure 3.12 Evolution of the Faradaic efficiency in H₂ (green) and methanol (blue) and of methanol concentration (wine diamonds) during a long-time controlled potential photo-electrolysis at $E_{\text{applied}} = -0.14 \text{ V vs. RHE}$ of the illuminated CIGS (PV) coupled to CoPc/carbon paper (EC) assembly in 0.1 M KOH (pH 13) electrolyte, under CO atmosphere. $S_{\text{CIGS}} = 0.3 \text{ cm}^2$ and $S_{\text{Carbon paper}} = 1 \text{ cm}^2$.

3.5 Overall efficiency approach

According to our previous work, in terms of application, the choice of going sequentially, CO₂ reduction to CO in a first electrolyzer followed by CO reduction into methanol in a second one, rather than using a single reactor will be mainly cost-driven. Concerning these two electrolyzers in series, operating the theoretical cathodic reaction described in equation 3.1, overall cathodic Faradaic efficiency expression is shown in equation 3.2. Application of this overall Faradaic efficiency calculation to the reactions involved in this manuscript is pictured in Figure 3.13 It shows that sequential reduction of CO₂ to methanol allows to increase the overall Faradaic efficiency up to 28.4%.



$$\text{FE}_{\text{sequential}} = \frac{\alpha_1 + \alpha_2}{\frac{\alpha_1}{\text{FE}_1} + \frac{\alpha_2}{\text{FE}_2}} \quad (3.2)$$

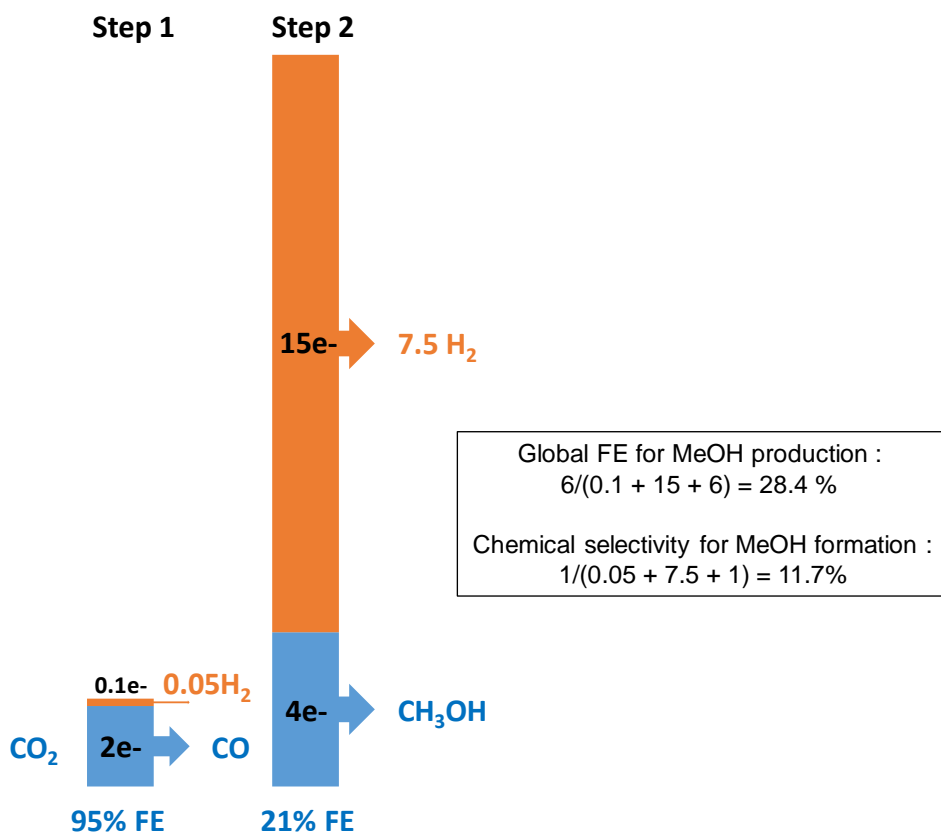


Figure 3.13 Overall Faradaic efficiency (FE) and chemical selectivity for sequential reduction of CO₂ to CH₃OH, taking into account a two steps procedure with first CO₂-to-CO conversion with 95% Faradaic efficiency and then reduction of CO to CH₃OH with a Faradaic efficiency of 21%.

3.6 Conclusions and perspectives

In this chapter, we have showed promising results with the combination of a CIGS PV cell with a molecular catalyst deposited on a carbon electrode to achieve the solar assisted reduction CO₂ to CO and then to methanol reduction in aqueous media. The origin of carbon products was asserted by isotope labelled experiments. In this PV-EC system, the electrochemical part is only based on abundant elements (carbon, cobalt complex) and is operational at ambient pressure and temperature, the employed

molecular catalyst belonging to an already industrially used compounds (cobalt phthalocyanine).

CIGS unit showed high efficiency and supplies a large photovoltage to feed the EC unit. The formation of mM amounts of methanol was reached after few hours of electrolysis at very moderate applied bias.

First stability tests are highly encouraging, with no great loss of activity during several hours. Our results indicate that the performance of the system depend on the surface area matching between the PV cell and the electrode. More work is under way to gain both in understanding and in productivity.

Table 3.1 PV-EC CO₂ and CO electrochemical reduction performance with CoPc decorated carbon paper electrode powered by a CIGS PV cell.

Entry	Electrolyte	Substrate	Electrolyte	Time (h)	T	E _{applied} (V vs. RHE)	S _c (carbon paper) (cm ²)	S _c (IGS) (cm ²)	S _c (MCNTs) (cm ²)	at. %	m _c (m)	a	η (mV)	i _{total} (mA)	CH ₃ OH			CO			H ₂				
															F (%)	i (mA)	E (%)	F (%)	i (mA)	FE (%)	F (%)	i (mA)	FE (%)		
1	CO ₂	KHCO ₃	0.1 M pH 6.8	1	-	0.36	5	9	0	15	1:	90	3	.35	2	.03	0	05	1	.35	2	7	.16	0	
2				2	-	0.46	5	9	0	15	1:	90	4	.83	2	.3	0	.01	0	08	1	.83	2	8	.23
3	CO	KOH	0.1 M pH 13	2	-	0.19	5	9	0	15	1:	90	2	.10	2	2	1	.25	0	-	-	7	8	.83	1
4				2	-	0.14	5	9	0	15	1:	40	2	.32	1	9	1	.25	0	-	-	5	6	.86	0
5	CO	KOH	0.1 M pH 13	2	-	0.09	5	9	0	15	1:	90	1	.18	1	.5	8	.10	0	-	-	0	6	.71	0
6				2	+	0.01	5	9	0	15	1:	0	9	-	0	-	0	-	-	-	-	-	-	-	-
7	Ar	KHCO ₃	0.1 M pH 6.8	1	-	0.14	1	9	0	15	1:	40	2	.75	2	1	.58	0	-	-	3	7	.01	2	
8				1	-	0.14	5	9	0	15	1:	40	2	.85	2	5	1	.43	0	-	-	8	7	.22	2
9	Ar	KHCO ₃	0.1 M pH 6.8	1	-	0.14	1	9	0	15	1:	40	2	.39	3	-	-	-	-	-	-	3	7	.47	2
				1	-	0.14	1	9	0	15	1:	40	2	.39	3	-	-	-	-	-	-	-	3	7	.47

Table 3.2 Current (i) and faradaic efficiency (FE) during controlled potential photo-electrolysis at $E_{\text{applied}} = -0.14$ V vs. RHE, with CoPc:MWCNT mass ratio of 1:15, in 0.1 M KOH (pH 13) electrolyte, under CO atmosphere, with $S_{\text{CIGS}} = 0.3$ cm² and $S_{\text{Carbon paper}} = 1$ cm².

Time (h)	i_{total} (mA)	CH ₃ OH		H ₂	
		FE (%)	i (mA)	FE (%)	i (mA)
1	1.74	16.2	0.28	65.9	1.15
3	1.75	15.6	0.27	63.3	1.11
4	1.74	13.6	0.24	66.2	1.15
5	1.73	12.1	0.21	69.2	1.2
6	1.73	10.7	0.19	69.3	1.20
7	1.73	10.5	0.18	70.2	1.21

Chapter 4 - Preliminary investigation of PEC CO₂ reduction on p-GaP semiconductors associated with molecular catalysts

4.1 PEC reduction of CO₂ on GaP semiconductors

GaP is a semiconductor with a band gap of about 2.3 eV. [132] The wide bang gap theoretically provides enough energy to split water directly in a PEC cell. Additionally, it is a promising electrode because of its stability in electrolytes under cathodic conditions. This is caused by the slow kinetics of the cathodic dissociation reaction of GaP and by the rapid formation of a thin oxide layer.[133]

Therefore, GaP has been quite intensively studied for PEC-applications. In 1978, Halmann's group first reported CO₂ reduction on p-GaP under 365 nm illumination with an applied potential of -1.4 V (vs. SCE). [134] In 1979, Fujishima and Honda demonstrated photoelectrocatalytic reduction of CO₂ to formaldehyde and methanol by irradiating TiO₂ and GaP with the UV light at a potential of -1.5 V (vs SCE). [103] Petit et al. later reported PEC reduction of CO₂ to CO on p-GaP semiconductor associated with molecular Ni(cyclam)²⁺ in aqueous medium. The Faradaic efficiency for CO was 83% at a potential as early as 0.46 V vs. RHE with H₂ as the only byproducts. [135] Bocarsly's group reported pyridinium-catalyzed CO₂ reduction on GaP photocathodes with applied potentials between -0.7 V and -0.2 V (vs SCE) under UV light. [30] More recently, Cronin group reported PEC reduction of CO₂ to methanol using TiO₂

passivated GaP photocathodes under 532 nm wavelength illumination. They investigated the effects of TiO₂ thickness on the performances. The TiO₂ passivation layer successfully stabilizes the GaP surface in solution, preventing it from photocorrosion.[136] In these studies, no experimental evidence showed that methanol is issued from CO₂ reduction. Despite these interesting early results, high efficient and long-term stable system towards CO₂ reduction has not yet been designed.

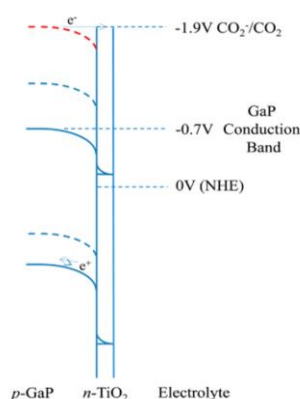


Figure 4.1 Energy band alignment of GaP and TiO₂. [136]

We adopted the strategy to deposit a n-TiO₂ thin layer by atomic layer deposition (ALD) on a GaP semiconductor as a photoelectrode, in association with a molecular catalyststo drive PEC reduction of CO₂. On one hand, the TiO₂ deposited by ALD is n-type due to oxygen vacancies and forms a p-n junction with the underlying p-type GaP photocathode. This creates a built-in field that should assist the separation of photogenerated electron–hole pairs, further reducing recombination (Figure 4.1). On the other hand, the TiO₂ passivation layer may stabilize the GaP surface in solution, preventing it from photocorrosion. Zn doped p-type (100) oriented GaP semiconductors were obtained from Universitywafers (USA). One side is polished and another side is matt. The thickness is 430 μm and the surface area is 0.9~1 cm² (Figure 4.2).

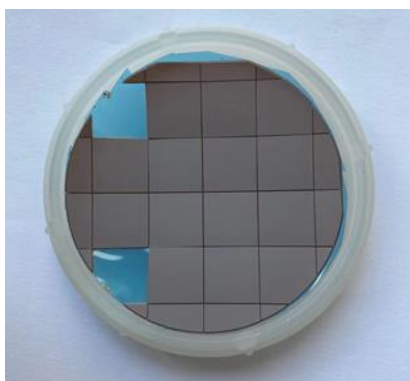


Figure 4.2 Bare p-GaP semiconductors

4.2 HER performance of p-GaP based photoelectrode

4.2.1 Preparation of photoelectrode

Firstly, an ohmic contact was made to the back of the crystal using an indium-gallium solder. The contact was then connected to the external circuitry with a copper wire. Scotch (3M) tape was used to cover the connections and only expose the front face of the semiconductor to the solution (Figure 4.3).



Figure 4.3 p-GaP photoelectrode as prepared in this work.

4.2.2 Hydrogen evolution reaction at bare GaP photoelectrode

The wide bang gap of GaP semiconductor theoretically provides enough energy to directly split water in a PEC cell. The Cronin group reported photocatalytic water splitting on TiO₂ passivated GaP. The TiO₂ passivation layer prevents corrosion of the

GaP surface, making it stable in pH = 0 solution.

In order to check the preparation of the photoelectrode and the PEC properties of this obtained GaP material, a simple HER reaction was explored in 0.5 M H₂SO₄. Irradiation were performed with the light of a Xe lamp (150 W) combined with a Schott GG435 long pass filter and 2-cm-long glass (OS) cell filled with deionized water to cut off infrared and low ultraviolet incident photons. PEC experiments were performed in a three-electrode system using a Pt counter electrode and a SCE reference electrode separated from the working electrode compartment by bridges. Figure 4.4 shows the CV curves for bare GaP measured in 0.5 M H₂SO₄ (pH = 0.3) solution. Bare GaP under light irradiation (black curve) has an onset for photocurrent at a potential of approximately -0.2 V vs. RHE.

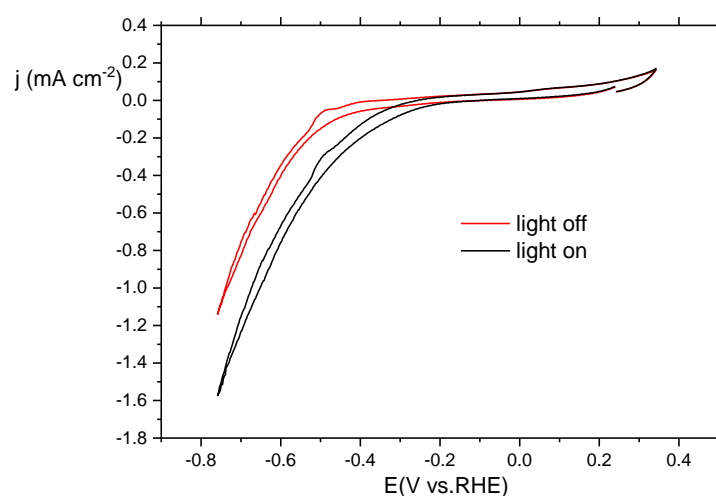


Figure 4.4 CV in PEC conditions at a GaP electrode in 0.5 M H₂SO₄ under air atm. Scan rate was 100 mV s⁻¹.

4.3 Homogeneous PEC reduction of CO₂ on GaP based photoelectrode with molecular catalyst

4.3.1 Preliminary experiments in aqueous solution

Iron tetra (o-N,N,N,N-trimethylanilinium) porphyrin (abbreviated as Fe-o-TMA, Figure 4.5) is a water-soluble molecular catalyst. In our previous work, Fe-o-TMA showed excellent electrochemical CO₂-to-CO-conversion performance. [117] In the work presented here, we used a GaP semiconductor passivated by TiO₂ (5 nm) as photoelectrode associated with Fe-o-TMA catalyst to drive CO₂ reduction in PEC cells.

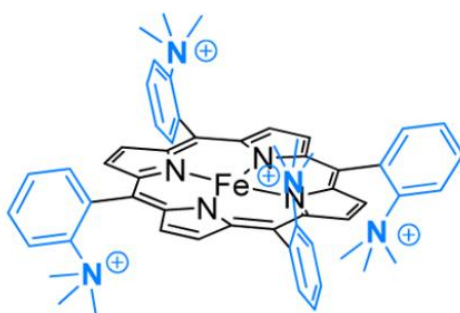


Figure 4.5 Structure of iron tetra-phenyl porphyrin (Fe-o-TMA) catalyst.

Electrolysis was performed at -0.35 V vs. RHE for 2h (Figure 4.6) on bare GaP and GaP passivated with TiO₂ in a CO₂ saturated pH = 6.8 solution of 0.1 M KHCO₃ under illumination. The concentration of Fe-o-TMA catalyst was 200 μM. Bare GaP (blue) showed an average current density of 13 μA cm⁻² and increased gradually with time. For the TiO₂ passivated GaP, we get a smaller current density of 6 μA cm⁻². The products were investigated through gas chromatography analysis. In both conditions, no products were detected.

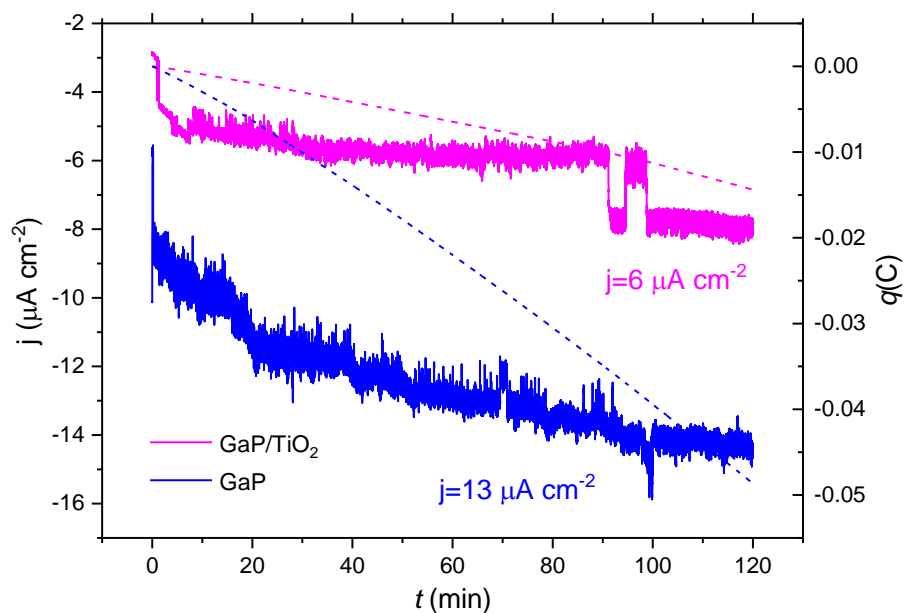


Figure 4.6 Photo-electrolysis at -0.35 V vs. RHE in 0.1M KHCO_3 saturated with CO_2 ($\text{pH} = 6.8$) (Catalyst concentration: $200 \mu\text{M}$).

As already pointed out [137], p-type GaP acts as a photocathode due to the direction of band bending at its interface with the solvent, promoting photoelectron flow to the water. For n-type semiconductors, the bending is usually upward, resulting in photohole flow to the water, as illustrated in Figure 4.7 (a). When the TiO_2 thickness is further increased, there is enough donor impurities to bend the band upward, hindering the electron flow to the water, as shown in Figure 4.7 (b). It is, therefore, somewhat surprising that when n-type TiO_2 with 5 nm thick is coated on top of p-GaP, the current density decreased. Further investigation will be done in our group to pursue these first unsuccessful tests.

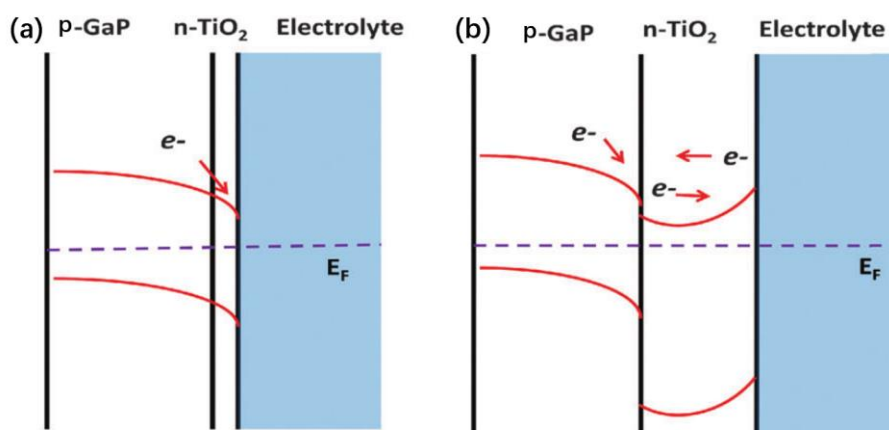


Figure 4.7 Energy band diagrams for (e) thin and (f) thick TiO_2 layers.[137]

4.3.2 Preliminary experiments in acetonitrile

Having in mind the good catalytic performance of CoPc molecular catalyst, we also preliminary explored a strategy using GaP as photoelectrode and CoPc as catalyst to drive PEC reduction of CO_2 in a homogeneous system. We adapted a new method to prepare to photoelectrode, on account of the corrosion of tape in organic solvent. Firstly, an ohmic contact was made to the back of the crystal using an indium-gallium solder and connected to an external lead with copper wire. Then we use an epoxy resin to expose only the front face of the semiconductor to solution.

According to the work of Sauvage et al., a small photocurrent could probably be due to a passive film formation on the top of GaP crystal. [138] A pretreatment was thus conducted before being used as photocathodes. The GaP crystals were etched in $\text{HF} + \text{HNO}_3 + \text{H}_2\text{O}$ (1: 3 : 4), and an ohmic contact (Au + Zn) was made on their back side by vapor deposition under vacuum, followed by 20 min heating at 400°C under an N_2 atmosphere. Before each experiment, the semiconducting electrode was successively enched in 1 M KOH and $\text{HF} + \text{HNO}_3 + \text{H}_2\text{O}$ (1: 3 : 4). LSV was performed in

acetonitrile in the presence of phenol (PhOH, 1 M) on a GaP photoelectrode under chopped light illumination (Figure 4.9), which showed a photo-response with an onset potential of -0.6 V vs. SCE and small photocurrent as well. A blank experiment was also conducted under Ar exhibiting negligible photocurrent in the same conditions (Figure 4.9). At that stage, and due to the small current density, electrolysis and product identification have not been performed.

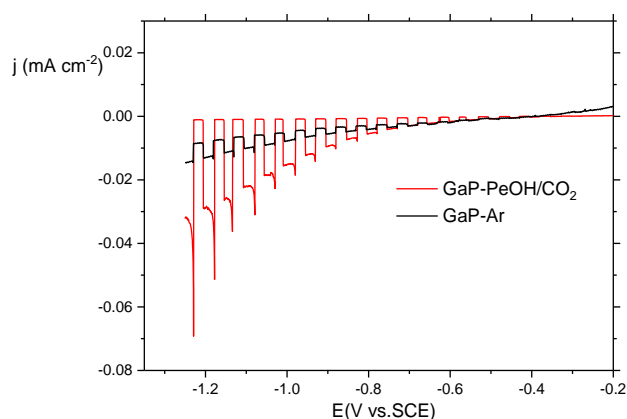


Figure 4.9 LSV in PEC conditions at a GaP electrode in acetonitrile under chopped light under Ar atmosphere (black) and after saturated with CO₂ (red) with phenol as a co-substrate (1 M). Scan rate was 5 mV s⁻¹. (catalyst concentration: 250 μM)

4.4 Perspectives

This work was just a first step. Beside the pretreatment process of the GaP crystals to increase the PEC performance, the thickness of TiO₂ protective layer needs to be optimized since it has a significant effect on the performance (e.g. resistances). Considering our previous work (described in Chapters 2 and 3), it should be interesting also to graft molecular molecular catalyst on the surface of GaP based photoelectrode.

Chapter 5 - General conclusions and perspectives

5.1 General conclusions

The main objective of this thesis was to explore the use of semiconductor materials associated to molecular catalysts for the visible-light driven photoelectrochemical reduction of CO₂ in aqueous solutions. CIGS semiconductor was introduced because of its high efficiency and low cost in producing solar electricity. This thin-film device has been well studied and characterized for several PV applications. In this work, efficient CIGS solar devices were fabricated and characterized, and the CIGS electrodes have been successfully used for CO₂ catalytic reduction in different configurations with the assistance of molecular catalysts. Cobalt-based molecular catalysts, such as the quaterpyridine complexes used in this work, are capable of driving CO₂ reductions in heterogeneous water conditions with several supporting materials. The results in this thesis have illustrated the combination of CIGS devices and functionalized cobalt quaterpyridine molecular catalyst. Most importantly, the photoelectrochemical reduction of CO₂-to-CO was achieved at the photocathodes, under visible-light in water. In a complementary approach, thin films made of Co phthalocyanine and multi-walled carbon nanotubes were used to drive reduction of CO₂-to-methanol with a photovoltaic CIGS device in a PV-EC system, again in water. Both high catalytic efficiency, selectivity as well as stability could be obtained. More precisely, the main results of this work can be summarized as follows:

1. We successfully demonstrated the application of CIGS photovoltaic materials

for photoelectrochemical reduction of CO₂. Cobalt quaterpyridine complexes were functionalized and homogeneously immobilized on a TiO₂ upper layer on CIGS. Various spectroscopic characterization techniques showed no structural damage and loss of activity of the catalyst. A PV-EC configuration was designed with a carbon paper electrode to load the catalyst connected to a CIGS device. Average current density of 3.25 mA cm⁻² and a selectivity of 87% for CO were obtained with a bias potential of -0.06 V vs. RHE in water, corresponding to a formally negative overpotential relatively to the thermodynamic potential ($\eta = -50$ mV). A long-term electrolysis for 7 h showed a good stability and the selectivity for CO was maintained between 82% and 85% over the whole experiment course. Then a PEC configuration was developed to combine CIGS photocathode with functionalized catalyst, leading to a selectivity of 97% for CO₂ (and 3 % for H₂ as the only by-product) at -0.06 V vs. RHE, corresponding gain to a formal overpotential of -50 mV in pure aqueous media. The photocathodes were stable for a couple of hours. At low overpotential (less than 100 mV), current density up to 3-4 mA cm⁻² could be obtained in chopped-light, short time experiment. When compared to previously reported PEC CO₂ reduction systems, even those employing rare metal complex as catalyst, this work shows excellent performance.

2. Encouraged by these results, we further investigated decoupling the process of CO₂ reduction to methanol in order to maximize efficiency, upon first realizing CO₂-to-CO reduction in optimized conditions in an electrochemical cell and then using CO as a reactant in a second photoelectrochemical cell, in aqueous solution (basic conditions). In a PV-EC system, we successfully combined a carbon paper electrode

loaded with cobalt phthalocyanine catalyst and a CIGS PV cell to drive CO reduction to methanol. CIGS PV cell supplies a large photovoltage to the EC unit. A Faradaic efficiency of 21% for methanol was obtained with a bias potential of -0.06 V vs. RHE, corresponding to an overpotential of 240 mV. The performances of the system depend on the surface area matching between CIGS and the carbon paper electrode. A long-term electrolysis for 7 h showed progressive albeit small loss of activity during the time, and the origin of methanol product was asserted by isotope labelled experiments.

5.2 Future perspectives

This work paves the way to the development of more efficient systems for PEC reduction of CO₂. Because of the complexity of solar-driven reduction system, the performance is controlled by several factors, including light absorption, charge transfer, catalytic activity, and engineering techniques as well. The ability to design an efficient and stable photoelectrode integrating molecular catalysts, allowing to properly synchronize in time and space all steps of the process remains a challenge.

A highly active catalyst is essential to get high efficiency. Considering the advantages of molecular catalyst, developing earth-abundant metal based efficient molecular catalyst is still very promising. A higher catalyst loading would also significantly improve the performance. Improve the specific surface area eg. upon nano-structuration of the surface is certainly an approach to be followed. Besides, it is still a challenge to design molecular catalyst to drive CO₂ reduction beyond two-electron process, so as to produce liquid fuels (e.g. methanol).

Different semiconductor materials may be explored for PEC reduction of CO₂ to expand light absorbers, produce large current densities and photovoltage. As described in Chapter 4, we did a start to investigate GaP semiconductor as photoelectrode.

A thorough understanding of the catalytic pathways and the deactivation process (such as the reasons for catalyst leaching and/or degradation, (un)stability of protective oxide layers) is essential to improve the catalytic activity and long-term stability. Finally, designing a fully unassisted solar-driven fuel production system may also be investigated when coupled with an appropriate photoanodic reaction.

Currently, this work has led to two publications:

1. "CO₂ reduction to methanol with a molecular cobalt catalyst loaded porous carbon electrode assisted by a CIGS photovoltaic cell"

R. Wang, E. Boutin, N. Barreau, F. Odobel, J. Bonin, M. Robert, *ChemPhotoChem* **2021**, 5, 705-710.

2. "Photocathode functionalized with a molecular cobalt catalyst for selective CO₂ reduction in water"

P. B. Pati, E. Boutin, R. Wang, S. Diring, S. Jobic, N. Barreau, F. Odobel, M. Robert, *Nat. Commun.* **2020**, 11:3499.

Chapter 6 - Experiments and Methods

6.1 Chemicals and synthesis

6.6.1 Commercial chemicals

Solids

KHCO_3 (99.5%) and KOH (99.5%) were purchased from Merck; KH_2PO_4 (97%) was purchased from Prolabo; K_2HPO_4 (99.5%) was purchased from Labosi; Cobalt phthalocyanine (CoPc, β form, 97% dye content) and multi-walled carbon nanotubes (MWCNTs, 6-9 nm diameter, 5 μm length, > 95% Carbon) were purchased from Sigma-Aldrich; carbon paper (Toray Carbon Paper, TGPH-60) was purchased from Alfa Aesar.

All chemicals were used as received without any further purification.

Liquids and solvents

Acetonitrile (99.8%), ethylene glycol (EG, reagent plus > 99%) and Nafion[®] (5 wt% solution in low aliphatic alcohol/ H_2O) were purchased from Sigma-Aldrich; ethanol (EtOH, analysis grade) was purchased from Merck.

Electrolyte solutions were prepared with ultra-pure water (TKA MicroPure, 0.055 $\mu\text{S cm}^{-1}$) or electrochemical grade acetonitrile.

Gases

$^{12}\text{CO}_2$ (> 99.7%), ^{12}CO (> 999.7) and Argon (> 99.998) gases were purchased from Air Liquide. $^{13}\text{CO}_2$ (99% content in atom ^{13}C) was purchased from Sigma-Aldrich.

6.1.2 Synthesis and purifications

Synthesis of Co-qPyH

Cobalt quaterpyridine used in this manuscript is prepared with planar tetradentate ligand 2,2':6',2'':6'',2'''-quaterpyridine (Co-qPyH). Specifically, (1E,5E)-1,6-bis(4-bromophenyl)hexa-1,5-diene-3,4-dione (**1**) was synthesized as previously reported method (illustrated in Figure 2.7). A 2,3-butadione (2.58 g, 3 mmol) solution was added dropwise to a continuously stirred MeOH solution of 4-bromobenzaldehyde (11.1 g, 6 mmol) and piperidine (0.6 ml, 0.6 mmol) using a dropping funnel in 10 min. Then, the mixture was heated overnight. The solution was cooled in an ice bath, and the obtained orange precipitate was filtered and washed thoroughly with diethyl ether. The orange compound was dried under vacuum to yield 2.71 g of compound **1**, which was used directly for the following steps.

In order to get compound **2**: 4',4''-bis(4-bromophenyl)-2,2':6',2'':6'',2'''-quaterpyridine, compound **1** (420 mg, 1.0 mmol) was added to a solution of the Kröhnke reagent N-[2-(2-pyridyl)-2-oxethyl] pyridinium iodide (652 mg, 3.26 mmol) and anhydrous ammonium acetate (8 g, excess) in absolute ethanol (40 mL). Then the mixture was heated under reflux for 24 h. The precipitate was filtered and washed thoroughly with diethyl ether after cooling. About 140 mg of compound **2** was generated (white powder) with 23% yield, which is insoluble in common organic solvents. ¹H NMR characterization is shown in Figure 6.1 (ppm, 300 MHz, 298 K, CDCl₃) δ 8.88 (d, J= 1.8 Hz, 2H), 8.75 (m, 2H), 8.74 (d, J= 1.8 Hz, 2H), 8.68 (dt, J= 4.8, 1.2 Hz, 2H), 7.92 (td, J= 8.1, 1.8 Hz, 2H), 7.79 (d, J= 8.7 Hz, 4H), 7.68 (d, J= 8.7

Hz, 4H), and 7.38 (dt, J= 4.8, 1.2 Hz, 2H); HRMS m/z calcd. for C₃₂H₂₁Br₂N₄ [M+ H]⁺ 619.0133, found 619.0137.

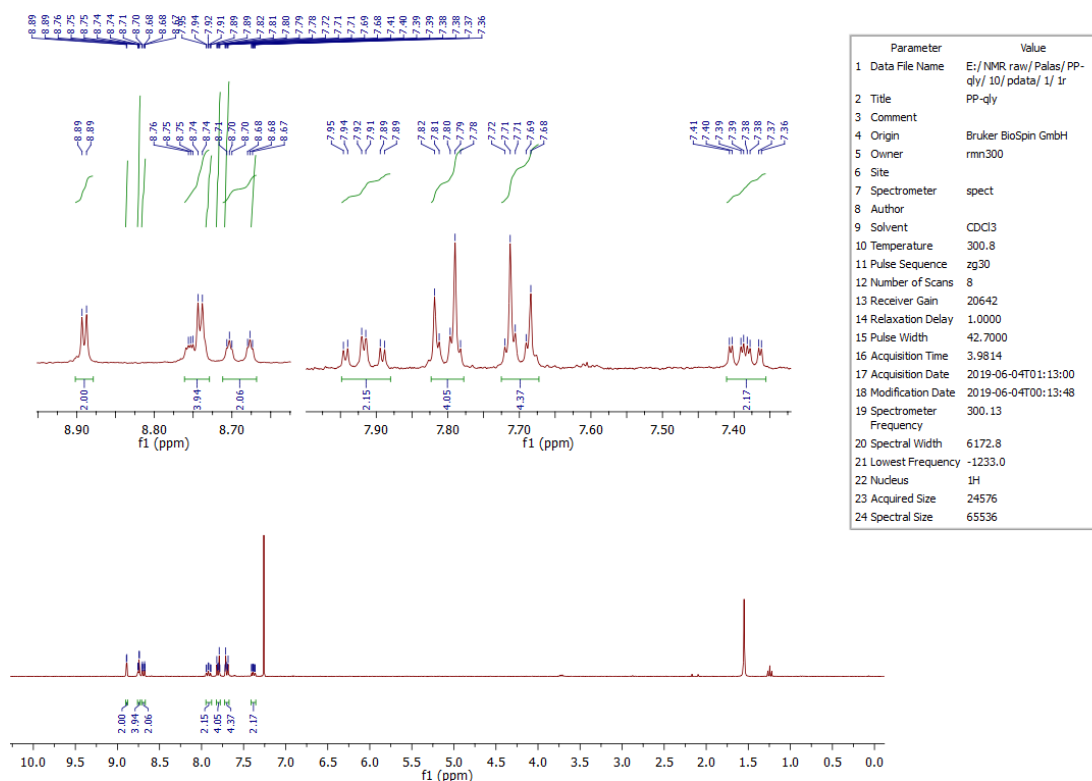


Figure 6.1 ¹H NMR spectrum of compound **2**.

Compound 3: tetraethyl ([2,2':6',2'':6'',2'''-quaterpyridine]-4',4''-diylbis(4,1-phenylene))bis (phosphonate) was obtained via Hirao cross-coupling reaction: Compound **2** (100 mg, 0.16 mmol), Pd(PPh₃)₄ (17 mg, 0.015 mmol), and Cs₂CO₃ (114 mg, 0.35 mmol) were mixed in anhydrous THF (4 mL) in a microwave vial (10 mL) with a stirrer bar inside under argon. Diethylphosphite (107 mg, 0.78 mmol, purged with Ar) was added into the mixture for 10 min. The mixture was heated to 110°C for 2.5 h with the vial sealed. A yellow solution was obtained after filtration. Then the solvent was evaporated under reduced pressure. The generated brown solid was dissolved in CH₂Cl₂ (20 mL) and stirred with decolorizing charcoal for 30 min and then filtered to remove all of the solvent under reduced pressure to get the oily bright-yellow

residue. It was dissolved in acetone (5 mL) and filtered through a short silica plug eluting with acetone (25 mL). A pale-yellow solution was obtained. The solvent volume was reduced to around 5 mL of cold pentane that was added, until compound **3** precipitated out from the solution. A white powder (compound **3**) was obtained (108 mg, 92%). ¹H NMR characterization is shown in Figure 6.2 (ppm, 400 MHz, 298 K, CDCl₃) δ 8.95 (d, J= 1.6 Hz, 2H), 8.80 (J= 1.6 Hz, 2H), 8.75 (m, 2H), 8.70 (dt, J= 8.0, 0.8 Hz, 2H), 8.01–8.03 (m, 8H), 7.93 (td, J= 7.6, 1.6 Hz, 2H), 7.38 (dt, J= 6.0, 1.2 Hz, 2H), 4.13–4.26 (m, 8H), and 1.38 (t, J= 6.8 Hz, 12H); ¹³C NMR characterization is shown in Figure 6.3 (ppm, 100 MHz, 298 K, CDCl₃) δ 156.5, 156.3, 156.1, 149.5, 149.4, 143.0, 137.2, 132.8, 132.7, 127.8, 127.6, 124.3, 121.6, 119.61, 119.56, 62.5, 62.4, 16.6, 16.5; HRMS m/z calcd. for C₄₀H₄₁N₄O₆P₂ [M+ H]⁺ 735.3501, found 735.3497.

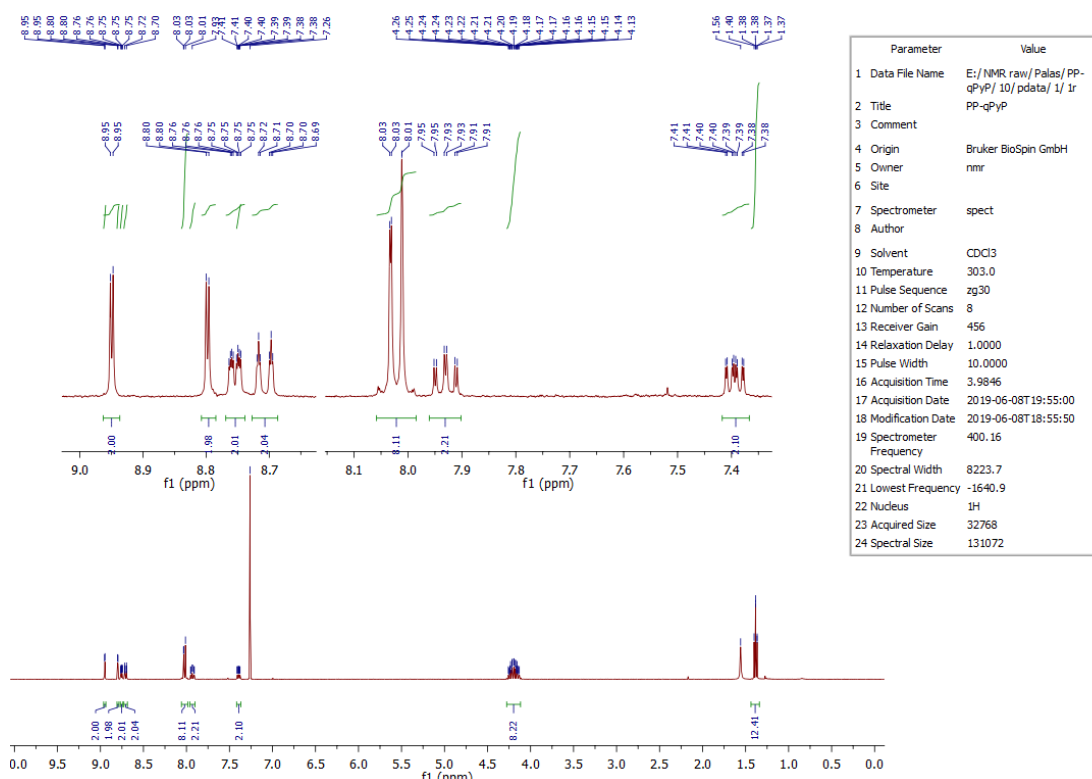


Figure 6.2 ¹H NMR spectrum of compound **3**.

Cobalt[tetraethyl([2,2':6',2'':6'',2'''-quaterpyridine]-4',4''-diylbis(4,1phenylene))

bis(phosphonate)] bis-chloro (**Co-qPyE**) was generated through the following steps: $\text{CoCl}_2 \cdot 6\text{H}_2\text{O}$ (75.5 mg, 0.31 mmol) was dissolved in methanol (6 mL). A chloroform solution (6 mL) of compound **3** (233 mg, 0.31 mmol) was added slowly under stirring for 2 h at ambient temperature. A brown solid was obtained gradually. The solid was filtered and washed thoroughly with methanol and chloroform to remove the unreacted ligand and solvent. The solid was dried in a vacuum oven to result in yellow powder. Yield: 120 mg (45%). Anal. calcd. for $\text{C}_{40}\text{H}_{40}\text{Cl}_2\text{CoN}_4\text{O}_6\text{P}_2$: C, 55.57; H, 4.66; N, 6.48. Found: C, 55.70; H, 4.76; N, 6.98; HRMS m/z calcd for $\text{C}_{40}\text{H}_{40}\text{CoN}_4\text{O}_6\text{P}_2 [\text{M}-2\text{Cl}]^{2+}$ 793.1755, found 793.1762.

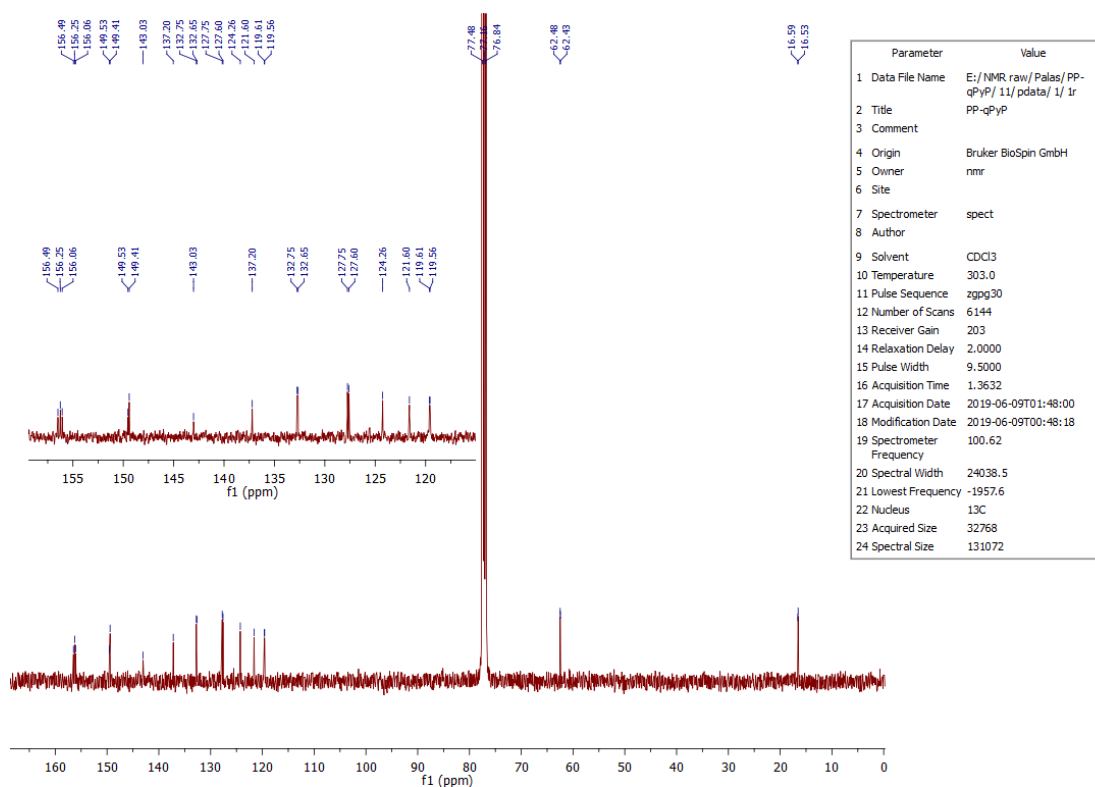


Figure 6.3 ^{13}C NMR spectrum of compound **3**.

Cobalt[2,2' :6',2'' :6'',2'''-quaterpyridine]-4',4''-diylbis(4,1-phenylene)bis(phosphonic acid)] bis - chloro (**Co-qPyH**): hydrolysis of phosphonate ester groups of **Co-qPyE** could not be accomplished in refluxing at 6 N HCl as usual owing to high

risk of decomplexation, so the following procedure was instead followed. Co-qPyE (50 mg, 0.06 mmol) was taken in an oven-dried three-neck round-bottom flask kept under Ar atmosphere. About 6 mL of extra dry DMF was added followed by 0.25 mL of distilled triethylamine added to the mixture. Then 0.15 mL of SiMe₃Br was added to the reaction mixture dropwise, and the reaction mixture was stirred for 48 h at 45°C. The reaction mixture was cooled, and solvent was removed through reduced pressure. The residue was diluted with very dilute aqueous solution of HCl (pH = 6.8) to remove quaternary ammonium salt formed during reaction and protonation of phosphonic acid. The brown precipitate was filtered and washed with water and dried under vacuum to produce 36 mg (yield = 82%) of Co-qPyH. Anal. calcd. for C₃₂H₂₄Cl₂CoN₄O₆P₂·3.1H₂O: C, 47.56; H, 3.77; N, 6.93. Found: C, 48.07; H, 4.23; N, 6.93. HRMS m/z calcd. for C₃₂H₂₄CoN₄O₆P₂ [M-2Cl⁻]²⁺ 681.0503, found 681.0494.

Immobilization of Co-qPyH on TiO₂

A 0.2 mM solution of Co-qPyH was prepared in methanol (10 mL). Two drops of ultra-pure water were added, and the mixture was sonicated for 10 min with continuous degassing by Ar. Then electrodes were dipped in the solution, and was heated at 45°C in the oven for 48 h. The electrodes were completely rinsed with methanol and dried under nitrogen atmosphere.

CIGS electrode preparation

Mo back contact layer was deposited by DC sputtering, with total thickness of 500 nm. CuIn_{0.1}Ga_{0.9}Se₂ (CIGS) layers were grown onto Mo coated soda-lime glass substrates by co-evaporation from elemental sources. The soda-lime glass consists of

1-mm-thick microscope slides. The process used for CIGS deposition is known as CuPRO process.[139] Specifically, keep In and Ga fluxes constant and change Cu flux so that nominal composition of the growing film undergoes Cu-poor/Cu-rich transitions needed for high-performance devices.[140] Substrate temperature was kept at 580°C during the whole deposition.

The n-type CdS layer was grown by chemical bath deposition. The p-CIGS/n-CdS heterojunction was finally covered with Radio Frequency (RF) sputtered ZnO/ZnO:Al bilayer. Here the applied ZnO:Al-layer thickness was ca. 300 nm ($R_{\text{sheet}} = 20 \Omega/\text{sq}$).

6.2 Characterization Methods

6.2.1 Solar simulator

Irradiation was simulated with a 150 W Xenon lamp from Oriel Instrument with light source positioned at 20 cm from the PV cell for PV-EC configuration and 25 cm from the photoelectrode in PEC configuration. UV light was filtered at wavelength below $\lambda = 435 \text{ nm}$ with a low-pass filter (Schott GG435). Part of the light above 1000 nm was also filtered via a water filter to avoid electrolyte warmup. In PEC configuration of Chapter 2, the cell was equipped with a quartz window to avoid parasite light absorption.

6.2.2 UV-visible spectroscopy

UV-visible absorption measurement was conducted on a Agilent Cary 60 spectrometer. Aliquots of the solution were poured into a quartz cell (1 cm length). Typical spectral region ranged from 200-800 nm and it was swept at a rate of 720 nm s^{-1} .

6.2.3 Attenuated Total Reflection (ATR-IR) spectroscopy

ATR-IR spectra were recorded on BRUKER Tensor 27.

6.2.4 Inductively coupled plasma – Optical Emission Spectroscopy (ICP - OES)

The loading of the catalyst was measured by ICP-OES. Cobalt catalyst was desorbed from the electrode in a 69% HNO₃ solution overnight. This solution was then diluted to a 1.38% HNO₃ solution for analysis. ICAP 6300 (Thermo Sci.) ICP – OES CID spectrometer was used with detection of cobalt in different samples (238.8 nm band that is the most intense).

6.2.5 X-ray photoelectron spectrometer (XPS)

The composition (content in carbon, nitrogen, oxygen, phosphorus and cobalt elements) of samples were determined by XPS spectrometer analyses, which were performed with a THERMO-VG ESCALAB 250 spectrometer accompanied by a microfocalized X-ray source (K α Al 1486.6 eV).

6.2.6 pH measurements

pH value of the electrolyte was tested on a Hanna pH210 and HI221 instruments and 6 mm microelectrodes (Fisher Scientific).

6.2.7 Nuclear magnetic resonance (NMR) spectroscopy

¹H and ¹³C NMR spectra were recorded on an AVANCE 300 Ultra Shield BRUKER

and AVANCE 400 BRUKER at room temperature. Chemical shifts for ^1H and ^{13}C NMR spectra are referenced relative to residual protium and ^{13}C in the deuterated solvent (CDCl_3 $\delta = 7.26$ ppm for ^1H and $\delta = 77.16$ ppm for ^{13}C). Chemical shifts are given in ppm and coupling constants in Hz.

6.2.8 Gas chromatography (GC)

GC analyses of gas during the electrolysis (H_2 , O_2 , N_2 , CO , and CO_2) were conducted with an Agilent Technologies 7820A GC system equipped with a thermal conductivity detector and a capillary column (CARBOPLOT P7), with Argon as carrier gas. Calibration curves for H_2 and CO were determined separately by injecting known volumes of pure gas. Figure 6.4 and 6.5 show the calibration curves of H_2 and CO , respectively. A typical gas chromatogram in Figure 6.6 as an example indicates the peaks of H_2 and CO .

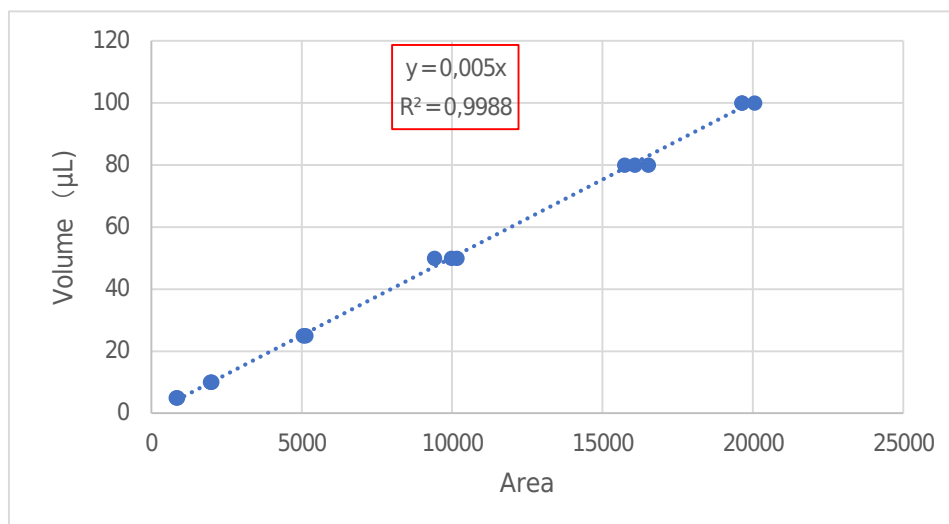


Figure 6.4 Calibration curve of H_2 .

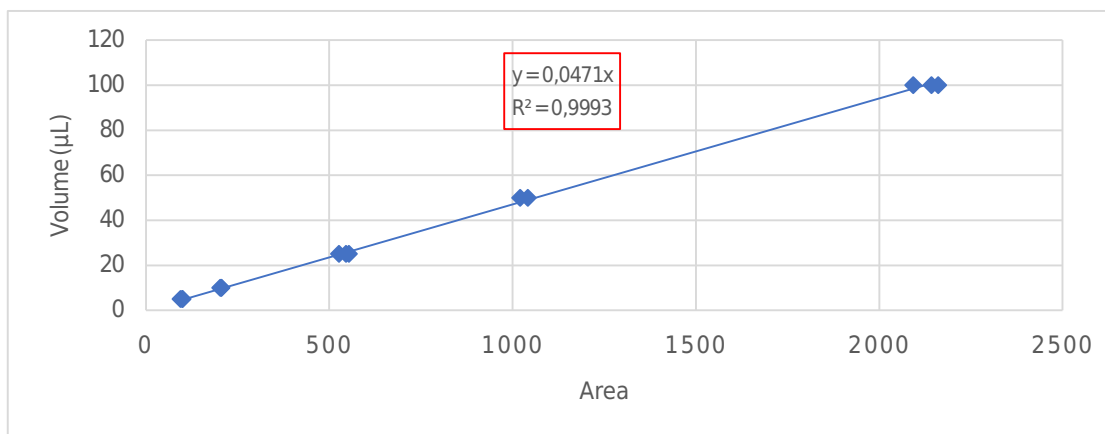


Figure 6.5 Calibration curve of CO.

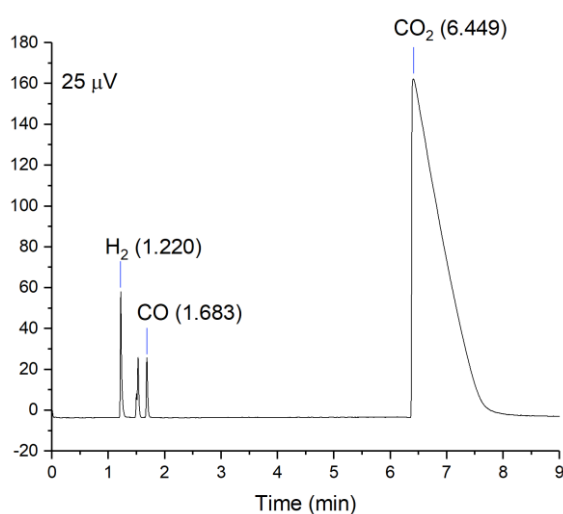


Figure 6.6 Gas chromatogram

For products quantification, TON and TOF are calculated from Eqs. 6-1 and 6-2, respectively:

$$\text{TON} = n_{\text{product}} / n_{\text{catalyst, film}} \quad (6-1)$$

$$\text{TOF} = \text{TON} / t \quad (6-2)$$

These apparent TON value can be regarded as a lower estimation of the real number of catalytic cycles because the electrolysis is not performed until the total deactivation of the catalyst/photoelectrode. Moreover, in most cases, the amount of active molecular catalyst is significantly smaller (ca. up to an order of magnitude) than

the amount of catalyst present at the electrode.[98, 143] Finally, the amount of electrochemically active catalyst in the film is decaying over time, so the TOF is changing with time t . The TOF calculated here is a mean value over the course of the electrolysis.

6.2.9 EC and PEC measurements

EC and PEC experiments were conducted on a CHI 760 or a PGSTAT 302N Autolab potentiostat–galvanostat, and every experiment was conducted at least three times to make sure the reproducibility of the results. Electrolytes were saturated with the gas of interest by bubbling more than 20 min prior to measurement. In a standard three-electrode EC setup, counter electrode (CE) was a platinum grid, separated from the working compartment by a glass frit bridge filled with the same electrolyte. Potentials were measured relative to a saturated calomel electrode (SCE) as reference electrode (Ref) and converted into relative hydrogen electrode (RHE) using Eq. 6-3:

$$E \text{ (V vs. RHE)} = E \text{ (V vs. SCE)} + 0.242 + 0.059 \times \text{pH} \quad (6-3)$$

For PV- EC system in Chapter 2, the external CIGS PV cell is connected in series with a Co-qPyH|m-TiO₂ electrode. Front (–) and back (+) lateral contacts of the cell were taken on ZnO:Al and Mo layers, respectively. When the geometric surface of TiO₂ is different from the surface of irradiated CIGS, current density is reported per surface of electrode and per surface of PV. When only one single value is reported for current density, it means that both CIGS and TiO₂ surfaces have been intentionally set to the same value. In PEC configuration, working electrode was covered with an insulating tape covering the edges to avoid contact between underlayers and electrolyte. A window

was previously cut in this tape to define the working area. Working surface was between 0.15 and 0.25 cm².

6.2.10 $J(V)$ curve measurement.

$J(V)$ measurements were performed in conditions as close as possible to those defined by standard testing conditions, namely at 25°C, under AM1.5 (using filtered light source) illumination normalized at 1000 Wm⁻². The size of the investigated solar cells was about 1 × 0.5 cm². The actual value of J_{sc} was deduced from the integration of EQE measured from a laboratory-built setup. The surface shaded by the grids, accounted in the J_{sc} calculation, is about 3%.

References

- [1] B.D. Santerm, M.F. Wehnert, M.L. Wigley, R. Sauseng, G.A. Meehl, K.E. Taylor, C. Ammann, J. Arblaster, W.M. Washington, J.S. Boylea, W. Bruggemann, *Contributions of Anthropogenic and Natural Forcing to Recent Tropopause Height Changes*, *Science*, 301 (2003) 479-483.
- [2] N.M.T. Westerhold, A. J. Drury, D. Liebrand, C. Agnini, E. Anagnostou, J.S.K. Barnet, S.M. Bohaty, D.D. Vleeschouwer, F. Florindo, T. Frederichs, D.A. Hodell, A.E. Holbourn, D. Kroon, V. Lauretano, K. Littler, L.J. Lourens, M. Lyle, H. Pälike, U. Röhl, J. Tian, R.H. Wilkens, P.A. Wilson, J.C. Zachos, *An astronomically dated record of Earth's climate and its predictability over the last 66 million years*, *Science*, 369 (2020) 1383-1387
- [3] <https://www.nasa.gov/press-release/2020-tied-for-warmest-year-on-record-nasa-analysis-shows>.
- [4] Global Climate Change Indicators, <https://www.ncdc.noaa.gov/monitoring-references/faq/indicators.php>.
- [5] Summary for Policymakers of IPCC Special Report on Global Warming of 1.5°C approved by governments, <https://www.ipcc.ch/2018/10/08/summary-for-policymakers-of-ipcc-special-report-on-global-warming-of-1-5c-approved-by-governments/>.
- [6] CO₂ emissions, <https://ourworldindata.org/co2-emissions>.
- [7] S.N. Habisreutinger, L. Schmidt-Mende, J.K. Stolarczyk, *Photocatalytic Reduction of CO₂ on TiO₂ and Other Semiconductors*, *Angew. Chem. Int. Ed.*, 52 (2013) 7372-7408.
- [8] V. Kumaravel, J. Bartlett, S.C. Pillai, *Photoelectrochemical Conversion of Carbon Dioxide (CO₂) into Fuels and Value-Added Products*, *ACS Energy Lett.*, 5 (2020) 486-519.
- [9] B.R. Eggins, P.K.J. Robertson, E.P. Murphy, E. Woods, J.T.S. Irvine, *Factors affecting the photoelectrochemical fixation of carbon dioxide with semiconductor colloids*, *J. Photochem. Photobiol. A*, 118 (1998) 31-40.
- [10] A. Fujishima, X. Zhang, D. Tryk, *TiO₂ photocatalysis and related surface phenomena*, *Surf. Sci. Rep.*, 63 (2008) 515-582.
- [11] M. Shen, M.A. Henderson, *Identification of the Active Species in Photochemical Hole Scavenging Reactions of Methanol on TiO₂*, *J. Phys. Chem. Lett.*, 2 (2011) 2707-2710.
- [12] P.V. Kamat, *Manipulation of Charge Transfer Across Semiconductor Interface. A Criterion That Cannot Be Ignored in Photocatalyst Design*, *J. Phys. Chem. Lett.*, 3 (2012) 663-672.
- [13] C. Sah, R.N. Noyce, W. Shockley, *Carrier Generation and Recombination in P-N Junctions and P-N Junction Characteristics*, *Proc. IRE*, 45 (1957) 1228-1243.
- [14] Y. Chen, J.C. Crittenden, S. Hackney, L. Sutter, D.W. Hand, *Preparation of a Novel TiO₂-Based p-n Junction Nanotube Photocatalyst*, *Environ. Sci. Technol.*, 39 (2005) 1201-1208.
- [15] R.P. Smith, A.A.-C. Hwang, T. Beetz, E. Helgren, *Introduction to semiconductor processing: Fabrication and characterization of p-n junction silicon solar cells*, *Am. J. Phys.*, 86 (2018) 740-746.
- [16] H. Kisch, *Semiconductor Photocatalysis—Mechanistic and Synthetic Aspects*, *Angew. Chem. Int. Ed. Engl.*, 52 (2013) 812-847.
- [17] J.L. White, M.F. Baruch, J.E. Pander Iii, Y. Hu, I.C. Fortmeyer, J.E. Park, T. Zhang, K. Liao, J. Gu, Y. Yan, T.W. Shaw, E. Abelev, A.B. Bocarsly, *Light-Driven Heterogeneous Reduction of Carbon Dioxide: Photocatalysts and Photoelectrodes*, *Chem. Rev.*, 115 (2015) 12888-12935.
- [18] P.D. Tran, L.H. Wong, J. Barber, J.S.C. Loo, *Recent advances in hybrid photocatalysts for solar*

- fuel production*, Energy Environ. Sci., 5 (2012) 5902-5918.
- [19] S. Xu, E.A. Carter, *Theoretical Insights into Heterogeneous (Photo)electrochemical CO₂ Reduction*, Chem. Rev., 119 (2019) 6631-6669.
- [20] A.A. Peterson, J.K. Nørskov, *Activity descriptors for CO₂ electroreduction to methane on transition-metal catalysts*, J. Phys. Chem. Lett., 3 (2012) 251-258.
- [21] E. Casado-Rivera, D.J. Volpe, L. Alden, C. Lind, C. Downie, T. Vázquez-Alvarez, A.C. Angelo, F.J. DiSalvo, H.D. Abruña, *Electrocatalytic activity of ordered intermetallic phases for fuel cell applications*, J. Am. Chem. Soc., 126 (2004) 4043-4049.
- [22] J.F. Hull, Y. Himeda, W.-H. Wang, B. Hashiguchi, R. Periana, D.J. Szalda, J.T. Muckerman, E. Fujita, *Reversible hydrogen storage using CO₂ and a proton-switchable iridium catalyst in aqueous media under mild temperatures and pressures*, Nature Chem., 4 (2012) 383-388.
- [23] K. Maeda, *Metal-Complex/Semiconductor Hybrid Photocatalysts and Photoelectrodes for CO₂ Reduction Driven by Visible Light*, Adv. Funct., 31 (2019) 1808205.
- [24] M. Bradley, T. Tysak, *p-Type silicon based photoelectrochemical cells for optical energy conversion: electrochemistry of tetra-azomacrocyclic metal complexes at illuminated*, J. Electroanal. Chem. Interf. Electrochem., 135 (1982) 153-157.
- [25] B.A. Parkinson, P.F. Weaver, *Photoelectrochemical pumping of enzymatic CO₂ reduction*, Nature, 309 (1984) 148-149.
- [26] J.-P. Petit, P. Chartier, M. Beley, J.-P. Deville, *Molecular catalysts in photoelectrochemical cells: study of an efficient system for the selective photoelectroreduction of CO₂: p-GaP or p-GaAs/Ni (cyclam)²⁺, aqueous medium*, J. Electroanal. Chem. Interf. Electrochem., 269 (1989) 267-281.
- [27] B. JO'M, J. Wass, *On the photoelectrocatalytic reduction of carbon dioxide*, Mater. Chem. Phys., 22 (1989) 249-280.
- [28] B. Kumar, J.M. Smieja, C.P. Kubiak, *Photoreduction of CO₂ on p-type Silicon Using Re (bipy-Bu')(CO)₃Cl: Photovoltages Exceeding 600 mV for the Selective Reduction of CO₂ to CO*, J. Phys. Chem. C., 114 (2010) 14220-14223.
- [29] E. Torralba-Peñalver, Y. Luo, J.D. Compain, S. Chardon-Noblat, B. Fabre, *Selective Catalytic Electroreduction of CO₂ at Silicon Nanowires (SiNWs) Photocathodes Using Non-Noble Metal-Based Manganese Carbonyl Bipyridyl Molecular Catalysts in Solution and Grafted onto SiNWs*, Acs Catal., 5 (2015) 6138-6147.
- [30] E.E. Barton, D.M. Rampulla, A.B. Bocarsly, *Selective Solar-Driven Reduction of CO₂ to Methanol Using a Catalyzed p-GaP Based Photoelectrochemical Cell*, J. Am. Chem. Soc., 130 (2008) 6342-6344.
- [31] T. Arai, S. Sato, K. Uemura, T. Morikawa, T. Kajino, T. Motohiro, *Photoelectrochemical reduction of CO₂ in water under visible-light irradiation by a p-type InP photocathode modified with an electropolymerized ruthenium complex*, Commun. Chem., 46 (2010) 6944-6946.
- [32] S. Sato, T. Arai, T. Morikawa, K. Uemura, T.M. Suzuki, H. Tanaka, T. Kajino, *Selective CO₂ conversion to formate conjugated with H₂O oxidation utilizing semiconductor/complex hybrid photocatalysts*, J. Am. Chem. Soc., 133 (2011) 15240-15243.
- [33] T. Arai, S. Tajima, S. Sato, K. Uemura, T. Morikawa, T. Kajino, *Selective CO₂ conversion to formate in water using a CZTS photocathode modified with a ruthenium complex polymer*, Commun. Chem., 47 (2011) 12664-12666.
- [34] L.Z. Fan, J. Maier, *High-performance polypyrrole electrode materials for redox supercapacitors*, Electrochem. commun., 8 (2006) 937-940.

- [35] K. Sekizawa, S. Sato, T. Arai, T. Morikawa, *Solar-driven photocatalytic CO₂ reduction in water utilizing a ruthenium complex catalyst on p-type Fe₂O₃ with a multiheterojunction*, ACS Catal., 8 (2018) 1405-1416.
- [36] A. Bachmeier, S. Hall, S.W. Ragsdale, F.A. Armstrong, *Selective visible-light-driven CO₂ reduction on a p-type dye-sensitized NiO photocathode*, J. Am. Chem. Soc., 136 (2014) 13518-13521.
- [37] C.R. Cabrera, H.D. Abruña, *Electrocatalysis of CO₂ reduction at surface modified metallic and semiconducting electrodes*, J. Electroanal. Chem. Interf. Electrochem., 209 (1986) 101-107.
- [38] A. Paracchino, V. Laporte, K. Sivula, M. Grätzel, E. Thimsen, *Highly active oxide photocathode for photoelectrochemical water reduction*, Nature Mater., 10 (2011) 456-461.
- [39] J.M. Smieja, C.P. Kubiak, *Re(bipy-^tBu)(CO)₃Cl-improved catalytic activity for reduction of carbon dioxide: IR-spectroelectrochemical and mechanistic studies*, Inorg. Chem., 49 (2010) 9283-9289.
- [40] M. Schreier, P. Gao, M.T. Mayer, J. Luo, T. Moehl, M.K. Nazeeruddin, S.D. Tilley, M. Grätzel, *Efficient and selective carbon dioxide reduction on low cost protected Cu₂O photocathodes using a molecular catalyst*, Energy Environ. Sci., 8 (2015) 855-861.
- [41] M.G. Walter, E.L. Warren, J.R. McKone, S.W. Boettcher, Q. Mi, E.A. Santori, N.S. Lewis, *Solar water splitting cells*, Chem. Rev., 110 (2010) 6446-6473.
- [42] K. Maeda, D. An, C.S.K. Ranasinghe, T. Uchiyama, R. Kuriki, T. Kanazawa, D. Lu, S. Nozawa, A. Yamakata, Y. Uchimoto, *Visible-light CO₂ reduction over a ruthenium (ii)-complex/C₃N₄ hybrid photocatalyst: the promotional effect of silver species*, J. Mater. Chem. A., 6 (2018) 9708-9715.
- [43] M. Schreier, J. Luo, P. Gao, T. Moehl, M.T. Mayer, M. Grätzel, *Covalent Immobilization of a Molecular Catalyst on Cu₂O Photocathodes for CO₂ Reduction*, J. Am. Chem. Soc., 138 (2016) 1938-1946.
- [44] J.T. Song, H. Ryoo, M. Cho, J. Kim, J.-G. Kim, S.-Y. Chung, J. Oh, *Nanoporous Au Thin Films on Si Photoelectrodes for Selective and Efficient Photoelectrochemical CO₂ Reduction*, Adv. Energy Mater., 7 (2017) 1601103.
- [45] Y. Hu, F. Chen, P. Ding, H. Yang, J. Chen, C. Zha, Y. Li, *Designing effective Si/Ag interface via controlled chemical etching for photoelectrochemical CO₂ reduction*, J. Mater. Chem. A., 6 (2018) 21906-21912.
- [46] S.K. Choi, U. Kang, S. Lee, D.J. Ham, S.M. Ji, H. Park, *Sn-Coupled p-Si Nanowire Arrays for Solar Formate Production from CO₂*, Adv. Energy Mater., 4 (2014) 1301614.
- [47] K. Alenezi, S.K. Ibrahim, P. Li, C.J. Pickett, *Solar Fuels: Photoelectrosynthesis of CO from CO₂ at p-Type Si using Fe Porphyrin Electrocatalysts*, Chem. Eur. J., 19 (2013) 13522-13527.
- [48] J.S. DuChene, G. Tagliabue, A.J. Welch, W.H. Cheng, H.A. Atwater, *Hot Hole Collection and Photoelectrochemical CO₂ Reduction with Plasmonic Au/p-GaN Photocathodes*, Nano Lett., 18 (2018), 2545-2550.
- [49] T. Arai, S. Sato, T. Kajino, T. Morikawa, *Solar CO₂ reduction using H₂O by a semiconductor/metal-complex hybrid photocatalyst: enhanced efficiency and demonstration of a wireless system using SrTiO₃ photoanodes*, Energy Environ. Sci., 6 (2013) 1274.
- [50] Q. Kong, D. Kim, C. Liu, Y. Yu, Y. Su, Y. Li, P. Yang, *Directed Assembly of Nanoparticle Catalysts on Nanowire Photoelectrodes for Photoelectrochemical CO₂ Reduction*, Nano Lett., 16 (2016) 5675-5680.
- [51] J. Qiu, G. Zeng, M.A. Ha, M. Ge, Y. Lin, M. Hettick, B. Hou, A.N. Alexandrova, A. Javey, S.B.

- Cronin, *Artificial Photosynthesis on TiO₂-Passivated InP Nanopillars*, Nano Lett., 15 (2015) 6177-6181.
- [52] S. Chu, S. Fan, Y. Wang, D. Rossouw, Y. Wang, G.A. Botton, Z. Mi, *Tunable Syngas Production from CO₂ and H₂O in an Aqueous Photoelectrochemical Cell*, Angew. Chem. Int. Ed. , 55 (2016) 14262-14266.
- [53] Q. Shen, Z. Chen, X. Huang, M. Liu, G. Zhao, *High-Yield and Selective Photoelectrocatalytic Reduction of CO₂ to Formate by Metallic Copper Decorated Co₃O₄ Nanotube Arrays*, Environ. Sci. Technol., 49 (2015) 5828-5835.
- [54] Y.J. Jang, I. Jeong, J. Lee, J. Lee, M.J. Ko, J.S. Lee, *Unbiased Sunlight-Driven Artificial Photosynthesis of Carbon Monoxide from CO₂ Using a ZnTe-Based Photocathode and a Perovskite Solar Cell in Tandem*, ACS Nano, 10 (2016) 6980-6987.
- [55] J. Jean, P.R. Brown, R.L. Jaffe, T. Buonassisi, V. Bulović, *Pathways for solar photovoltaics*, Energy Environ. Sci., 8 (2015) 1200-1219.
- [56] S.J. Palm, K. Kushiya, L. Stolt, A.N. Tiwari, E.Niemi, K.M. Beck,, P.W.C. Eberspacher, A. Bayman, U. Schoop, K. Ramanathan, B. Wieting, B. Dimmler, C. Kuhn, S. Whitelegg, U. Rühle, D. Lincot, N. Naghavi,, M.C.L.-S. T. Walter, R. Schatmann, A. Kuypers, B. Szyszka, P.L.S. Siebentritt, M. Powalla, R. Noufi, H.-W. Schock, *White paper for CIGS thin film solar cell technology*, 2016.
- [57] P. Jackson, R. Wuerz, D. Hariskos, E. Lotter, W. Witte, M. Powalla, *Effects of heavy alkali elements in Cu(In,Ga)Se₂ solar cells with efficiencies up to 22.6 %*, Phys. Status Solidi RRL, 10 (2016).
- [58] "Photovoltaics Report," Fraunhofer ISE, 2016.
- [59] F. Kessler, D. Rudmann, *Technological aspects of flexible CIGS solar cells and modules*, Sol. Energy, 77 (2004) 685-695.
- [60] D.D. Hsu, P. O'Donoghue, V. Fthenakis, G.A. Heath, H.C. Kim, P. Sawyer, J.-K. Choi, D.E. Turney, *Life Cycle Greenhouse Gas Emissions of Crystalline Silicon Photovoltaic Electricity Generation*, J. Ind. Ecol., 16 (2012) S122-S135.
- [61] K.A.W. Horowitz, M. Woodhouse, *Cost and potential of monolithic CIGS photovoltaic modules*, 2015 IEEE 42nd Photovoltaic Specialist Conference (PVSC), pp. 1-6.
- [62] D. Rudmann, D. Brémaud, A.F. da Cunha, G. Bilger, A. Strohm, M. Kaelin, H. Zogg, A.N. Tiwari, *Sodium incorporation strategies for CIGS growth at different temperatures*, Thin Solid Films, 480-481 (2005) 55-60.
- [63] J. Hedstrom, H. Ohlsen, M. Bodegard, A. Kylner, L. Stolt, D. Hariskos, M. Ruckh, H. Schock, *ZnO/CdS/Cu(In,Ga)Se₂ thin film solar cells with improved performance*, Conference Record of the Twenty Third IEEE Photovoltaic Specialists Conference - 1993 (Cat. No.93CH3283-9), 1993, pp. 364-371.
- [64] A. Chirilă, P. Reinhard, F. Pianezzi, P. Bloesch, A.R. Uhl, C. Fella, L. Kranz, D. Keller, C. Gretener, H. Hagedorfer, D. Jaeger, R. Erni, S. Nishiwaki, S. Buecheler, A.N. Tiwari, *Potassium-induced surface modification of Cu(In,Ga)Se₂ thin films for high-efficiency solar cells*, Nature Mater., 12 (2013) 1107-1111.
- [65] MiaSolé., "MiaSolé - Home. <http://miasole.com/>," 2016.
- [66] A. Gerthoffer, F. Roux, F. Emieux, P. Faucherand, H. Fournier, L. Grenet, S. Perraud, *CIGS solar cells on flexible ultra-thin glass substrates: Characterization and bending test*, Thin Solid Films, 592 (2015) 99-104.
- [67] N. Kohara, S. Nishiwaki, Y. Hashimoto, T. Negami, T. Wada, *Electrical properties of the*

- Cu(In,Ga)Se₂/MoSe₂/Mo structure*, Sol. Energ. Mat. Sol. Cells, 67 (2001) 209-215.
- [68] D. Abou-Ras, G. Kostorz, D. Bremaud, M. Kälin, F.V. Kurdesau, A.N. Tiwari, M. Döbeli, *Formation and characterisation of MoSe₂ for Cu(In,Ga)Se₂ based solar cells*, Thin Solid Films, 480-481 (2005) 433-438.
- [69] M. Tomassini, *Synthèse de couches minces de molybdène et application au sein des cellules solaires à base de Cu(In,Ga)Se₂ co-éaporé*. PhD thesis, Université de Nantes, 2013.
- [70] J.H. Yoon, J.H. Kim, W.M. Kim, J.K. Park, Y.J. Baik, T.Y. Seong, J.h. Jeong, *Electrical properties of CIGS/Mo junctions as a function of MoSe₂ orientation and Na doping*, Prog. Photovolt.: Res. App., 22 (2014) 90-96.
- [71] R. Caballero, M. Nichterwitz, A. Steigert, A. Eicke, I. Lauermann, H.W. Schock, C.A. Kaufmann, *Impact of Na on MoSe₂ formation at the CIGSe/Mo interface in thin-film solar cells on polyimide foil at low process temperatures*, Acta Mater., 63 (2014) 54-62.
- [72] K. Orgassa, H.W. Schock, J.H. Werner, *Alternative back contact materials for thin film Cu(In,Ga)Se₂ solar cells*, Thin Solid Films, 431-432 (2003) 387-391.
- [73] T. Klinkert, *Comprehension and optimisation of the co-evaporation deposition of Cu(In,Ga)Se₂ absorber layers for very high efficiency thin film solar cells*. PhD thesis, Université Pierre et Marie Curie-Paris VI, 2015.
- [74] T. Klinkert, M. Jubault, F. Donsanti, D. Lincot, J.-F. Guillemoles, *Differential in-depth characterization of co-evaporated Cu(In,Ga)Se₂ thin films for solar cell applications*, Thin Solid Films, 558 (2014) 47-53.
- [75] P.D. Paulson, R.W. Birkmire, W.N. Shafarman, *Optical characterization of CuIn_{1-x}Ga_xSe₂ alloy thin films by spectroscopic ellipsometry*, J. Appl. Phys., 94 (2003) 879-888.
- [76] M.I. Alonso, M. Garriga, C.A. Durante Rincón, E. Hernández, M. León, *Optical functions of chalcopyrite CuGa_xIn_{1-x}Se₂ alloys*, Appl. Phys. A, 74 (2002) 659-664.
- [77] S. Siebentritt, M. Igalson, C. Persson, S. Lany, *The electronic structure of chalcopyrites—bands, point defects and grain boundaries*, Prog. Photovolt.: Res. Appl., 18 (2010) 390-410.
- [78] R. Scheer, H.-W. Schock, *Chalcogenide Photovoltaics: Physics, Technologies, and Thin Film Devices*, Wiley-VCH, 2011.
- [79] S. Siebentritt, L. Gütay, D. Regesch, Y. Aida, V. Deprédurand, *Why do we make Cu(In,Ga)Se₂ solar cells non-stoichiometric?*, Sol. Energy Mater Sol. Cells, 119 (2013) 18-25.
- [80] J.E. Granata, J.R. Sites, S. Asher, R.J. Matson, *Quantitative incorporation of sodium in CuInSe₂ and Cu(In,Ga)Se₂ photovoltaic devices*, Conference Record of the Twenty Sixth IEEE Photovoltaic Specialists Conference - 1997, 1997, pp. 387-390.
- [81] A. Rockett, M. Bodegard, K. Granath, L. Stolt, *Na incorporation and diffusion in CuIn_{1-x}Ga_xSe₂*, Conference Record of the Twenty Fifth IEEE Photovoltaic Specialists Conference - 1996, 1996, pp. 985-987.
- [82] S.-H. Wei, S.B. Zhang, A. Zunger, *Effects of Na on the electrical and structural properties of CuInSe₂*, J. Appl. Phys., 85 (1999) 7214-7218.
- [83] A. Chirilă, S. Buecheler, F. Pianezzi, P. Bloesch, C. Gretener, A.R. Uhl, C. Fella, L. Kranz, J. Perrenoud, S. Seyrling, R. Verma, S. Nishiwaki, Y.E. Romanyuk, G. Bilger, A.N. Tiwari, *Highly efficient Cu(In,Ga)Se₂ solar cells grown on flexible polymer films*, Nature Mater., 10 (2011) 857-861.
- [84] U. Rau, K. Taretto, S. Siebentritt, *Grain boundaries in Cu(In, Ga)(Se, S)₂ thin-film solar cells*, Appl. Phys. A, 96 (2008) 221.

- [85] C.K. D. Abou-Ras, V. Küstner, P. van Aken, U. Jahn, M. Contreras, R. Caballero, C. Kaufmann, R. Scheer, T. Unold, and H.-W. Schock, *Grain boundary types in chalcopyrite-type thin films and their correlations with film texture and electrical properties*, *Thin Solid Films*, 517 (2009) 2545–2549.
- [86] R. Baier, C. Leendertz, D. Abou-Ras, M.C. Lux-Steiner, S. Sadewasser, *Properties of electronic potential barriers at grain boundaries in Cu(In,Ga)Se₂ thin films*, *Sol. Energy Mater Sol. Cells*, 130 (2014) 124-131.
- [87] P. Jackson, R. Wuerz, D. Hariskos, E. Lotter, W. Witte, M. Powalla, *Effects of heavy alkali elements in Cu(In,Ga)Se₂ solar cells with efficiencies up to 22.6%*, *Phys. Status Solidi RRL*, 10 (2016) 583-586.
- [88] R. Kamada, T. Yagioka, S. Adachi, A. Handa, K.F. Tai, T. Kato, H. Sugimoto, *New world record Cu(In,Ga)(Se,S)₂ thin film solar cell efficiency beyond 22%*, 2016 IEEE 43rd Photovoltaic Specialists Conference (PVSC), pp. 1287-1291.
- [89] C. Broussillou, C. Viscogliosi, A. Rogee, S. Angle, P.P. Grand, S. Bodnar, C. Debauche, J.L. Allary, B. Bertrand, C. Guillou, L. Parissi, S. Coletti, *Statistical Process Control for Cu(In,Ga)(S,Se)₂ electrodeposition-based manufacturing process of 60×120 cm² modules up to 14,0% efficiency*, 2015 IEEE 42nd Photovoltaic Specialist Conference (PVSC), pp. 1-5.
- [90] D. Schmid, M. Ruckh, F. Grunwald, H.W. Schock, *Chalcopyrite/defect chalcopyrite heterojunctions on the basis of CuInSe₂*, *J. Appl. Phys.*, 73 (1993) 2902-2909.
- [91] M.A. Contreras, L.M. Mansfield, B. Egaas, J. Li, M. Romero, R. Noufi, E. Rudiger-Voigt, W. Mannstadt, *Wide bandgap Cu(In,Ga)Se₂ solar cells with improved energy conversion efficiency*, *Prog. Photovolt.: Res. Appl.*, 20 (2012) 843-850.
- [92] M. Burgelman, P. Nollet, S. Degrave, *Modelling polycrystalline semiconductor solar cells*, *Thin Solid Films*, 361-362 (2000) 527-532.
- [93] M. Burgelman, J. Verschraegen, S. Degrave, P. Nollet, *Modeling thin-film PV devices*, *Prog. Photovolt.: Res. Appl.*, 12 (2004) 143-153.
- [94] A. Gorczyński, J.M. Harrowfield, V. Patroniak, A.R. Stefankiewicz, *Quaterpyridines as Scaffolds for Functional Metallosupramolecular Materials*, *Chem. Rev.*, 116 (2016) 14620-14674.
- [95] L. Chen, G. Chen, C.F. Leung, C. Cometto, M. Robert, T.C. Lau, *Molecular quaterpyridine-based metal complexes for small molecule activation: water splitting and CO₂ reduction*, *Chem. Soc. Rev.*, 49 (2020) 7271-7283.
- [96] Z. Guo, S. Cheng, C. Cometto, E. Anxolabehere-Mallart, S.M. Ng, C.C. Ko, G. Liu, L. Chen, M. Robert, T.C. Lau, *Highly Efficient and Selective Photocatalytic CO₂ Reduction by Iron and Cobalt Quaterpyridine Complexes*, *J. Am. Chem. Soc.*, 138 (2016) 9413-9416.
- [97] C. Cometto, L. Chen, P.-K. Lo, Z. Guo, K.-C. Lau, E. Anxolabéhère-Mallart, C. Fave, T.-C. Lau, M. Robert, *Highly Selective Molecular Catalysts for the CO₂-to-CO Electrochemical Conversion at Very Low Overpotential. Contrasting Fe vs Co Quaterpyridine Complexes upon Mechanistic Studies*, *ACS Catal.*, 8 (2018) 3411-3417.
- [98] M. Wang, L. Chen, T.C. Lau, M. Robert, *A Hybrid Co Quaterpyridine Complex/Carbon Nanotube Catalytic Material for CO₂ Reduction in Water*, *Angew. Chem. Int. Ed.*, 57 (2018) 7769-7773.
- [99] C. Cometto, R. Kuriki, L. Chen, K. Maeda, T.C. Lau, O. Ishitani, M. Robert, *A Carbon Nitride/Fe Quaterpyridine Catalytic System for Photostimulated CO₂-to-CO Conversion with Visible Light*, *J. Am. Chem. Soc.*, 140 (2018) 7437-7440.

- [100] B. Ma, G. Chen, C. Fave, L. Chen, R. Kuriki, K. Maeda, O. Ishitani, T.C. Lau, J. Bonin, M. Robert, *Efficient Visible-Light-Driven CO₂ Reduction by a Cobalt Molecular Catalyst Covalently Linked to Mesoporous Carbon Nitride*, *J. Am. Chem. Soc.*, 142 (2020) 6188-6195.
- [101] K.L. Materna, R.H. Crabtree, G.W. Brudvig, *Anchoring groups for photocatalytic water oxidation on metal oxide surfaces*, *Chem. Soc. Rev.*, 46 (2017) 6099-6110.
- [102] S.A. Paniagua, A.J. Giordano, O.N.L. Smith, S. Barlow, H. Li, N.R. Armstrong, J.E. Pemberton, J.-L. Brédas, D. Ginger, S.R. Marder, *Phosphonic Acids for Interfacial Engineering of Transparent Conductive Oxides*, *Chem. Rev.*, 116 (2016) 7117-7158.
- [103] T. Inoue, A. Fujishima, S. Konishi, K. Honda, *Photoelectrocatalytic reduction of carbon dioxide in aqueous suspensions of semiconductor powders*, *Nature*, 277 (1979) 637-638.
- [104] X. Chen, S.S. Mao, *Titanium Dioxide Nanomaterials: Synthesis, Properties, Modifications, and Applications*, *Chem. Rev.*, 107 (2007) 2891-2959.
- [105] M.D. Hernández-Alonso, F. Fresno, S. Suárez, J.M. Coronado, *Development of alternative photocatalysts to TiO₂: Challenges and opportunities*, *Energy Environ. Sci.*, 2 (2009) 1231-1257.
- [106] Y. Kou, S. Nakatani, G. Sunagawa, Y. Tachikawa, D. Masui, T. Shimada, S. Takagi, D.A. Tryk, Y. Nabetani, H. Tachibana, H. Inoue, *Visible light-induced reduction of carbon dioxide sensitized by a porphyrin–rhenium dyad metal complex on p-type semiconducting NiO as the reduction terminal end of an artificial photosynthetic system*, *J. Catal.*, 310 (2014) 57-66.
- [107] G. Sahara, H. Kumagai, K. Maeda, N. Kaeffer, V. Artero, M. Higashi, R. Abe, O. Ishitani, *Photoelectrochemical Reduction of CO₂ Coupled to Water Oxidation Using a Photocathode with a Ru(II)–Re(I) Complex Photocatalyst and a CoO_x/TaON Photoanode*, *J. Am. Chem. Soc.*, 138 (2016) 14152-14158.
- [108] H. Kumagai, G. Sahara, K. Maeda, M. Higashi, R. Abe, O. Ishitani, *Hybrid photocathode consisting of a CuGaO₂ p-type semiconductor and a Ru(II)–Re(I) supramolecular photocatalyst: non-biased visible-light-driven CO₂ reduction with water oxidation*, *Chem. Sci.*, 8 (2017) 4242-4249.
- [109] J.J. Leung, J. Warnan, K.H. Ly, N. Heidary, D.H. Nam, M.F. Kuehnel, E. Reisner, *Solar-driven reduction of aqueous CO₂ with a cobalt bis(terpyridine)-based photocathode*, *Nat. Catal.*, 2 (2019) 354-365.
- [110] B. Shan, S. Vanka, T.-T. Li, L. Troian-Gautier, M.K. Brennaman, Z. Mi, T.J. Meyer, *Binary molecular-semiconductor p–n junctions for photoelectrocatalytic CO₂ reduction*, *Nat. Energy*, 4 (2019) 290-299.
- [111] X. Sun, Q. Zhu, X. Kang, H. Liu, Q. Qian, Z. Zhang, B. Han, *Molybdenum–Bismuth Bimetallic Chalcogenide Nanosheets for Highly Efficient Electrocatalytic Reduction of Carbon Dioxide to Methanol*, *Angew. Chem. Int. Ed.*, 55 (2016) 6771-6775.
- [112] J. Albo, A. Sáez, J. Solla-Gullón, V. Montiel, A. Irabien, *Production of methanol from CO₂ electroreduction at Cu₂O and Cu₂O/ZnO-based electrodes in aqueous solution*, *Appl. Catal. B*, 176 (2015) 709-717.
- [113] S. Navarro-Jaén, M. Virginie, J. Bonin, M. Robert, R. Wojcieszak, A.Y. Khodakov, *Highlights and challenges in the selective reduction of carbon dioxide to methanol*, *Nat. Rev. Chem.*, 5 (2021) 564-579.
- [114] T. Hatsukade, K.P. Kuhl, E.R. Cave, D.N. Abram, J.T. Feaster, A.L. Jongorius, C. Hahn, T.F. Jaramillo, *Carbon Dioxide Electroreduction using a Silver–Zinc Alloy*, *Energy Technol.*, 5 (2017) 955-961.

- [115] Q.H. Low, N.W.X. Loo, F. Calle-Vallejo, B.S. Yeo, *Enhanced Electroreduction of Carbon Dioxide to Methanol Using Zinc Dendrites Pulse-Deposited on Silver Foam*, *Angew. Chem. Int. Ed.*, 58 (2019) 2256-2260.
- [116] R. Kas, R. Kortlever, A. Milbrat, M.T.M. Koper, G. Mul, J. Baltrusaitis, *Electrochemical CO₂ reduction on Cu₂O-derived copper nanoparticles: controlling the catalytic selectivity of hydrocarbons*, *Phys. Chem. Chem. Phys.*, 16 (2014) 12194-12201.
- [117] I. Azcarate, C. Costentin, M. Robert, J.-M. Savéant, *Through-space charge interaction substituent effects in molecular catalysis leading to the design of the most efficient catalyst of CO₂-to-CO electrochemical conversion*, *J. Am. Chem. Soc.*, 138 (2016) 16639-16644.
- [118] C. Costentin, S. Drouet, M. Robert, J.-M. Savéant, *A local proton source enhances CO₂ electroreduction to CO by a molecular Fe catalyst*, *Science*, 338 (2012) 90-94.
- [119] K. Ogura, S. Yamasaki, *Conversion of carbon monoxide into methanol at room temperature and atmospheric pressure*, *J. Chem. Soc., Faraday Trans. 1*, 81 (1985) 267-271.
- [120] K. Ogura, K. Takamagari, *Electrocatalytic reduction of carbon dioxide to methanol. Part 2. Effects of metal complex and primary alcohol*, *J. Chem. Soc., Dalton Trans.*, (1986) 1519-1523.
- [121] K. Ogura, I. Yoshida, *Electrocatalytic reduction of CO₂ to methanol: Part 9: Mediation with metal porphyrins*, *J. Mol. Catal.*, 47 (1988) 51-57.
- [122] M. Abdinejad, A. Seifitokaldani, C. Dao, E.H. Sargent, X.-a. Zhang, H.B. Kraatz, *Enhanced electrochemical reduction of CO₂ catalyzed by cobalt and iron amino porphyrin complexes*, *ACS Appl. Energy Mater.*, 2 (2019) 1330-1335.
- [123] E. Boutin, M. Wang, J.C. Lin, M. Mesnage, D. Mendoza, B. Lassalle-Kaiser, C. Hahn, T.F. Jaramillo, M. Robert, *Aqueous Electrochemical Reduction of Carbon Dioxide and Carbon Monoxide into Methanol with Cobalt Phthalocyanine*, *Angew. Chem. Int. Ed.*, 58 (2019) 16172-16176.
- [124] S.Q. Lomax, *Phthalocyanine and quinacridone pigments: their history, properties and use*, *Stud. Conserv.*, 50 (2005) 19-29.
- [125] C.M. Lieber, N.S. Lewis, *Catalytic reduction of carbon dioxide at carbon electrodes modified with cobalt phthalocyanine*, *J. Am. Chem. Soc.*, 106 (1984) 5033-5034.
- [126] J. Choi, P. Wagner, S. Gambhir, R. Jalili, D.R. MacFarlane, G.G. Wallace, D.L. Officer, *Steric Modification of a Cobalt Phthalocyanine/Graphene Catalyst to Give Enhanced and Stable Electrochemical CO₂ Reduction to CO*, *ACS Energy Lett.*, 4 (2019) 666-672.
- [127] S. Roy, M. Miller, J. Warnan, J.J. Leung, C.D. Sahm, E. Reisner, *Electrocatalytic and Solar-Driven Reduction of Aqueous CO₂ with Molecular Cobalt Phthalocyanine–Metal Oxide Hybrid Materials*, *ACS Catal.*, 11 (2021) 1868-1876.
- [128] W.-H. Cheng, M.H. Richter, I. Sullivan, D.M. Larson, C. Xiang, B.S. Brunschwig, H.A. Atwater, *CO₂ Reduction to CO with 19% Efficiency in a Solar-Driven Gas Diffusion Electrode Flow Cell under Outdoor Solar Illumination*, *ACS Energy Lett.*, 5 (2020) 470-476.
- [129] C.E. Creissen, M. Fontecave, *Solar-Driven Electrochemical CO₂ Reduction with Heterogeneous Catalysts*, *Adv. Energy Mater.*, 11 (2021) 2002652.
- [130] T. Chatterjee, E. Boutin, M. Robert, *Manifesto for the routine use of NMR for the liquid product analysis of aqueous CO₂ reduction: from comprehensive chemical shift data to formaldehyde quantification in water*, *Dalton Trans.*, 49 (2020) 4257-4265.
- [131] E. Boutin, A. Salamé, L. Merakeb, T. Chatterjee, M. Robert, *On the Existence and Role of Formaldehyde During Aqueous Electrochemical Reduction of Carbon Monoxide to Methanol by*

- Cobalt Phthalocyanine*, Chem. Eur. J., Early View (2022), e202200697.
- [132] S.R.M. Levinshtein, M. Shur, *Handbook Series on Semiconductor Parameters*, World Scientific 1996.
- [133] D.S. Ginley, M.B. Chamberlain, *Interfacial Chemistry at p-GaP Photoelectrodes*, J. Electrochem. Soc., 129 (1982) 2141-2145.
- [134] M. Halmann, *Photoelectrochemical reduction of aqueous carbon dioxide on p-type gallium phosphide in liquid junction solar cells*, Nature, 275 (1978) 115-116.
- [135] J.P. Petit, P. Chartier, M. Beley, J.P. Deville, *Molecular catalysts in photoelectrochemical cells, study of an efficient system for the selective photoelectroreduction of CO₂: p-GaI or p-GaAs/Ni(cyclam)²⁺, aqueous medium*, J. Electroanal. Chem., 269 (1989) 267-281.
- [136] G. Zeng, J. Qiu, Z. Li, P. Pavaskar, S.B. Cronin, *CO₂ Reduction to Methanol on TiO₂-Passivated GaP Photocatalysts*, ACS Catal., 4 (2014) 3512-3516.
- [137] J. Qiu, G. Zeng, P. Pavaskar, Z. Li, S.B. Cronin, *Plasmon-enhanced water splitting on TiO₂-passivated GaP photocatalysts*, Phys. Chem. Chem. Phys., 16 (2014) 3115-3121.
- [138] M.B.J.-P.C.a.J.-P. Sauvage, *Photoassisted electro-reduction of CO₂ on p-GaAs in the presence of Ni cyclam²⁺*, J. Electroanal. Chem., 206 (1986) 333-339.
- [139] J. Kessler, C. Chityuttakan, J. Lu, J. Schöldström, L. Stolt, *Cu(In,Ga)Se₂ thin films grown with a Cu-poor/rich/poor sequence: growth model and structural considerations*, Prog. Photovolt.: Res. Appl, 11 (2003) 319-331.
- [140] N. Barreau, T. Painchaud, F. Couzinié-Devy, L. Arzel, J. Kessler, *Recrystallization of CIGSe layers grown by three-step processes: A model based on grain boundary migration*, Acta Mater., 58 (2010) 5572-5577.
- [141] M. Wang, K. Torbensen, D. Salvatore, S. Ren, D. Joulié, F. Dumoulin, D. Mendoza, B. Lassalle-Kaiser, U. Işci, C.P. Berlinguette, M. Robert, *CO₂ electrochemical catalytic reduction with a highly active cobalt phthalocyanine*, Nat. Commun., 10 (2019) 3602.